

Abstract of thesis entitled

Search for chargino and neutralino production in final states with two same-sign leptons, jets and missing transverse momentum at $\sqrt{s} = 13$ TeV with the ATLAS detector

Submitted by

Cheuk Yee LO

for the degree of Doctor of Philosophy
at The University of Hong Kong
in November 2018

The Standard Model in particle physics has successfully explained almost all experimental results in the microscopic scale with high accuracy. However, the nature of dark matter and the Higgs mass hierarchy problem are still unanswered questions. Supersymmetry (SUSY), which proposes a new symmetry between fermions and bosons, is one of the most promising theories beyond the Standard Model for potentially answering these questions. In recent searches for supersymmetric particles that are involved in strong interaction, their masses were found to be above 1 TeV. Since the production cross section drops as the masses of particles increase, this might suggest that the pair production of electroweak gauginos, which tend to have lower mass, is a dominant SUSY production process at the Large Hadron Collider (LHC). In addition, the upgrade in the increased center-of-mass energy of the proton-proton collisions \sqrt{s} to 13 TeV has opened a new phase of exploration for electroweak SUSY productions.

In this thesis, a search is presented for the electroweak pair production of a chargino and a neutralino ($p + p \rightarrow \tilde{\chi}_1^\pm + \tilde{\chi}_2^0$), where the chargino decays to the

lightest neutralino and a W boson ($\tilde{\chi}_1^\pm \rightarrow \tilde{\chi}_1^0 + W$), and the second lightest neutralino decays to the lightest neutralino and a Standard-Model-like Higgs boson ($\tilde{\chi}_2^0 \rightarrow \tilde{\chi}_1^0 + h$). The final state with two same-sign leptons, jets and missing transverse momentum is considered in this search. The two leptons come from the leptonic decay of the W boson and the Higgs boson, with the decay modes of $h \rightarrow WW$, $h \rightarrow \tau\tau$ or $h \rightarrow ZZ$. This analysis is based on the proton-proton collision data delivered by the LHC at $\sqrt{s} = 13$ TeV with the ATLAS (A Toroidal LHC ApparatuS) particle detector. The integrated luminosity of data is 36.1 fb^{-1} .

As a result, observations are consistent with the Standard Model predictions, therefore new exclusion limits for the masses of $\tilde{\chi}_1^\pm/\tilde{\chi}_2^0$ and $\tilde{\chi}_1^0$ are set, which supersedes the run 1 results.

An abstract of exactly 307 words

**Search for chargino and neutralino
production in final states with two
same-sign leptons, jets and missing
transverse momentum at $\sqrt{s} = 13$ TeV
with the ATLAS detector**

by

Cheuk Yee LO

A thesis submitted in partial fulfilment of the requirements for
the Degree of Doctor of Philosophy
at The University of Hong Kong.

November 2018

Declarations

I declare that this thesis represents my own work, except where acknowledgement is made, and that it has not been previously included in a thesis, dissertation or report submitted to this University or to any other institution for a degree, diploma or other qualifications.

Signed
.....

Cheuk Yee LO

Acknowledgments

I would like to take this opportunity to thank people who helped me do the research.

I would like to thank my supervisor Dr. Tu Yanjun for giving me the opportunity to do the research, for her support on my research and for her guidance and suggestions on my analysis.

I would like to thank Dr. Zhang Dongliang. He helped me get familiar with the linux software: the linux shell, the text editor (vim) and the revision control system (svn). He taught me how to use the ATLAS software: the event analysis software (ROOT and RootCore), the data acquisition software(dq2 and rucio) and the distributed computing management (grid and panda). I learnt from him many other experimental skill. He also helped our group write the multiLepSearch package to generate the ntuple.

I would like to thank Dr. Daniela Katherinne Paredes Hernandez. She gave a lot of suggestions on the analysis. She designed the validation region and helped me do the analysis.

I would like to thank Dr. Jeanette Miriam Lorenz from the Ludwig Maximilian University of Munich. She provided the configuration file for HistFitter and organized various tasks during collaboration.

I would like to thank Dr. Peter Tornambe from Albert the Ludwig University of Freiburg. He helped me compare my fake lepton background measurements with his measurements by helping me generate the Monte Carlo ntuples.

I would like to thank Dr. Daniela Maria Kock from the Ludwig Maximilian University of Munich. She provided me the ntuples for systematics study.

The study of the systematic uncertainties is not done by me, therefore it is not included here. The following are my contributions to the public paper [1] [2].

1. An alternative method for the SR optimization is used as a cross-check for

the signal regions optimized by Daniela Maria Kock. I also suggested that she can use m_{T2} for optimization.

2. I contribute to the ntuple production for the charge flip background. I also maintain the framework of the charge flip estimation.
3. I provide the cross-check to the work by Peter Tornambe (fake lepton background) and Daniela Paredes (validation region).

Contents

Abstract	i
Title Page	iii
Declaration	iv
Acknowledgments	v
Contents	vii
List of Figures	x
List of Tables	xv
List of Abbreviations and Symbols	xvii
1 Theoretical background	1
1.1 Introduction	1
1.2 Standard Model	1
1.2.1 Matter particles	2
1.2.2 Forces and carrier particles	3
1.2.3 Feynman diagram	3
1.3 Limitation of Standard Model	3
1.3.1 Dark matter	3
1.3.2 Hierarchy problem	5
1.3.3 Unification of forces	6
1.4 Supersymmetry	6
1.4.1 Minimal Supersymmetric Standard Model	6
1.5 Signal scenario	9

2 Experimental setup	12
2.1 Introduction	12
2.2 The Large Hadron Collider	12
2.3 ATLAS detector	14
2.3.1 The coordinate system and basic variables	16
2.3.2 The magnetic system	18
2.3.3 The inner detector	19
2.3.4 Calorimeter	23
2.3.5 Muon spectrometer	32
3 Dataset and event selection	36
3.1 Dataset	36
3.1.1 Data samples	36
3.1.2 MC samples	36
3.2 Pre-selection and event cleaning	38
3.3 Trigger strategy	39
3.4 Object definitions	40
3.4.1 Electrons	40
3.4.2 Muons	40
3.4.3 Jets	40
3.4.4 Missing transverse momentum	41
3.4.5 Overlap removal	42
4 Signal regions	43
4.1 Discriminant variables	43
4.2 Signal region optimization	45
4.2.1 Pre-selections	47
4.2.2 Samples	47
4.2.3 Optimization	47
4.2.4 Results of optimization	50
5 Background estimation	55
5.1 Charge flip background	55
5.1.1 Sources for charge flip background	55
5.1.2 Likelihood method	57

5.1.3	Background subtraction	60
5.1.4	Results without systematic uncertainty	60
5.1.5	Systematic uncertainties due to background subtraction . .	60
5.1.6	Systematic uncertainties due to likelihood method	62
5.1.7	Results with total uncertainties	64
5.1.8	MC validation	66
5.2	Fake lepton background	66
5.2.1	Sources for fake lepton background	66
5.2.2	Matrix method	68
5.2.3	Measurement of real efficiencies	72
5.2.4	Measurement of fake efficiencies	73
5.2.5	Validation for the fake lepton background	74
6	Validation regions	80
7	Results	85
8	Conclusion	90
A	List of MC samples	91
A.1	List of data samples	91
A.2	List of background MC samples	91
A.3	List of signal MC samples	96
B	Label for trigger [3,4]	98
B.1	Electron trigger	98
B.2	Muon trigger	98
References		101

List of Figures

1.1	The table for all fundamental particles in SM [5].	2
1.2	All allowed fundamental Feynman vertices in SM, except higgs-related vertices [6].	4
1.3	All allowed fundamental higgs-related Feynman vertices in SM. . .	5
1.4	The particles in Standard Model and their corresponding superpartners and their names	7
1.5	The exclusion contours for the masses $m_{\tilde{\chi}_1^\pm, \tilde{\chi}_2^0}$ and $m_{\tilde{\chi}_1^0}$ in the Run-I analysis [7].	9
1.6	The Feynman diagram for the Wh same-sign signal scenario in this thesis. The final states in this process include two same-sign leptons (electron or muon), quarks (i.e. jets) and missing transverse momentum contributed by the lightest neutralinos $\tilde{\chi}_1^0$ and neutrinos ν	10
2.1	The schematic diagram of the CERN accelerator complex, which shows a series of accelerators and facilities [8].	13
2.2	The cut-away view of the ATLAS detector. It is 25 m high and 44 m long [9].	15
2.3	The cross section of the ATLAS detector. This shows different components of the ATLAS and how ATLAS detects different types of particles [10].	15
2.4	This figure shows how the impact parameters z_0 and d_0 are defined by the nearest point (the small circle) of the track to the z-axis. It also shows how the azimuthal angle ϕ and the polar angle θ of the momentum \mathbf{p} are defined. p_T is the projection of the momentum \mathbf{p} onto the x-y plane.	17

2.5	The red lines show different directions corresponding to different positive values of pseudorapidity [11].	18
2.6	Schematic view of the magnetic system of the ATLAS detector [12].	19
2.7	The whole structure of the ATLAS inner detector [13].	20
2.8	The radius R from the beam for the 3 components: pixel, SCT and TRT [13].	21
2.9	The shapes, the orientations and the η coverage for each sensor [14].	22
2.10	Schematic view for the calorimeter system of the ATLAS detector [15].	24
2.11	Schematic view for one side of the end-cap and forward calorimeter [16].	25
2.12	Schematic view for one side of the end-cap and forward calorimeter. One layer of forward calorimeter is electromagnetic and two are hadronic [14].	25
2.13	The granularity in η and ϕ of the cells of each of the three layers in the electromagnetic calorimeter [14].	27
2.14	Schematic view of one module of the tile calorimeter [14].	29
2.15	Schematic view of the arrangement of the HEC readout structure in the 8.5 mm inter-plate gap. All dimensions are in mm [14].	30
2.16	Electrode structure of FCal 1 with the matrix of copper plates and the copper tubes and rods with the LAr gap for the electrodes. The Molière radius, R_M , is represented by the solid disk [14].	31
2.17	Cut-away view of the muon spectrometer [17].	33
2.18	The cross section of the barrel region for the muon spectrometer. Three concentric cylindrical layers of barrel MDT are shown [14].	34
2.19	The cross section of the end-cap region for the muon spectrometer. Four layers of end-cap MDT are shown in blue colour. Three layers of barrel MDT are also shown in green colour [14].	35
2.20	The cross-section of a MDT tube. When muons pass through the tube, free electrons are produced along the track, which drift to the anode wire [14].	35
4.1	Distributions of the kinematic variables used for the optimization in SRjet1. The pre-selections have been applied.	48

4.2	Distributions of the kinematic variables used for the optimization in SRjet23. The pre-selections have been applied.	49
4.3	The N-1 plots for SRjet1.	52
4.4	The N-1 plots for SRjet23.	53
4.5	The expected combined signal significances for different mass points.	54
5.1	It shows how the track of the electron is incorrectly reconstructed (the orange track), due to the process of bremsstrahlung and γ conversion.	56
5.2	It shows how the track of the electron is incorrectly reconstructed (the orange track), due to very high p_T of the electron.	56
5.3	The comparison between the OS events and the SS events in data. The number of OS events is much larger than the number of SS events by almost 10^3 times.	58
5.4	The measured values of the charge-flip rate ϵ_i in data. Only uncertainties due to the likelihood method are included.	61
5.5	The systematic variations of the charge-flip rate ϵ_i in data, due to the background subtraction.	62
5.6	This diagram shows how the original electron is found through the decay chain.	63
5.7	The comparisons between the likelihood method and the MC truth method. The systematic uncertainties due to likelihood method can be estimated.	64
5.8	The measured values of the charge-flip rate ϵ_i in data, with total uncertainties.	65
5.9	The comparisons between the weighted OS events and the SS events.	67
5.10	The real efficiencies for electrons (left) and muons (right). Only statistical uncertainties are considered.	73
5.11	The fake efficiencies for electrons (left) and muons (right). Only statistical uncertainties are considered.	74
5.12	Signal contributions in the validation region are shown for different mass points.	76

5.13 Distribution of the leading lepton p_T , m_{eff} , m_T , E_T^{miss} and n_{jets} in the electron-electron channel. The ratio of data to background yields is shown in the lower plot. The error bar includes all the systematic uncertainties except for the theoretical uncertainties.	77
5.14 Distribution of the leading lepton p_T , m_{eff} , m_T , E_T^{miss} and n_{jets} in the muon-muon channel. The ratio of data to background yields is shown in the lower plot. The error bar includes all the systematic uncertainties except for the theoretical uncertainties.	78
5.15 Distribution of the leading lepton p_T , m_{eff} , m_T , E_T^{miss} and n_{jets} in the electron-muon channel. The ratio of data to background yields is shown in the lower plot. The error bar includes all the systematic uncertainties except for the theoretical uncertainties.	79
6.1 Fractions of signal contribution are shown for the VRjet1 (left) and VRjet23 (right).	81
6.2 Background composition in the VRjet1 (left) and SRjet1 (right).	82
6.3 Background composition in the VRjet23 (left) and SRjet23 (right).	82
6.4 Distributions of the variables in the VRjet1 for the background estimation and the data are shown. A signal at a mass point $(m_{\tilde{\chi}_1^\pm, \tilde{\chi}_2^0}, m_{\tilde{\chi}_1^0}) = (175, 0)$ is also shown. The internal shaded area refers to the statistical uncertainties, while the external shaded area refers to the total uncertainty.	83
6.5 Distributions of the variables in the VRjet23 for the background estimation and the data are shown. A signal at a mass point $(m_{\tilde{\chi}_1^\pm, \tilde{\chi}_2^0}, m_{\tilde{\chi}_1^0}) = (175, 0)$ is also shown. The internal shaded area refers to the statistical uncertainties, while the external shaded area refers to the total uncertainty.	84

7.1 N-1 plots for different variable distributions in the SRjet1 for the background estimation and the data. The signal of the mass point with the highest significance ($m_{\tilde{\chi}_1^\pm, \tilde{\chi}_2^0}, m_{\tilde{\chi}_1^0} = (175,0)$) is shown by the red dashed line. The internal shaded area refers to the statistical uncertainties, while the external shaded area refers to the total uncertainty. The vertical dashed line shows the SR cut of that variable. The lower plot shows the ratio of data yields with respect to the total background predictions. The plots are made by Dr. Daniela Paredes [1].	86
7.2 N-1 plots for different variable distributions in the SRjet23 for the background estimation and the data. The signal of the mass point with the highest significance ($m_{\tilde{\chi}_1^\pm, \tilde{\chi}_2^0}, m_{\tilde{\chi}_1^0} = (175,0)$) is shown by the red dashed line. The internal shaded area refers to the statistical uncertainties, while the external shaded area refers to the total uncertainty. The vertical dashed line shows the SR cut of that variable. The lower plot shows the ratio of data yields with respect to the total background predictions. The plots are made by Dr. Daniela Paredes [1].	87
7.3 The expected and observed exclusion limits for the combined SRjet1 and SRjet23 are shown. Experimental and theoretical systematic uncertainties are applied to background and signal samples and illustrated by the yellow band and the red dotted contour lines respectively. The red dotted lines indicate the $\pm 1\sigma$ variation on the observed exclusion limit due to theoretical uncertainties on the signal cross-section. The upper limits for signal cross section at different mass points are also shown in grey numbers.	89

List of Tables

1.1	The spin and R-parity for the Standard Model particles and their superpartners.	8
2.1	The granularity in η and ϕ for different layers in the barrel region [14].	26
2.2	The granularity in η and ϕ for different layers in the end-cap region [14].	28
2.3	The granularity in the x-y plane in the forward calorimeter [14]. .	32
3.1	List of the single lepton triggers used in this analysis.	39
3.2	List of the di-lepton triggers used in this analysis.	40
3.3	Summary of the electron and muon selection criteria. The signal selection requirements are applied on top of the baseline criteria. .	41
3.4	Summary of the jet selection criteria.	42
4.1	Kinematic variables used in the optimization.	50
4.2	Final SR definitions	50
4.3	The yields in SRjet1. The unweighted event are also shown in parentheses.	51
4.4	The yields in SRjet23. The unweighted event are also shown in parentheses.	51
5.1	Binning in p_T and $ \eta $ for the charge-flip rate ϵ_i	57
5.2	Binning in p_T and $ \eta $ for real efficiencies.	73
5.3	Binning in p_T and $ \eta $ for fake efficiencies.	74
5.4	The background compositions in the validation region. The numbers in brackets are the event yields.	76

6.1	The definition of the two validation regions on top of the pre-selections in section 4.2.1. The values in red colour represent different cuts compared to the signal regions.	80
6.2	The expected number of background events and the observed number of data events in the VRjet1 (the second column) and VRjet23 (the third column). The uncertainties include the statistical and systematic uncertainties.	82
7.1	The observed events and the background yields in the signal regions are shown. The uncertainties include the statistical and systematic uncertainties.	85
7.2	From left to right: 95% confidence level upper limits on the visible cross section ($\langle \sigma_{\text{vis}} \rangle_{\text{obs}}^{95}$) and on the observed number of signal events (S_{obs}^{95}). The third column (S_{exp}^{95}) shows the 95% confidence level upper limit on the expected number of signal events, with $\pm 1\sigma$ excursions on the expectation of the background events. The last column shows the discovery p -value (p_0).	88
A.1	List of simulated W+jets processes	92
A.2	List of simulated Z+jets processes	93
A.3	List of simulated single-top processes	93
A.4	List of the simulated $t\bar{t}$ sample	93
A.5	List of simulated $t\bar{t}$ plus vector boson processes	93
A.6	List of simulated Higgs related processes, including Higgs plus vector boson production and $t\bar{t}H$ processes	94
A.7	List of simulated diboson processes	94
A.8	List of simulated triboson processes	94
A.9	List of simulated DrellYan processes	94
A.10	List of simulated multi-top processes	94
A.11	List of simulated V+ γ processes	95
A.12	List of signal samples	97
B.1	Label for electron trigger.	98
B.2	Label for muon trigger.	99

List of Abbreviations and Symbols

η pseudorapidity

p_T transverse momentum

BG background

BSM beyond the Standard Model

CERN the European Organization for Nuclear Research

CR control region

cut selection cut

Data the experimental data

jet a particle shower in a narrow cone from the hadronization of a quark or a gluon

lepton refer to electron or muon

LHC Large Hadron Collider

MC Monte Carlo Simulation

MET missing transverse energy

N-1 plot The plot with all selections are applied, except the selection for that variable

OS opposite sign

SM Standard Model

SR signal region

SS same sign

SUSY Supersymmetry

VR validation region

yield The resulting number of events

Chapter 1

Theoretical background

1.1 Introduction

Particle physics is a branch of physics that studies the most fundamental particles and their interactions. All matter in the universe is made up of these fundamental particles, and their interactions are described by the theories in particle physics. In 20th century, our understanding about the nature of fundamental particles has had great breakthrough and advance. Also, many particle colliders have been built to give much insight to develop the theories and test the theories. The currently mainstream theory of particle physics is called the Standard Model.

1.2 Standard Model

Standard Model(SM) is the current theory to describe the fundamental particles in particle physics. It has already gained huge success in predicting the experimental results, including the prediction of existence of the top quark, the tau neutrino, and the Higgs boson. It has also explained the most experimental results with high accuracy. It represents our best understanding of how the fundamental particles interact with each other.

Physicists discovered that there are 4 fundamental forces in the universe: electromagnetic force, weak force, strong force, and gravitational force. SM can describe three of them: electromagnetic, weak and strong interaction. Figure 1.1 shows all fundamental particles in the SM, and their mass, electric charge and spin. All matter is made up of fermions (purple and green), which is the first 3 columns in figure 1.1. Fermions are divided into two groups: quarks(purple) and

Standard Model of Elementary Particles

three generations of matter (fermions)					
	I	II	III		
QUARKS	mass 2/3 1/2	$\approx 2.4 \text{ MeV}/c^2$ 2/3 1/2	$\approx 1.275 \text{ GeV}/c^2$ 2/3 1/2	$\approx 172.44 \text{ GeV}/c^2$ 2/3 1/2	0 0 1
	up	u	charm	c	gluon
	down	d	strange	s	Higgs
	electron	e	muon	μ	photon
	neutrino	ν_e	neutrino	ν_μ	Z boson
	neutrino	ν_τ	W boson		
GAUGE BOSONS					
SCALAR BOSONS					

Figure 1.1: The table for all fundamental particles in SM [5].

leptons(green). The forces between the fermions are mediated by the force carriers, which is gauge bosons(red). Higgs bosons(yellow) are scalar bosons, which explain the masses of other massive particles.

1.2.1 Matter particles

There are six types of quarks: up quarks(u), down quarks(d), charm quarks(c), strange quarks(s), top quarks(t) and bottom quarks(b). Quarks interact with strong interactions, while leptons do not. There are three types of charged leptons: electrons, muons and taus. There are three types of neutral leptons: electron neutrinos, muon neutrinos and tau neutrinos. The first column is the first generation, which is the lightest and the most stable particles. Hence, normal matter in our daily life is made from the particles in the first generation. The second and third column are the second and third generation respectively, which are heavier

and less stable particles. These particles will finally decay into the particles in the first generation. Due to the phenomenon of neutrino oscillation, neutrinos are massive, but their value are still unknown.

1.2.2 Forces and carrier particles

Photon is the force carrier of electromagnetic interactions. Gluon is the force carrier of strong interactions. Z and W bosons are the force carriers of weak interactions. The effects of these fundamental forces stem from the exchange of the corresponding force carrier. These forces also have different strengths and different interaction ranges. The strong force is the strongest force, the electromagnetic force is in the middle, and the weak force is the weakest force. The electromagnetic force has infinite range, while the strong and weak forces have very short ranges at the level of subatomic particles.

For example, a proton is composed of two up quarks and one down quark, and a neutron is composed of one up quark and two down quarks. The forces between quarks inside the proton are mediated by gluons.

1.2.3 Feynman diagram

The fundamental interactions among these fundamental particles are described by the allowed Feynman vertices. All these allowed Feynman vertices in the SM are shown in figures 1.2 and 1.3.

1.3 Limitation of Standard Model

Although the Standard Model can explain almost all experimental results, there are still some phenomena it cannot explain.

1.3.1 Dark matter

Dark matter is some unknown matter that does not involve in electromagnetic interaction, but involves in gravitational interaction. It was first discovered in the Milky Way, by studying the speed of the stars orbiting around the center of the Milky Way. Because it does not involve in electromagnetic interaction, it cannot be seen by our telescopes. However, the SM cannot explain what dark matter is.

Standard Model Interactions (Forces Mediated by Gauge Bosons)

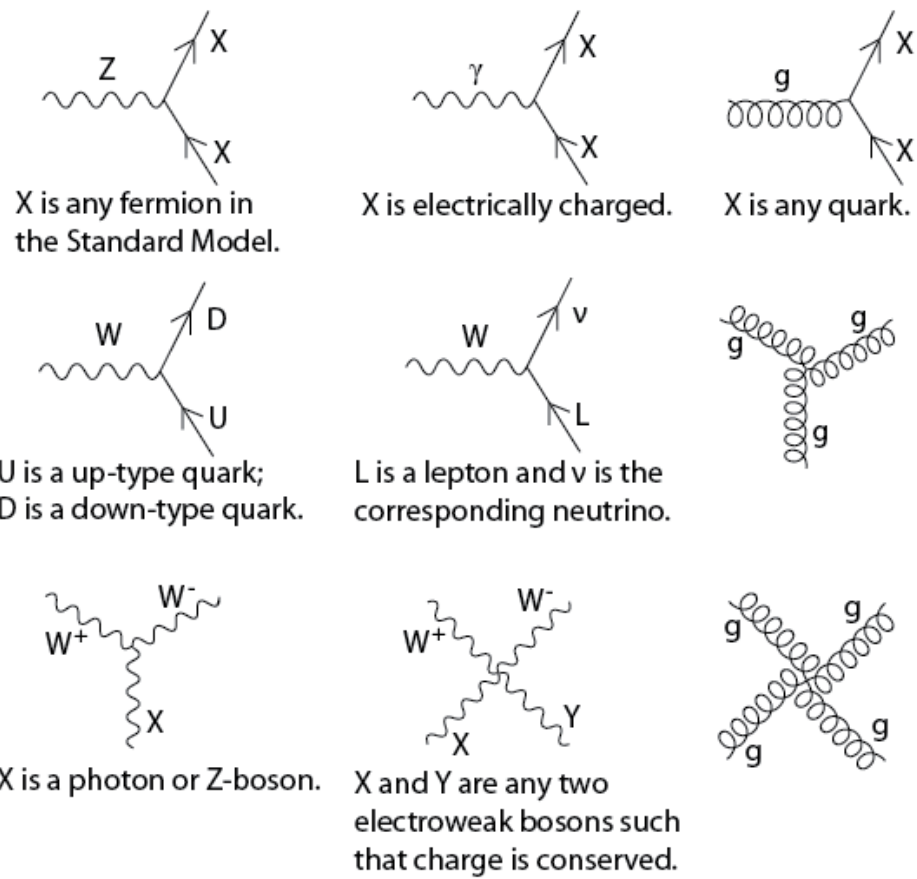


Figure 1.2: All allowed fundamental Feynman vertices in SM, except higgs-related vertices [6].

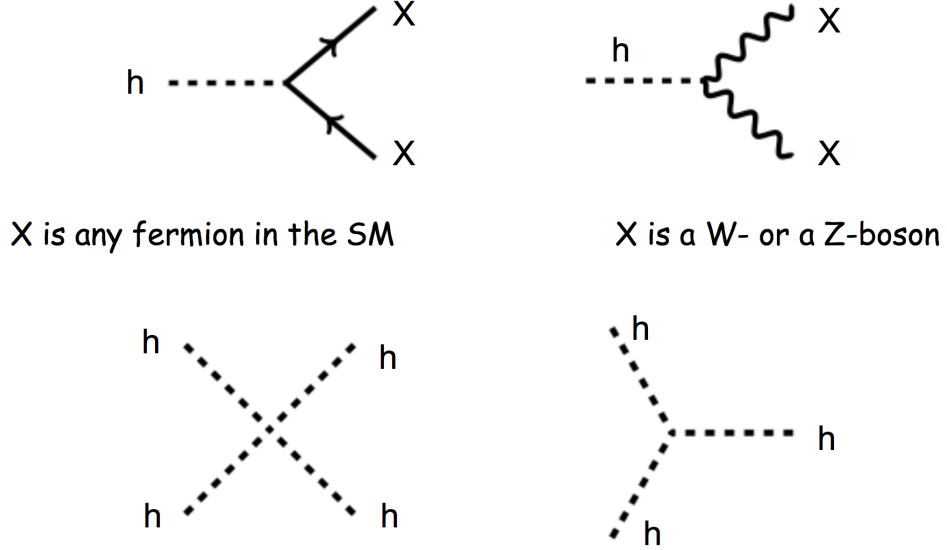


Figure 1.3: All allowed fundamental higgs-related Feynman vertices in SM.

1.3.2 Hierarchy problem

The hierarchy problem is the question why the weak force is stronger than the gravitational force by 10^{24} times. It is also asked why the mass of Higgs boson (~ 125 GeV) is much lighter than the Planck mass ($\sim 10^{19}$ GeV).

The Lagrangian for the interaction term between the fermion Dirac field f and the Higgs field H (i.e. Yukawa interaction) is given by

$$\mathcal{L}_{\text{Yukawa}} = -\lambda_f \bar{f} H f \quad (1.1)$$

where λ_f is the Yukawa coupling constant. The quantum correction to the square of the Higgs mass Δm_H^2 is then given by [18]

$$\Delta m_H^2 = -\frac{|\lambda_f|^2}{8\pi^2} \left[\Lambda^2 - 3m_f^2 \ln \left(\frac{\Lambda}{m_f} \right) \right] + \dots \quad (1.2)$$

where Λ is the energy scale up to which the quantum effects of gravity are not dominant, namely the Planck scale ($\sim 10^{19}$ GeV). Because the first term is quadratic divergent in Λ , its correction to the Higgs mass is in the order of Planck scale. Unless there are very delicate cancellation between the correction terms, the Higgs mass should be in the order of Planck scale. But, we found that the experimental Higgs mass is in the order of 125 GeV, and this is called the hierarchy problem.

1.3.3 Unification of forces

In the 1860s, James Clerk Maxwell wrote down his famous equations Maxwell's equations, which unify two different phenomena: electricity and magnetism. Due to this unification, we now understand that electricity and magnetism are two different manifestations of the same phenomenon, and we now call it electromagnetism.

Similar thing happened in the 1970s, physicists developed a theory that unified two fundamental forces: electromagnetic force and weak force. At the energy scale above 246 GeV, these two forces will merge into a single force: electroweak force. This unification predicted the existence of weak neutral current and a force carrier to carry this weak force. This force carrier Z boson was later confirmed experimentally in CERN.

After that, an effect of strong force was found experimentally that the strong force becomes weaker when the energy scale is higher. This may indicate that electroweak force and strong force will become a single force at higher energy scale. There are some theories beyond the Standard Model that can unify these forces, such as supersymmetry.

1.4 Supersymmetry

Supersymmetry(SUSY) is a theoretical extension of the Standard Model, and can answer some questions which the Standard Model cannot answer, mentioned in section 1.3. One of the problems SUSY can solve is the hierarchy problem of Higgs mass mentioned in section 1.3.2. We first notice that the negative sign of the quadratic divergent term in the equation 1.2 is due to the correction from the fermions. If there is a symmetry between the fermions and bosons, and the quadratic terms due to the bosons cancel with the quadratic terms due to the fermions, the hierarchy problem can be solved. This new symmetry is called the supersymmetry (SUSY).

1.4.1 Minimal Supersymmetric Standard Model

Minimal Supersymmetric Standard Model(MSSM) is the simplest realization of the supersymmetric theory that contains the minimum number of new particles and new interactions. It predicts that each particle in the Standard Model has

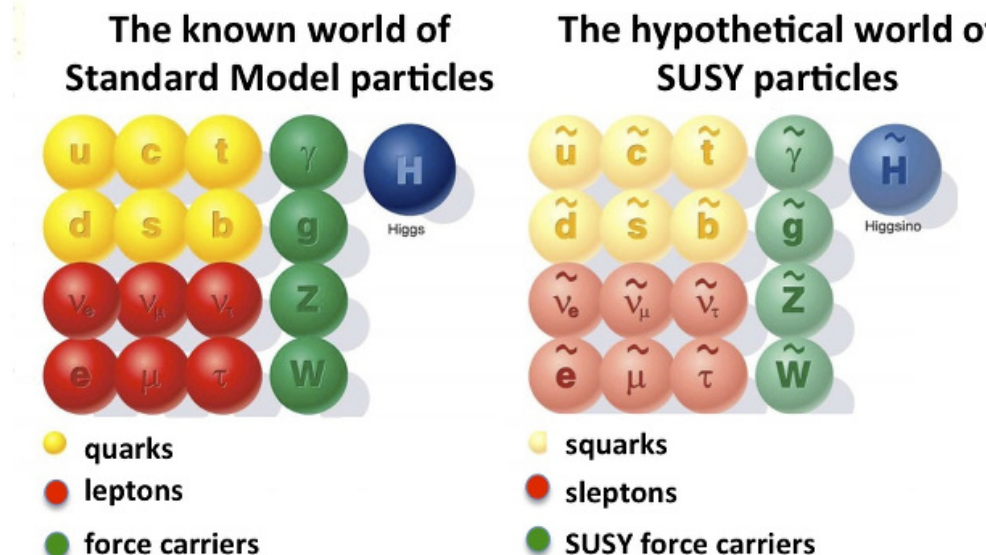


Figure 1.4: The particles in Standard Model and their corresponding superpartners and their names

its own partner particle, called the superpartner, as shown in figure 1.4. This is the new symmetry between the fermions and bosons. The name scheme for the superpartner of a fermion is to add a prefix “s”, in front of the name of the original Standard Model particle: squarks and sleptons, etc. For example, the superpartner of an electron is called selectron. For the superpartner of a Standard Model boson, the suffix “ino” is added: gluino and Higgsino, etc. As for the symbol for the superpartner, a tilde is added above the original symbol. For example, the symbol for selectron is \tilde{e} . Also, the spin of the superpartner differs from the Standard Model particle by $1/2$. For fermions, the spin of their superpartner is 0 , while for bosons, the spin of their superpartner is $1/2$. The superpartners interact with the same forces as the Standard Model particles, but they have different masses.

The quantum correction terms from the superpartners cancel the quadratic divergent terms in the Higgs mass. The idea is to postulate two scalar fields \tilde{f} for each fermion, with the coupling constant to the Higgs $\lambda_{\tilde{f}}$.

$$\mathcal{L} = -\lambda_{\tilde{f}} |H|^2 |\tilde{f}|^2 \quad (1.3)$$

The quantum correction to the square of the Higgs mass Δm_H^2 for the scalar field

is given by [18]

$$\Delta m_H^2 = \frac{\lambda_{\tilde{f}}}{16\pi^2} \left[\Lambda^2 - 2m_{\tilde{f}}^2 \ln \left(\frac{\Lambda}{m_{\tilde{f}}} \right) \right] + \dots \quad (1.4)$$

The quadratic terms in 1.2 and 1.4 exactly cancel with each other, if $\lambda_{\tilde{f}} = |\lambda_f|^2$. The logarithmic terms are left in the correction terms for the Higgs mass. Therefore, the hierarchy problem is solved.

In the MSSM, two neutral Higgs bosons (H_u^0 and H_d^0) and two charged Higgs bosons (H_u^+ and H_d^-) are introduced. Therefore, there are 4 neutral bosons: γ , Z , H_u^0 , H_d^0 and 4 charged bosons: W^+ , W^- , H_u^+ , H_d^- . The superpartners of the four neutral bosons together form four mass eigenstates called neutralinos: $\tilde{\chi}_1^0$, $\tilde{\chi}_2^0$, $\tilde{\chi}_3^0$ and $\tilde{\chi}_4^0$. The superpartners of the four charged bosons together form two mass eigenstates with electric charge ± 1 , called charginos: $\tilde{\chi}_1^\pm$ and $\tilde{\chi}_2^\pm$. The subscripts of the symbol of the neutralinos and charginos are labeled by the ascending order in mass. Table 1.1 summarizes the Standard Model particles and their superpartners.

Type	SM particle	Symbol	Spin	R-parity	Superpartner	Symbol	Spin	R-parity
Fermions	Quark	q	$\frac{1}{2}$	+1	Squark	\tilde{q}	0	-1
	Lepton	l	$\frac{1}{2}$	+1	Slepton	\tilde{l}	0	-1
Gluon	Gluon	g	1	+1	Gluino	\tilde{g}	$\frac{1}{2}$	-1
Neutral EW Bosons	Photon	γ	1	+1	Neutralinos	$\tilde{\chi}_1^0, \tilde{\chi}_2^0, \tilde{\chi}_3^0, \tilde{\chi}_4^0$	$\frac{1}{2}$	-1
	Z Boson	Z	1	+1				
	Neutral Higgs	H_u^0, H_d^0	0	+1				
Charged EW Bosons	W Boson	W^+, W^-	1	+1	Charginos	$\tilde{\chi}_1^\pm, \tilde{\chi}_2^\pm$	$\frac{1}{2}$	-1
	Charged Higgs	H_u^+, H_d^-	0	+1				

Table 1.1: The spin and R-parity for the Standard Model particles and their superpartners.

The baryon number B is defined by $\frac{1}{3}(n_q - n_{\bar{q}})$, where n_q is the number of quarks and $n_{\bar{q}}$ is the number of anti-quarks. The lepton number L is defined by $n_l - n_{\bar{l}}$, where n_l is the number of leptons and $n_{\bar{l}}$ is the number of anti-leptons. In the Standard Model and the experimental data, $B - L$ is conserved, but in MSSM, it is no longer conserved. To keep this conservation and prevent the proton decay, the R-parity P_R is introduced.

$$P_R = (-1)^{3(B-L)-2s} \quad (1.5)$$

where s is the spin. By this definition, all Standard Model particles have R-parity +1, and all supersymmetric particles have R-parity -1. If the R-parity is conserved, the lightest supersymmetric particle (LSP) does not decay. If the LSP is electrically neutral and interacts with matter only by the weak interaction

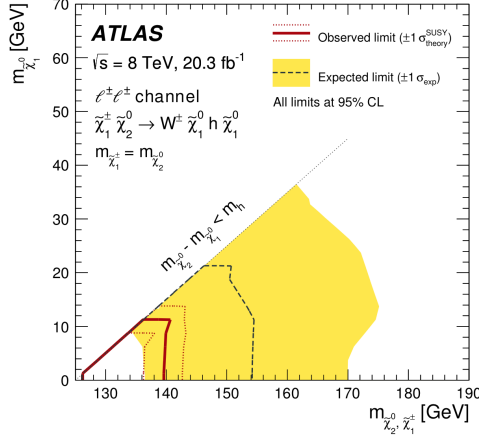


Figure 1.5: The exclusion contours for the masses $m_{\tilde{\chi}_1^\pm, \tilde{\chi}_2^0}$ and $m_{\tilde{\chi}_1^0}$ in the Run-I analysis [7].

and gravity, for example the lightest neutralinos $\tilde{\chi}_1^0$ or a sneutrino $\tilde{\nu}$, it can be a candidate for dark matter mentioned in section 1.3.1. In this analysis, the R-parity is assumed to be conserved, and the lightest neutralino $\tilde{\chi}_1^0$ is assumed to be the LSP. Due to the conservation of R-parity, the supersymmetric particles can only be pair-produced, and eventually decay into Standard Model particles and the lightest neutralino $\tilde{\chi}_1^0$, i.e. the LSP.

1.5 Signal scenario

In the recent searches for the squarks and gluinos, the masses of gluinos and the first and second generation squarks are suggested to be larger than 1 TeV, while the upper mass limits of the third generation squarks are below 1 TeV [19]. In this case, the direct pair production of electroweak gauginos (i.e. neutralinos and charginos) can be the dominant SUSY production process at the LHC, if the masses of the gluinos and squarks are significantly heavier than the low mass electroweak gauginos. Based on the results in the Run-I analysis [7] at the center-of-mass energy $\sqrt{s} = 8$ TeV shown in figure 1.5, the electroweak pair production is a promising search at a higher center-of-mass energy $\sqrt{s} = 13$ TeV with Run-II using 2015 and 2016 data.

The supersymmetric process searched in this thesis is the pair production of the lightest chargino $\tilde{\chi}_1^\pm$ and the second lightest neutralino $\tilde{\chi}_2^0$. The masses of them are assumed to be the same, $m_{\tilde{\chi}_1^\pm} = m_{\tilde{\chi}_2^0}$, and denoted by $m_{\tilde{\chi}_1^\pm, \tilde{\chi}_2^0}$ in the

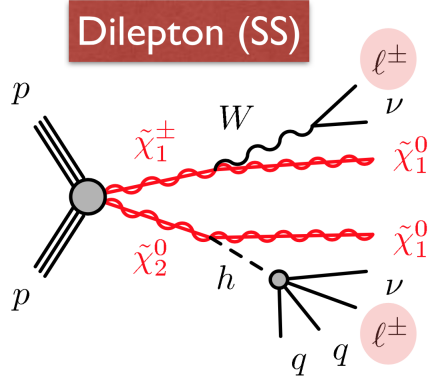


Figure 1.6: The Feynman diagram for the Wh same-sign signal scenario in this thesis. The final states in this process include two same-sign leptons (electron or muon), quarks (i.e. jets) and missing transverse momentum contributed by the lightest neutralinos $\tilde{\chi}_1^0$ and neutrinos ν .

following chapters. With the assumption that all sleptons are heavier than $\tilde{\chi}_1^\pm$ and $\tilde{\chi}_2^0$, $\tilde{\chi}_1^\pm$ decays to W boson and $\tilde{\chi}_1^0$ (i.e. $\tilde{\chi}_1^\pm \rightarrow W^\pm + \tilde{\chi}_1^0$) and $\tilde{\chi}_2^0$ decays to the lightest MSSM Higgs boson h and $\tilde{\chi}_1^0$ (i.e. $\tilde{\chi}_2^0 \rightarrow h + \tilde{\chi}_1^0$), or Z boson and $\tilde{\chi}_1^0$ (i.e. $\tilde{\chi}_2^0 \rightarrow Z + \tilde{\chi}_1^0$). In this thesis, we assume $\tilde{\chi}_1^\pm \rightarrow W^\pm + \tilde{\chi}_1^0$ and $\tilde{\chi}_2^0 \rightarrow h + \tilde{\chi}_1^0$ with 100% branching ratio. The mass of the lightest MSSM Higgs boson h is set to be 125 GeV.

The W boson from $\tilde{\chi}_1^\pm$ decays into one lepton (electron or muon) and one neutrino (i.e. $W^\pm \rightarrow \ell^\pm + \nu$). The Higgs boson from $\tilde{\chi}_2^0$ eventually decays into one lepton (electron or muon), quarks (i.e. jets) and neutrino(s) by various decay modes. For example, $h \rightarrow W^+W^-$ and $h \rightarrow \tau^+\tau^-$ are the dominant decay modes, with one of the W/τ decays leptonically (e.g. $W^\pm \rightarrow \ell^\pm + \nu$) and another decays hadronically (e.g. $W \rightarrow q + q$). Figure 1.6 is the Feynman diagram for the signal process searched in this thesis.

The two leptons in the final states are either electrons or muons, and the term “lepton” (with symbol ℓ) in the following chapters refers to electron or muon, but not tau lepton or neutrino. We search for the final state with exactly two leptons with the same electric charge, which rarely exists in the Standard Model. In the case that mass splitting is close to the mass of Higgs boson, which is called the compressed region, one of the lepton could be very soft that it fails the requirement of the signal lepton, due to the low momentum of the Higgs boson. However, if

the Higgs boson eventually decays into two leptons, for example $h \rightarrow ZZ$ with one of the Z boson decaying leptonically (e.g. $Z \rightarrow \ell^+ + \ell^-$) and another decaying hadronically (e.g. $Z \rightarrow q + q$), the total number of leptons in the final state is three. If one of the three leptons is soft and another two leptons have the same electric charge, this scenario will have the same final state as our signal. This means that in the compressed region, our 2-leptons search channel would be more sensitive than the 3-leptons channel.

Because the two neutralinos $\tilde{\chi}_1^0$ and neutrinos ν in the final state cannot be detected, a large missing transverse momentum (i.e. unbalanced momentum in the detector) is expected.

Chapter 2

Experimental setup

2.1 Introduction

The experimental data were collected from the ATLAS particle detector at the Large Hadron Collider (LHC). The following section will introduce LHC and the ATLAS particle detector.

2.2 The Large Hadron Collider

The Large Hadron Collider (LHC) was built in the border between France and Switzerland by the European Organization for Nuclear Research (CERN). It is a circular particle collider underground with circumference 27 km. Two beams of protons are accelerated in opposite directions, to almost the speed of light, and then collide with each other at the collision point. The energy of each beam is 6.5 TeV, and hence the center-of-mass energy of the two beams \sqrt{s} is 13 TeV, which is the energy used in this experiment. At such a high energy, new physics phenomena are expected, including SUSY. By analyzing the collision events, we can have a deeper understanding of the laws of nature. Figure 2.1 shows the schematic diagram of the CERN accelerator complex, which contains a series of accelerators, from low energy to high energy. The dark blue big circle in figure 2.1 represents the LHC, on which there are 4 particle detectors at 4 different interaction points (yellow points): ATLAS, CMS, LHCb and ALICE.

Before the beam is injected into LHC, the protons are accelerated by a series of accelerators. The journey of the protons starts from a tank of hydrogen gas. The proton and the electron are separated by an electric field. The protons are

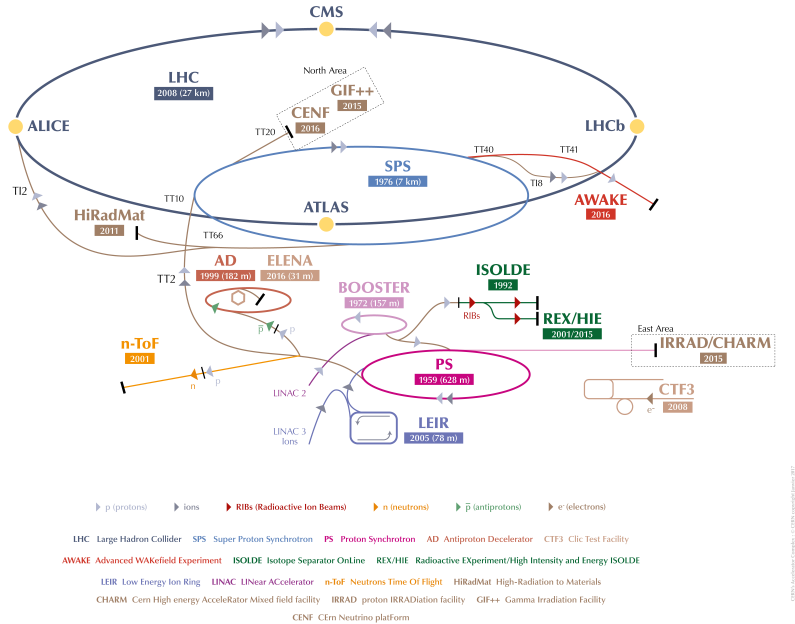


Figure 2.1: The schematic diagram of the CERN accelerator complex, which shows a series of accelerators and facilities [8].

then accelerated to 50 MeV by Linac2, which is a linear accelerator. The beam is then injected to the second accelerator called the Proton Synchrotron Booster (PSB), which accelerates the beam to 1.4 GeV. After then, the beam is injected to the third accelerator called the Proton Synchrotron (PS), which pushes the beam to 25 GeV. The fourth accelerator, called the Super Proton Synchrotron (SPS), further pushes the beam to 450 GeV. Finally, the beam is injected to the two beam pipes of the LHC. One of the beam moves in clockwise direction, while another beam moves in anti-clockwise direction. Two beams collide at the collision point inside the ATLAS detector [20].

The circular path of the proton beam is maintained by many superconducting electromagnets along the LHC tunnel. There are 1232 main magnetic dipoles, and each of them generates a large magnetic field of 8.3 T. In order to generate such a high magnetic field, the coils need to have very high current of 11,080 A, therefore superconducting coil need to be used to reduce the heat loss due to the electrical resistance. The material of superconducting coil is niobium-titanium (NbTi). To reach the condition for superconductivity, the electromagnets operate at a very low temperature, i.e. 1.9 K. There are also 392 magnetic quadrupoles

to squeeze the proton beam, so that the chance of proton-proton collision will be higher [21, 22].

The protons in the beam are grouped into different bunches and there are about 10^{11} protons in each bunch. The time-spacing between two adjacent bunches is 25 ns (or 50 ns in the previous experimental setup). This means that two bunches collide at the collision point in each 25 ns. For each bunch crossing, there are about 10 to 50 proton-proton interactions. Hence, about 10^9 proton-proton collisions are produced per second.

The interacting rate for a physics process $\frac{dN}{dt}$ is the product of the cross section of that physics process σ and the instantaneous luminosity \mathcal{L} .

$$\frac{dN}{dt} = \sigma \mathcal{L} \quad (2.1)$$

The instantaneous luminosity \mathcal{L} is a measure of the interacting rate of two protons at the collision point, which depends on the particle beam parameters. The instantaneous luminosity in this experiment is about $10^{34} \text{ cm}^{-2} \text{ s}^{-1}$ (or $10 \text{ nb}^{-1} \text{ s}^{-1}$).

2.3 ATLAS detector

A Toroidal LHC ApparatuS (ATLAS) is the particle detector used in this experiment [14]. Figure 2.2 shows the main components of the ATLAS detector. Its height is 25 m, its length is 44 m and its weight is 7000 tonnes. The ATLAS detector is a general purpose particle detector, which is consisted of 3 main components: the inner detector, the calorimeter and the muon spectrometer. The heavy and hence short-lived particles will immediately decay into lighter particles. The lighter particles and stable particles pass through different parts of the detectors. These detectors measure the momentum and energy of the particles. Figure 2.3 shows how the ATLAS distinguishes different types of particle by using different components of the detector. The inner detector is surrounded by the solenoid, providing a strong magnetic field. The magnetic field bends the charged particles and the inner detector can detect the paths of the charged particles and measure its momentum. Photons and electrons deposit most of their energy in the electromagnetic calorimeter. Hadrons(including protons and neutrons) and mesons deposit energy in the hadronic calorimeter. Only muons and the neutrinos can reach the outermost muon spectrometer, but only muons can be detected

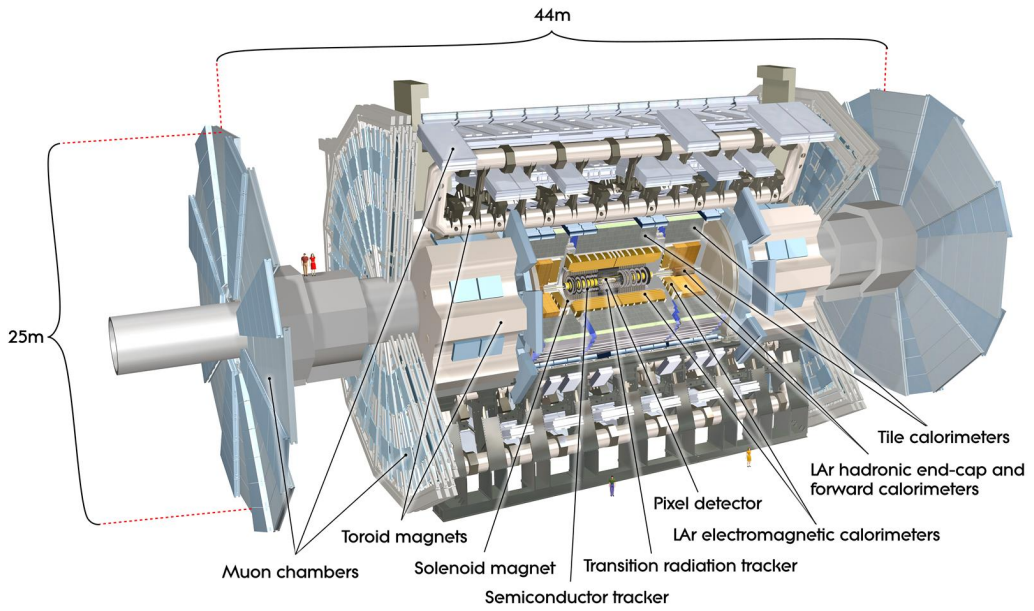


Figure 2.2: The cut-away view of the ATLAS detector. It is 25 m high and 44 m long [9].

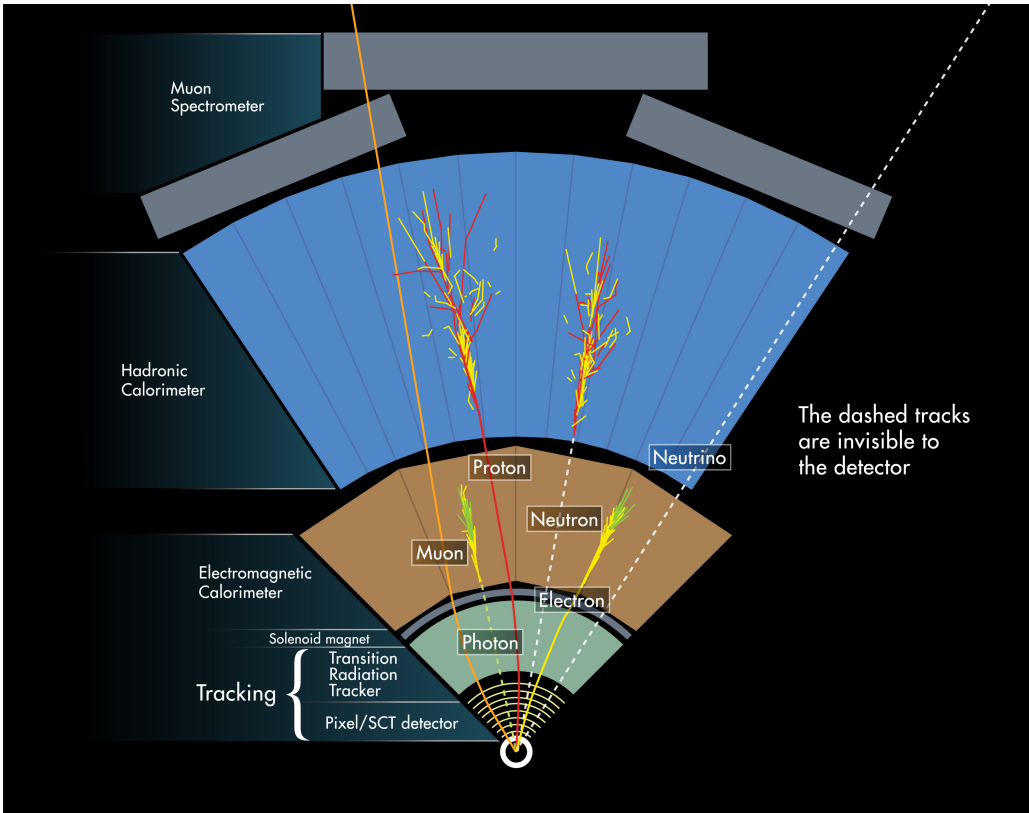


Figure 2.3: The cross section of the ATLAS detector. This shows different components of the ATLAS and how ATLAS detects different types of particles [10].

by the muon spectrometer. Neutrinos escape the ATLAS detector, which leads to missing energy. In this design, different particles can be identified due to their own signature in different parts of ATLAS.

- **Electron** The track of an electron is measured by the inner detector and its energy deposits in the electromagnetic calorimeter.
- **Proton** The tracks of protons are measured by the inner detector and their energies deposit in the hadronic calorimeter.
- **Photon** No track is inside inner detector but its energy deposits in the electromagnetic calorimeter.
- **Neutron** No track is inside inner detector but its energy deposits in the hadronic calorimeter.
- **Muon** The tracks of muons are measured by the inner detector and the muon spectrometer. They nearly do not deposit their energies into the calorimeter and escape the detector.
- **Neutrino** Neutrinos cannot be detected, which contributes to the missing momentum.

2.3.1 The coordinate system and basic variables

The nominal collision point is defined as the origin of the coordinate system. The z-axis is along the anticlockwise beam direction. The positive x-axis is pointing to the centre of the LHC ring. The positive y-axis is in the upward direction. The ATLAS detector is symmetric about the x-y plane.

The impact parameters of the track of a particle are z_0 and d_0 , described in figure 2.4. The nearest point of the track to the z-axis is marked by the small circle in the figure, with the smallest distance d_0 . The z-coordinate of the nearest point is z_0 .

The figure also shows the momentum \mathbf{p} of the particle when it passes through the nearest point. The azimuthal angle ϕ and the polar angle θ of the momentum \mathbf{p} are defined as usual in the spherical coordinate system. The polar angle θ is the angle between the momentum \mathbf{p} and the positive z-direction. The pseudorapidity η is defined as:

$$\eta = -\ln \left(\tan \frac{\theta}{2} \right) \quad (2.2)$$

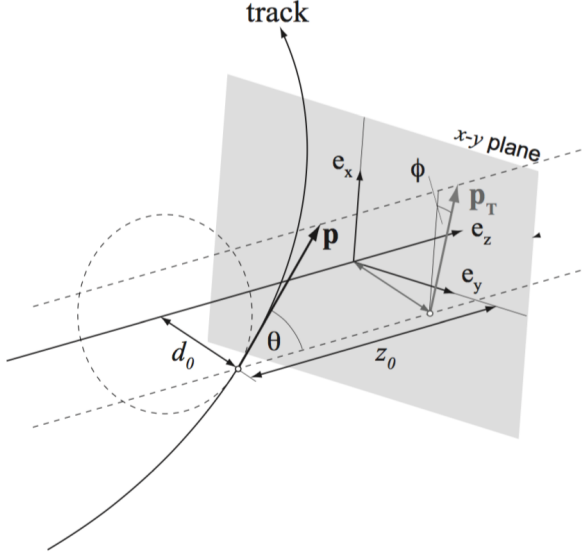


Figure 2.4: This figure shows how the impact parameters z_0 and d_0 are defined by the nearest point (the small circle) of the track to the z -axis. It also shows how the azimuthal angle ϕ and the polar angle θ of the momentum \mathbf{p} are defined. p_T is the projection of the momentum \mathbf{p} onto the x - y plane.

Different polar angles θ corresponding to different values of pseudorapidity η are shown in figure 2.5. The positive values of pseudorapidity η correspond to $0 < \theta < \frac{\pi}{2}$, while the negative values of pseudorapidity η correspond to $\frac{\pi}{2} < \theta < \pi$. The values of pseudorapidity η are reflective symmetric about the x - y plane.

$$(\eta \text{ at } \theta = \pi - x) = -\ln \left(\tan \frac{\pi - x}{2} \right) \quad (2.3)$$

$$= -\ln \left(\tan \left(\frac{\pi}{2} - \frac{x}{2} \right) \right) \quad (2.4)$$

$$= -\ln \left(\frac{1}{\tan \frac{x}{2}} \right) \quad (2.5)$$

$$= -\left(-\ln \left(\tan \frac{x}{2} \right) \right) \quad (2.6)$$

$$= -(\eta \text{ at } \theta = x) \quad (2.7)$$

The ATLAS detector covers the region where $|\eta| < 4.9$, but the reconstructed objects are often restricted to $|\eta| < 2.5$.

The projection of the nearest point onto the x - y plane is also shown in figure 2.4. The transverse momentum of a particle, denoted by \mathbf{p}_T , is the projection of its momentum \mathbf{p} onto the x - y plane, as shown in the figure. The azimuthal angle ϕ of the momentum \mathbf{p} is the azimuthal angle of \mathbf{p}_T in the two-dimensional polar

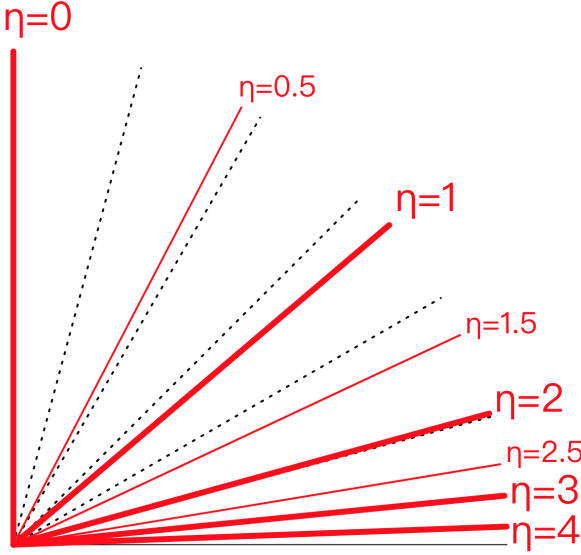


Figure 2.5: The red lines show different directions corresponding to different positive values of pseudorapidity [11].

coordinate system on the x-y plane. The magnitude of \mathbf{p}_T is denoted by p_T .

$$p_T = \sqrt{p_x^2 + p_y^2} \quad (2.8)$$

In the following chapter, the term “transverse momentum” p_T refer to the magnitude of \mathbf{p}_T .

The distance ΔR in the pseudorapidity-azimuthal angle space of two particles is defined as:

$$\Delta R = \sqrt{(\Delta\phi)^2 + (\Delta\eta)^2} \quad (2.9)$$

It measures the angular separation of the momentum of two particles.

2.3.2 The magnetic system

There is a thin superconducting solenoid magnet around the inner detector, which generates a 2 T magnetic field in the z-direction inside the inner detector. There are also 3 large superconducting toroids around the calorimeter: one for barrel and two for end-caps. Each toroid consists of eight coils arranged symmetrically, which provide magnetic field in the ϕ -direction for the muon spectrometer. The end-cap toroids are rotated by 22.5° relative to the barrel toroid, in order to optimize the magnetic field at the region between the two coil systems. The strength of the magnetic field is 0.5 T in the barrel region and 1 T in the end-cap region. All these magnets are shown in figure 2.6.

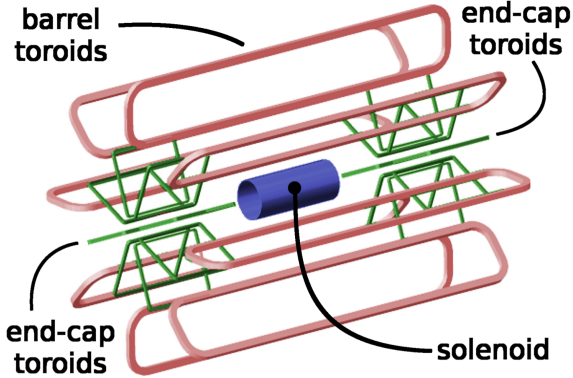


Figure 2.6: Schematic view of the magnetic system of the ATLAS detector [12].

2.3.3 The inner detector

The inner detector is a particle tracker. For each collision, thousands of particles will be produced within $|\eta| < 2.5$. It measures the tracks of charged particles, the momentum of the charged particles and the position of the vertices. Figure 2.7 shows the whole structure of the inner detector. The inner detector consists of 3 sub-detectors from inner to outer: the pixel detector, the silicon microstrip tracker (SCT) and the transition radiation tracker (TRT). Each part further divides into two parts: the barrel region with small $|\eta|$ and the end-cap region with large $|\eta|$. Figure 2.8 shows the radius R of the 3 sub-detectors from the beam, and figure 2.9 shows the shapes and the orientations of each sensor and the η coverage, in both the barrel and the end-cap regions. The η coverage for the inner detector is $|\eta| < 2.5$. The shapes and the orientations of the sensors are different in the barrel and the end-cap regions. In the barrel region, the shape and the orientation of the sensors is concentric cylinder shells around the beam axis, while in the end-cap region, they are disks perpendicular to the beam axis.

The precision tracking detectors (pixels and SCT) has high resolution in space by using discrete space-points to detect the track of a charged particle, with the cutting-edge technology, in order to achieve the good performance of the inner detector. When the particle moves inside the inner detector, there are averagely 36 hits per track. By recording the positions of these hits, the path of the particle can be reconstructed. The whole inner detector is immersed in a 2 T magnetic field generated by the solenoid magnet, therefore the path of any charged particles will be bent. By measuring the curvature of the path, the charge and momentum

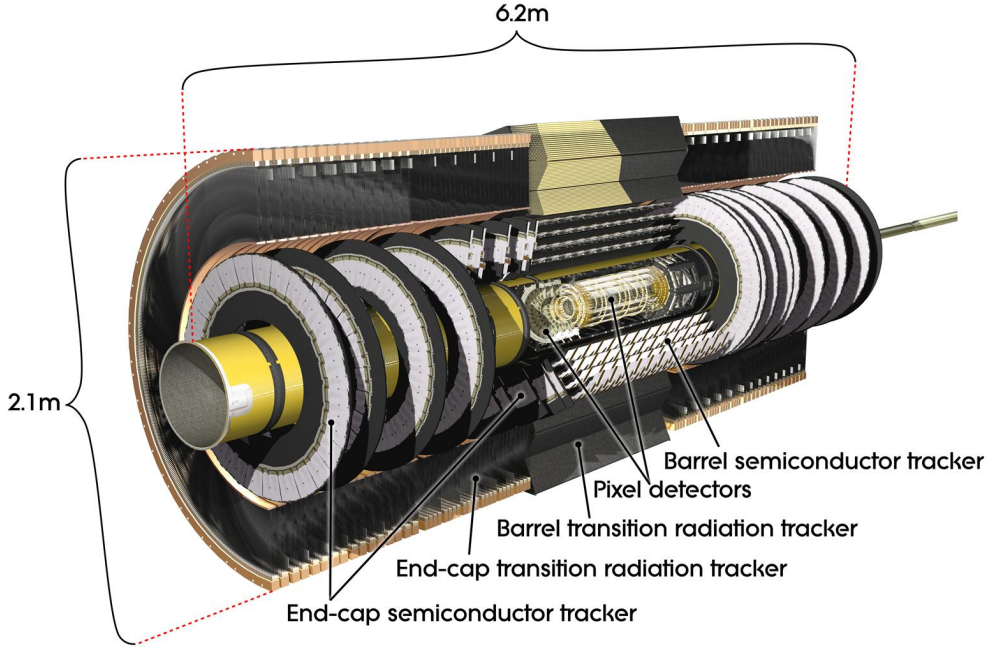


Figure 2.7: The whole structure of the ATLAS inner detector [13].

of the particle are measured. The equation for the circular path is

$$\frac{d\mathbf{p}}{dt} = q(\mathbf{v} \times \mathbf{B}) \quad (2.10)$$

where the relativistic momentum $\mathbf{p} = \gamma m \mathbf{v}$.

$$\frac{d\mathbf{p}}{dt} = q\left(\frac{\mathbf{p}}{\gamma m} \times \mathbf{B}\right) \quad (2.11)$$

$$= \frac{q}{\gamma m}(\mathbf{p} \times \mathbf{B}) \quad (2.12)$$

From this equation, we can get the angular frequency ω ,

$$\omega = \frac{qB}{\gamma m} \quad (2.13)$$

$$\frac{v}{r} = \frac{qB}{\gamma m} \quad (2.14)$$

$$\frac{1}{r} = \frac{qB}{\gamma mv} \quad (2.15)$$

$$\frac{1}{r} = \frac{qB}{p} \quad (2.16)$$

$$p = rqB \quad (2.17)$$

We can calculate the momentum of the particle from the curvature of track $1/r$, the charge and the magnetic field strength.

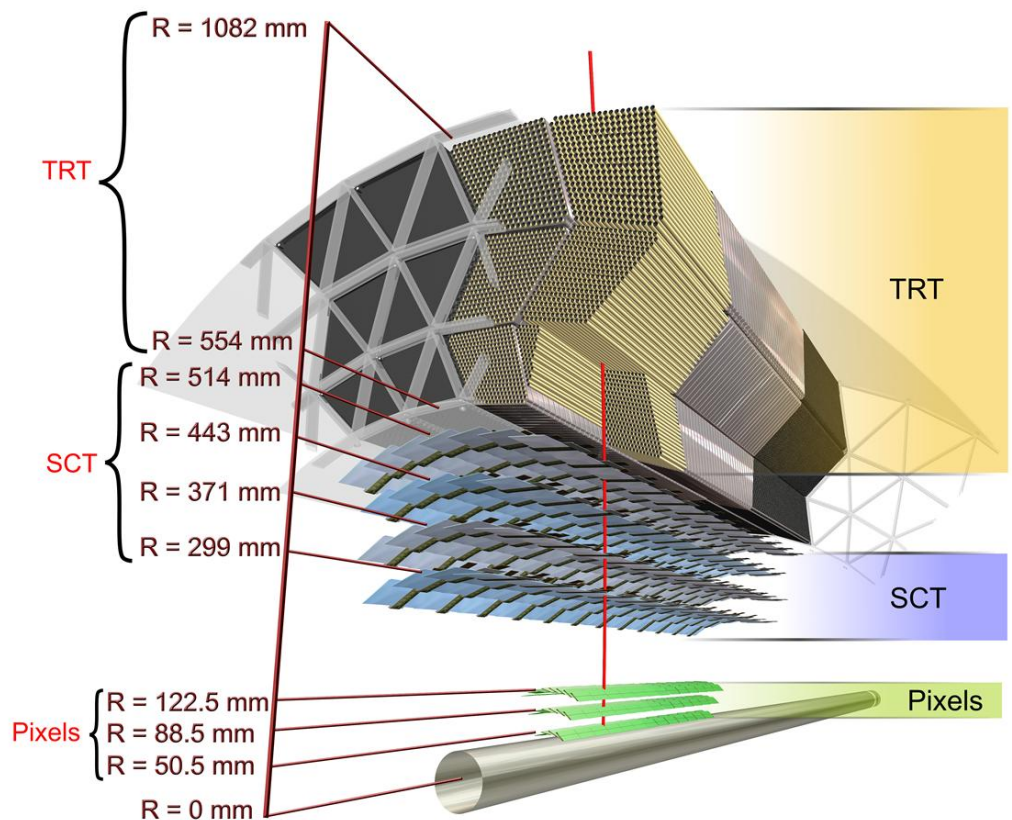


Figure 2.8: The radius R from the beam for the 3 components: pixel, SCT and TRT [13].

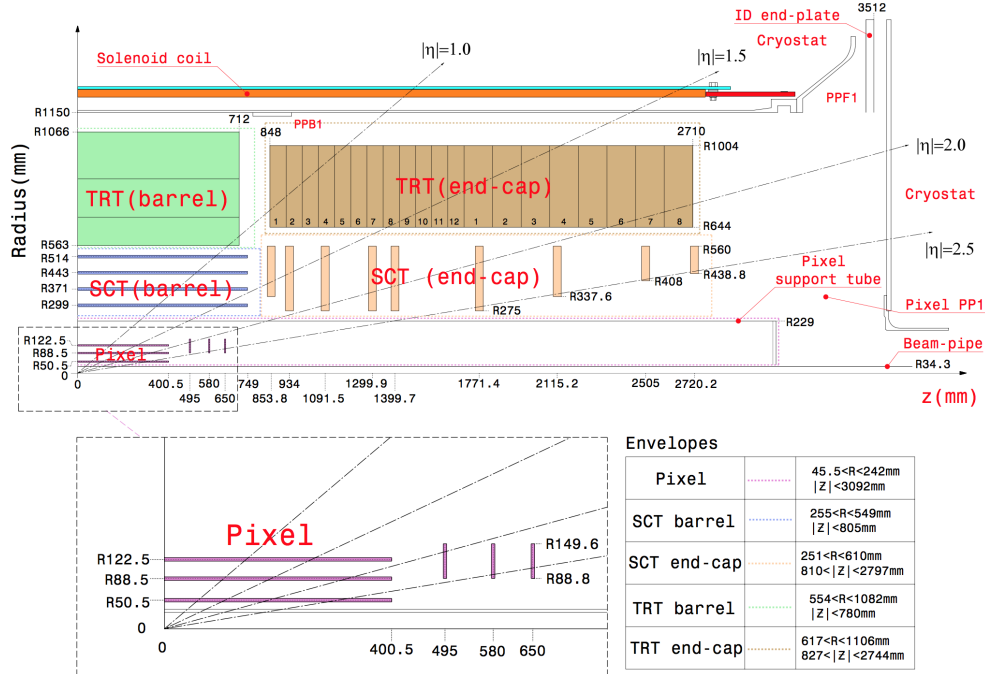


Figure 2.9: The shapes, the orientations and the η coverage for each sensor [14].

2.3.3.1 Pixel detector

The pixel detector is the innermost part of the inner detector, therefore it has to withstand the highest amount of radiation from the interaction point. As shown in figure 2.9, there are 3 layers of cylinder in the barrel region at radii 50.5 mm, 88.5 mm and 122.5 mm, and 3 layers of disk for each end-cap region at $z = 495$ mm, 580 mm and 650 mm. There are in total 1744 modules in the pixel detectors. Each module is identical, and has the size of $19\text{mm} \times 63\text{mm}$. The module has 47232 pixels, with the size of $50\mu\text{m} \times 400\mu\text{m}$. There are in total 80 million pixels for the whole pixel detector. Each pixel measures the position with an accuracy of $10\mu\text{m} \times 115\mu\text{m}$.

The sensors in the module are made with planar n^+ -in- n type of silicon with $250\ \mu\text{m}$ thick, where n^+ -type at the readout side (i.e. the electronics chip) and n -type at another side. When charged particles pass through the silicon, electrons are produced and attracted to the anode, which is attached to an electronics chip with $180\ \mu\text{m}$ thick.

The innermost layer of pixels at radius 50.5 mm is very important for measuring the secondary vertices of the long-lived b-hadrons. It helps identify the b-jets (jets originating from bottom quarks), which are the decay products of the top

quarks and Higgs bosons.

2.3.3.2 SCT

The SCT is in the middle part of the inner detector. As shown in figure 2.9, there are 4 layers of cylinder in the barrel region and 9 layers of disk for each end-cap region. There are 4088 modules in the SCT and 6.3 million pixels. Each module has the thickness of $300\ \mu\text{m}$. It has a thermally conductive base-board in the middle, which provides the cooling of the sensor. The p-in-n silicon sensors are glued on each side of the base-board. The working principle is similar to the pixel detector. Each sensor has the spatial resolution of $17\mu\text{m} \times 580\mu\text{m}$.

2.3.3.3 TRT

The TRT is the outermost part of the inner detector. It detects the track of the charged particle, and help distinguishing the electrons from other charged hadrons. It is a straw tube gaseous detector, with 96 TRT modules in the barrel and 20 TRT modules on each end-cap. There are 52544 straws in the barrel and 122880 straws in the end-cap. Each straw tube is a polyimide drift straw tube with 144 cm long and 4 mm diameter. It is filled with a non-flammable gas mixture of 70% Xe, 27% CO₂ and 3% O₂. When a charged particle passes through the gas, it ionizes the gas and produces transition radiation. The transition radiation further ionizes the gas and produces free electrons, which are attracted to the wire at the center of the straw tube. The electrons can be identified by detecting the amount of transition radiation, because electrons emit more transition radiation than other charged hadrons, like pions.

The TRT has the spatial resolution of $130\mu\text{m}$ in the R- ϕ plane. The spatial resolution of z is determined by the length of the straw tube, i.e. 144 cm.

2.3.4 Calorimeter

The calorimeter measures the energy of the particle. Besides the measurement of the energy of the particles, it also helps identifying different particles like electrons, photons and jets. It is because different particles have different signature when the particle deposits its energy to the calorimeters. It contains two types of calorimeters: the electromagnetic calorimeter and the hadronic calorimeter. The electromagnetic calorimeter is designed to measure the energy of electrons and

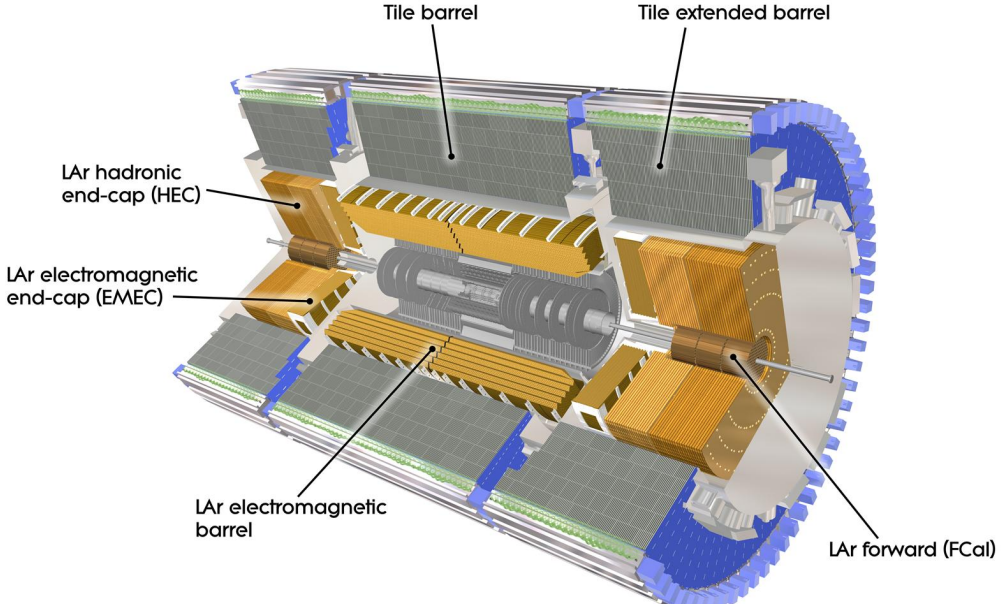


Figure 2.10: Schematic view for the calorimeter system of the ATLAS detector [15].

photon, while the hadronic calorimeter is to measure the energy of the hadrons like protons, neutrons and mesons. The figure 2.10 shows the calorimeter system of the ATLAS detector. In the barrel region, the Liquid Argon (LAr) electromagnetic calorimeter (ECal) works as an electromagnetic calorimeter, while the tile calorimeter (TileCal) works as a hadronic calorimeter. In the end-cap region, the LAr ElectroMagnetic End-Cap (EMEC) calorimeter works as an electromagnetic calorimeter, while the LAr Hadronic End-Cap (HEC) calorimeter works as a hadronic calorimeter. In the forward region, the LAr Forward Calorimeter (FCal) has three layers: one is electromagnetic and two are hadronic. Figures 2.11 and 2.12 show the schematic view for one side of the end-cap and forward calorimeter. The large coverage $|\eta| < 4.9$ is to ensure a good measurement of the missing energy (E_T^{miss}).

2.3.4.1 Electromagnetic calorimeter

In the barrel region, it covers $|\eta| < 1.457$. In the end-cap region, there are two concentric wheels, with the outer one covering from $1.375 < |\eta| < 2.5$ and the inner one covering from $2.5 < |\eta| < 3.2$. The EM calorimeter is alternately

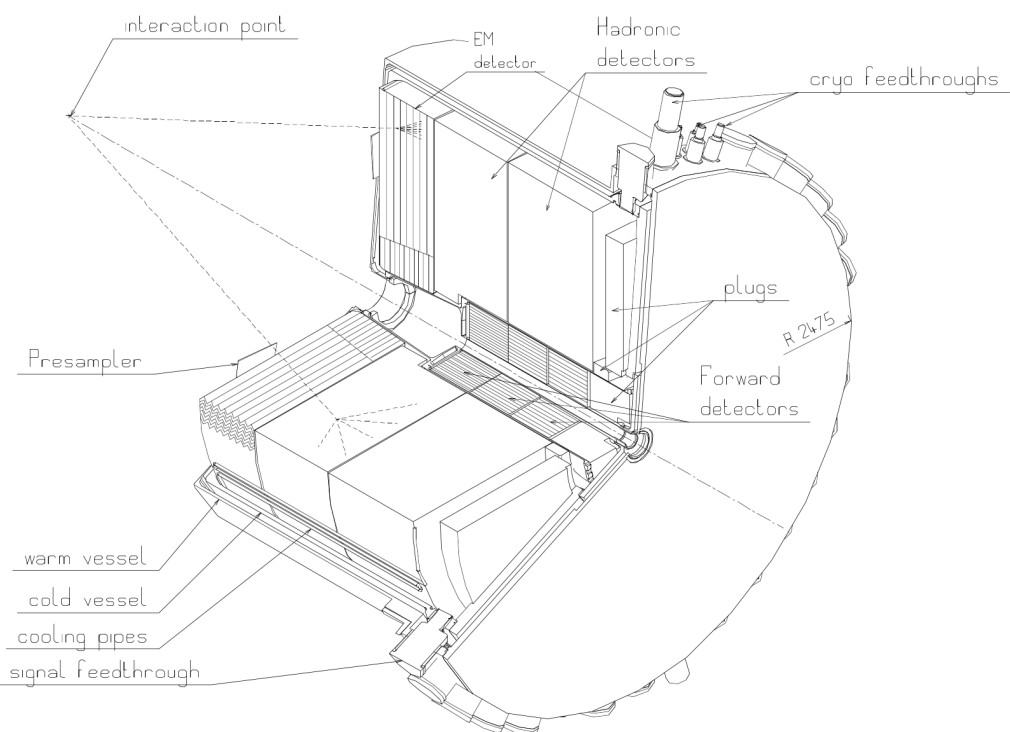


Figure 2.11: Schematic view for one side of the end-cap and forward calorimeter [16].

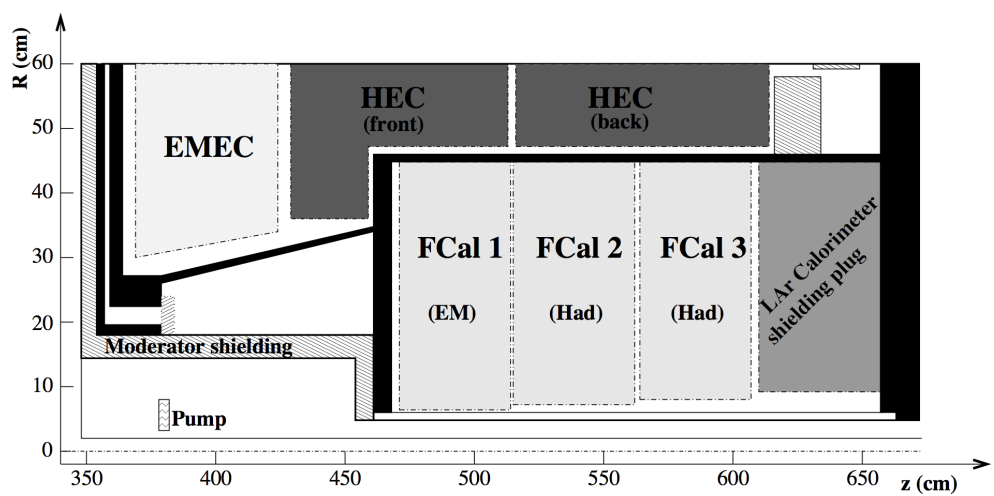


Figure 2.12: Schematic view for one side of the end-cap and forward calorimeter. One layer of forward calorimeter is electromagnetic and two are hadronic [14].

interleaved with many accordion-shaped layers of electrodes and absorbers, and is filled with liquid argon between the layers at -185°C . The accordion geometry provides complete ϕ symmetry without azimuthal cracks. A layer of absorbers is made of a lead plate, to which two stainless-steel sheets (0.2 mm thick) are glued on both sides. The thickness of the lead plate is 1.53 mm for $|\eta| < 0.8$ and 1.13 mm for $|\eta| > 0.8$ in the barrel region, and 1.7 mm for $|\eta| < 2.5$ and 2.2 mm for $|\eta| > 2.5$ in the end-cap region. A layer of electrode is made of three conductive copper layers, which are separated by insulating polyimide sheets. When high energy electrons or photons pass through the lead absorbers, a shower of lower energy electrons, positrons and photons is produced. The liquid argon atoms, as an active material, are ionized by the particles in the shower. Therefore, free electrons are produced and attracted to the electrode. By measuring the current from the electrode, the energy of the electron or photon are measured.

The lead absorber can further reduce the energy of particles in the shower before they escape the calorimeter. Hence, only part of the energy is measured and a correction need to be applied. The innermost layer, called the presampler, help calculate the correction due to the energy lost.

The EM calorimeter has a fine granularity to have precise energy measurements for electrons and photons. The granularity depends on the layers, as shown in figure 2.13. Besides the layer of presampler, there are two or three layers (Layer 1, Layer 2 and Layer 3), depending on the $|\eta|$. In the region of $|\eta| < 2.5$, three layers are often used for precise measurements. Table 2.1 and 2.2 show the granularity for each layers in the barrel region and the end-cap region respectively.

Layer	$ \eta $ range	Granularity $\Delta\eta \times \Delta\phi$
Presampler	$ \eta < 1.52$	0.025×0.1
Layer 1	$ \eta < 1.4$	0.003×0.1
	$1.4 < \eta < 1.475$	0.025×0.025
Layer 2	$ \eta < 1.4$	0.025×0.025
	$1.4 < \eta < 1.475$	0.075×0.025
Layer 3	$ \eta < 1.35$	0.050×0.025

Table 2.1: The granularity in η and ϕ for different layers in the barrel region [14].

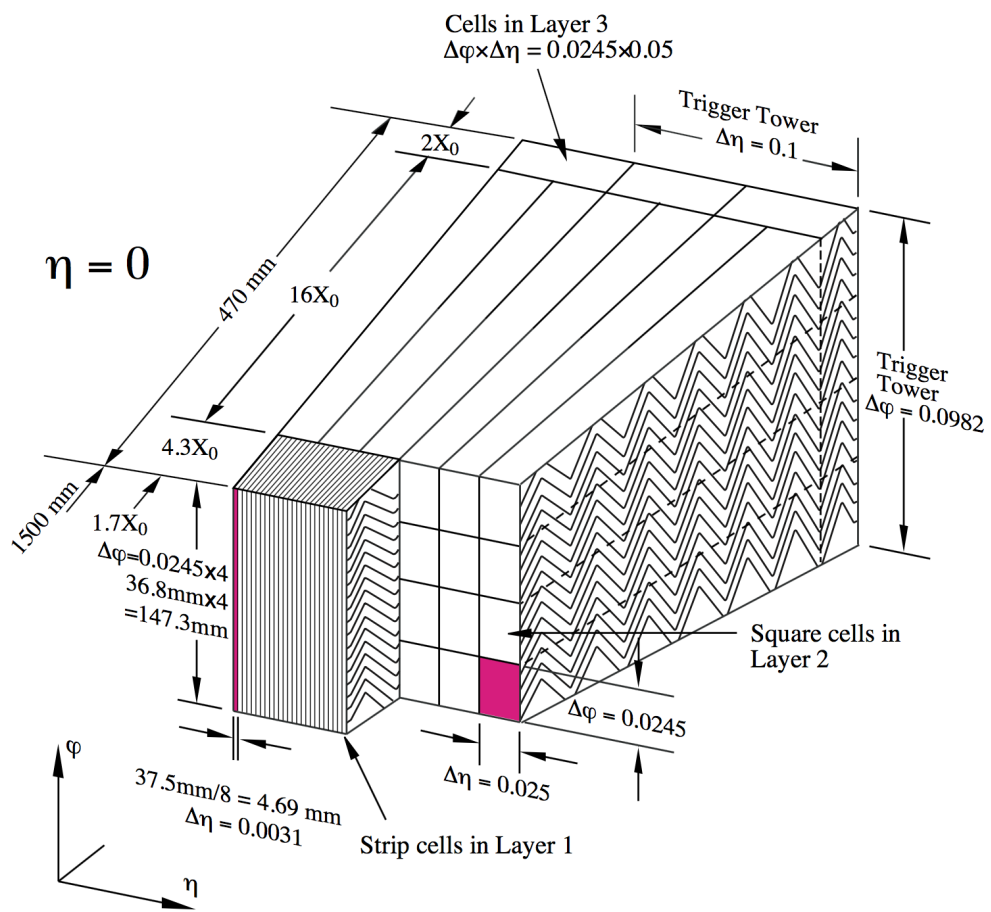


Figure 2.13: The granularity in η and ϕ of the cells of each of the three layers in the electromagnetic calorimeter [14].

Layer	$ \eta $ range	Granularity $\Delta\eta \times \Delta\phi$
Presampler	$1.5 < \eta < 1.8$	0.025×0.1
Layer 1	$1.375 < \eta < 1.425$	0.050×0.1
	$1.425 < \eta < 1.5$	0.025×0.1
	$1.5 < \eta < 1.8$	0.003×0.1
	$1.8 < \eta < 2.0$	0.004×0.1
	$2.0 < \eta < 2.4$	0.006×0.1
	$2.4 < \eta < 2.5$	0.025×0.1
	$2.5 < \eta < 3.2$	0.1×0.1
Layer 2	$1.375 < \eta < 1.425$	0.050×0.025
	$1.425 < \eta < 2.5$	0.025×0.025
	$2.5 < \eta < 3.2$	0.1×0.1
Layer 3	$1.5 < \eta < 2.5$	0.050×0.025

Table 2.2: The granularity in η and ϕ for different layers in the end-cap region [14].

2.3.4.2 Hadronic calorimeter

In the barrel region, tile calorimeter is used for measuring the energy of the hadrons in $|\eta| < 1.7$. The central barrel covers $|\eta| < 1.0$, while the extended region covers $0.8 < |\eta| < 1.7$. As shown in figure 2.14, the tile calorimeter is alternately interleaved with sheets of steel and scintillator, called tile, like a sandwich. The steel acts as the absorber material, while the scintillator acts as the active material. When high energy hadrons pass through the sheets of steel, they strongly interact with the atomic nuclei of the steel, and produce a shower of lower energy charged particles, which then triggers the scintillators to produce photons. These photons are collected by the wavelength-shifting fibres on the edges of the tile. The photomultiplier tubes (PMT) then convert the optical signal to an electronic signal. By measuring the intensity of the photons, the energy of the hadron are measured. There are 3 layers in the tile calorimeter. The granularity of the first 2 layers is $\Delta\eta \times \Delta\phi = 0.1 \times 0.1$, while the third layer is $\Delta\eta \times \Delta\phi = 0.2 \times 0.1$.

In the end-cap region $1.5 < |\eta| < 3.2$, there are two independent wheels of LAr hadronic calorimeters (HEC) for each end-cap, i.e. the front wheel and the back wheel as shown in figure 2.12. For each wheel, it consists of 32 identical

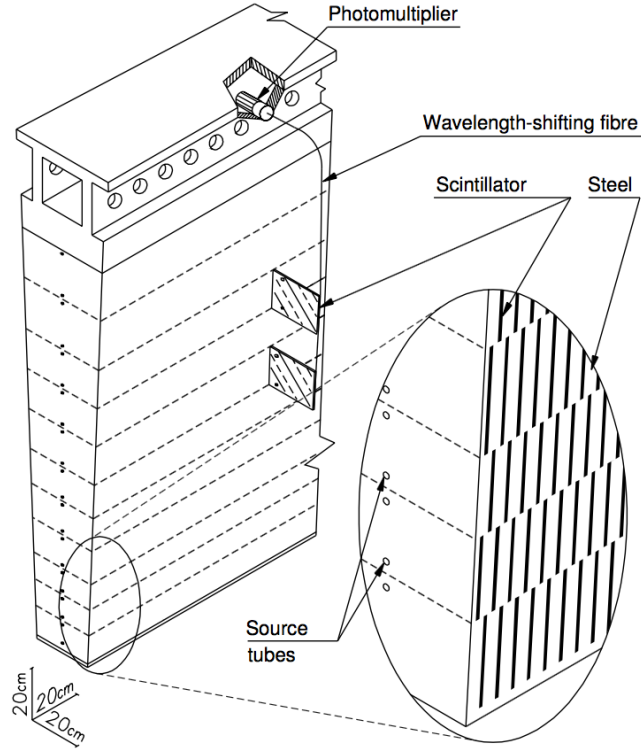


Figure 2.14: Schematic view of one module of the tile calorimeter [14].

wedge-shaped modules and each module has two layers. Hence, in total, there are 4 layers for each end-cap. Similar to the electromagnetic calorimeter, it uses the liquid argon as the active material, but it uses flat parallel copper plates as the absorber material. On the front wheel, there are 24 copper plates with 25 mm thick. On the back wheel, there are 16 copper plates with 50 mm thick. The gap between the copper plates is 8.5 mm. As shown in figure 2.15, the gap is separated by three electrodes and is filled with liquid argon. The granularity is $\Delta\eta \times \Delta\phi = 0.1 \times 0.1$ at $1.5 < |\eta| < 2.5$, and $\Delta\eta \times \Delta\phi = 0.2 \times 0.2$ at $2.5 < |\eta| < 3.2$.

2.3.4.3 Forward calorimeter

The LAr Forward calorimeter (FCal) covers $3.1 < |\eta| < 4.9$, with 3 wheels: FCal 1, FCal 2 and FCal 3. FCal 1 is an electromagnetic calorimeter and uses copper as the absorber material. FCal 2 and FCal 3 are hadronic calorimeters and use tungsten as the absorber material. It uses the liquid argon as the active material.

Due to the high $|\eta|$ and the close distance to the interaction point (4.7 m), the forward calorimeters are exposed to high particle fluxes. This results in a new

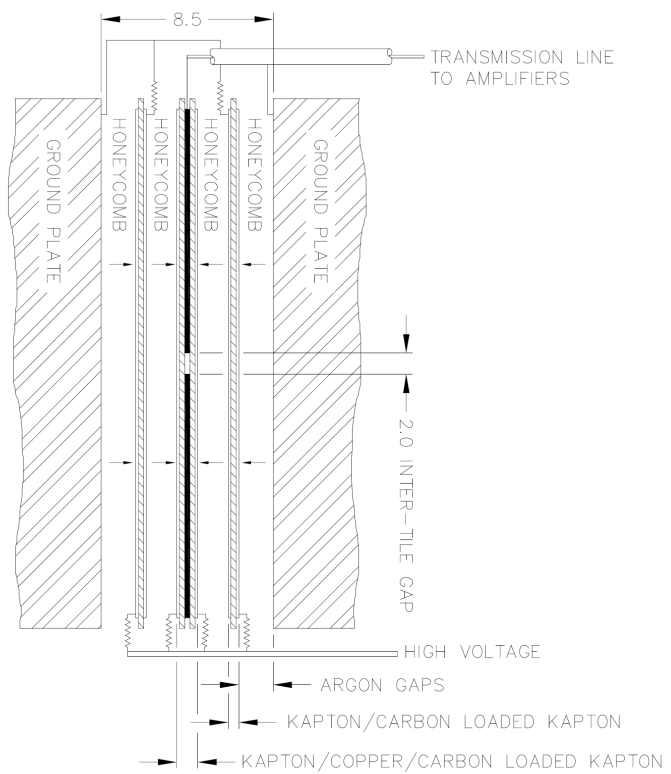


Figure 2.15: Schematic view of the arrangement of the HEC readout structure in the 8.5 mm inter-plate gap. All dimensions are in mm [14].

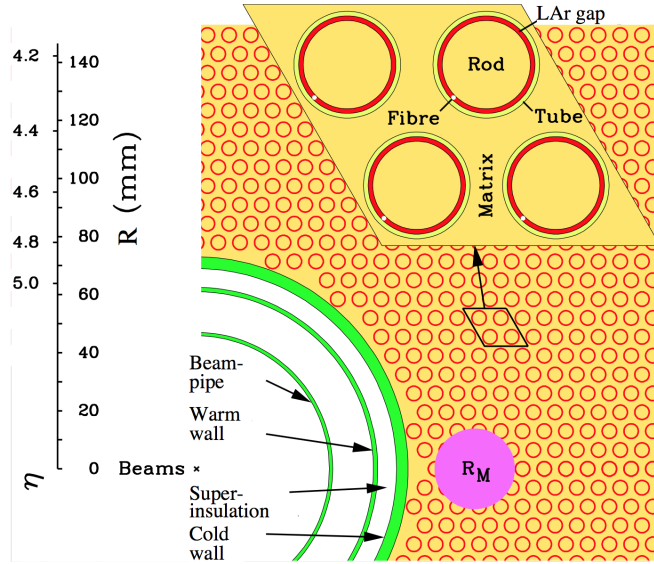


Figure 2.16: Electrode structure of FCal 1 with the matrix of copper plates and the copper tubes and rods with the LAr gap for the electrodes. The Molière radius, R_M , is represented by the solid disk [14].

design with a small gap of liquid argon to avoid the ion build-up problems. Figure 2.16 shows the structure of FCal 1. A matrix of copper plates is filled inside the forward calorimeter, with 12260 regularly spaced electrodes parallel to the beam direction. In the electrodes, there are concentric copper rods and copper tubes. The gap between rod and tube is filled with a thin layer of liquid argon with thickness 0.269 mm.

For FCal 2 and FCal 3, there are 10200 and 8224 electrodes respectively. The structure is similar to FCal 1, but the copper rods are replaced by the tungsten rods and the matrix of copper plates is replaced by a matrix of tungsten alloy. The tungsten rod is surrounded by a copper tube with the gap filled with liquid argon. The thickness of the liquid argon of FCal 2 and FCal 3 are 0.376 mm and 0.508 mm respectively. The granularity of the forward calorimeter in the x-y plane is shown in 2.3.

A shielding plug made of a copper alloy has been mounted behind the FCal 3 to further reduce the backgrounds that reach the muon spectrometer.

Layer	$ \eta $ range	Granularity $\Delta x \times \Delta y$ (cm)
FCal 1	$3.15 < \eta < 4.30$	3.0×2.6
	$3.10 < \eta < 3.15$	\sim four times finer
	$4.30 < \eta < 4.83$	\sim four times finer
FCal 2	$3.24 < \eta < 4.50$	3.3×4.2
	$3.20 < \eta < 3.24$	\sim four times finer
	$4.50 < \eta < 4.81$	\sim four times finer
FCal 3	$3.32 < \eta < 4.60$	5.4×4.7
	$3.29 < \eta < 3.32$	\sim four times finer
	$4.60 < \eta < 4.75$	\sim four times finer

Table 2.3: The granularity in the x-y plane in the forward calorimeter [14].

2.3.5 Muon spectrometer

The muon spectrometer is a tracker for muons. In the barrel region ($|\eta| < 1.4$), the magnetic field is provided by the barrel toroid, described in section 2.3.2. In the end-cap region ($1.6 < |\eta| < 2.7$), the magnetic field is provided by the end-cap toroid. In the transition region ($1.4 < |\eta| < 1.6$), the magnetic field is provided by the combined field from the two toroids.

Figure 2.17 shows all the components in the muon spectrometer. The tracking detector is made up of the Monitored Drift Tube chambers (MDT), in the range of $|\eta| < 2.7$. In the barrel region, the track of a muon is measured by three cylindrical layers of MDT located at $R = 5$ m, 7.5 m and 10 m, as shown in figure 2.18. Each layer has 8 large chambers and 8 small chambers. In the end-cap and the transition region, there are four wheels of MDT, located at $|z| = 7.4$ m, 10.8 m, 14 m and 21.5 m, as shown in figure 2.19. For the naming scheme of MDT chambers, the first letter (B and E) refers to the barrel and end-cap chambers respectively. The second letter (I, E, M and O) refers to the inner, extra, middle and outer layers respectively. The third letter (L and S) refers to the large and small chambers respectively.

The total number of drift tubes in each MDT chamber is about 200 to 500 depending on the type of the chamber. The lengths of the drift tubes vary from 0.85 m to 6.24 m. The tube is made of aluminium with a diameter of 29.970 mm as shown in figure 2.20. It is filled with a gas mixture of 93% argon and 7% CO₂,

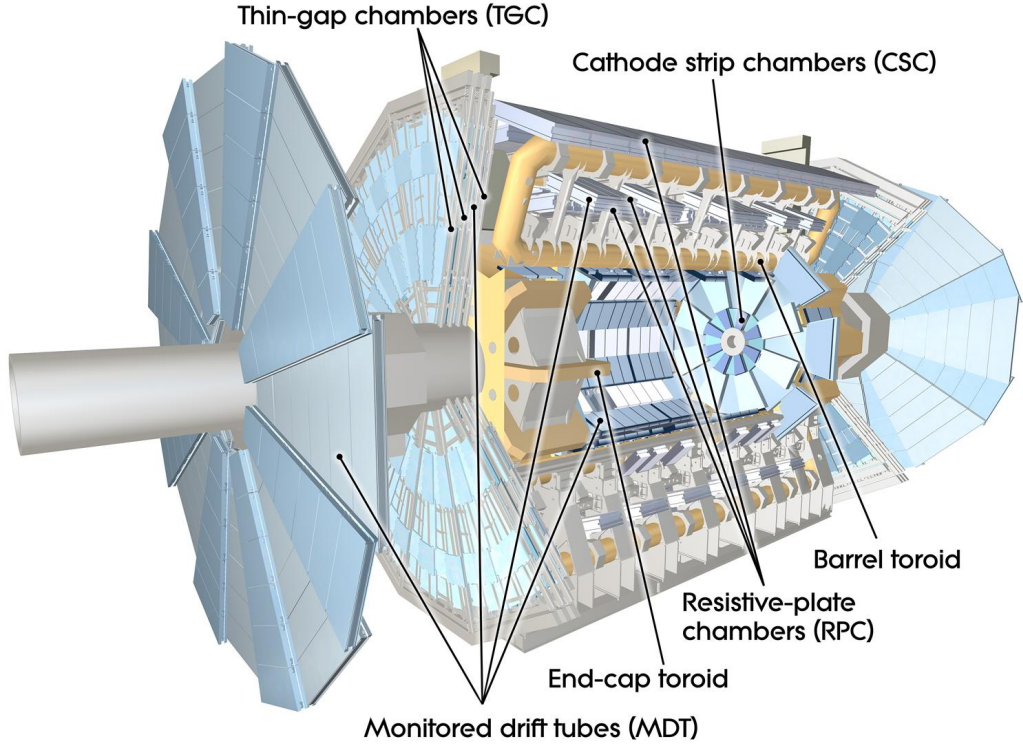


Figure 2.17: Cut-away view of the muon spectrometer [17].

operated at a pressure of 3 bar. The anode wire is made of tungsten-rhenium with a diameter of $50 \mu\text{m}$, at an electric potential of 3080 V. When muons pass through the tube, the gas is ionized and free electrons are produced, which are attracted and drift to the anode wire. By measuring the drift time the free electrons take from the position of the muon to the anode wire, the position of the muon can be measured. The average resolution of the MDT is $80 \mu\text{m}$ per tube, or about $35 \mu\text{m}$ per chamber.

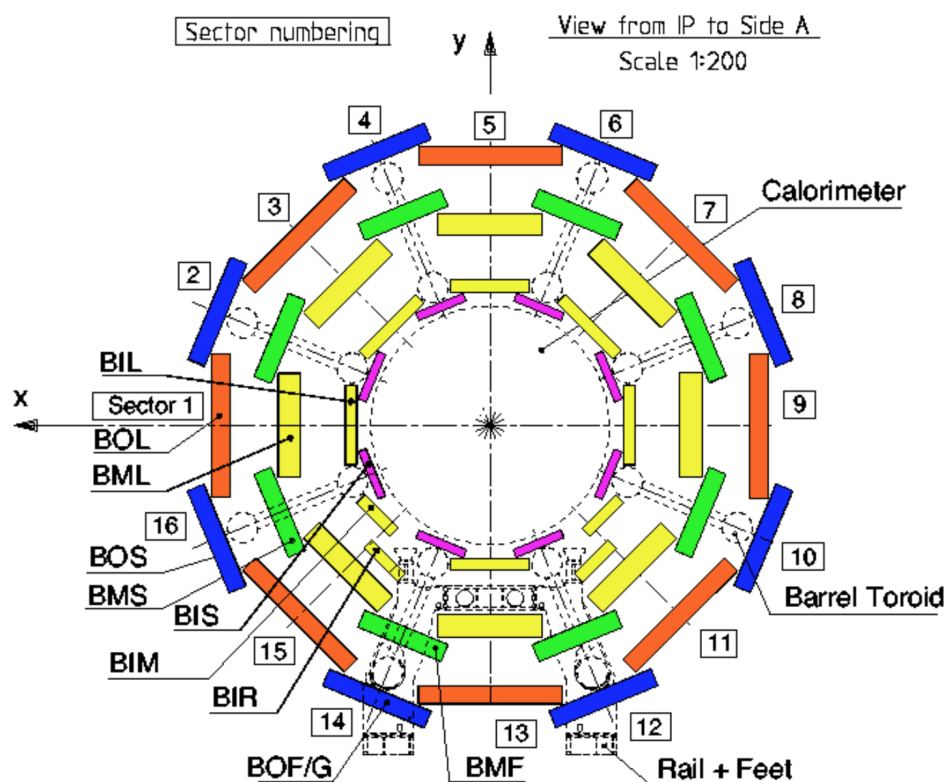


Figure 2.18: The cross section of the barrel region for the muon spectrometer. Three concentric cylindrical layers of barrel MDT are shown [14].

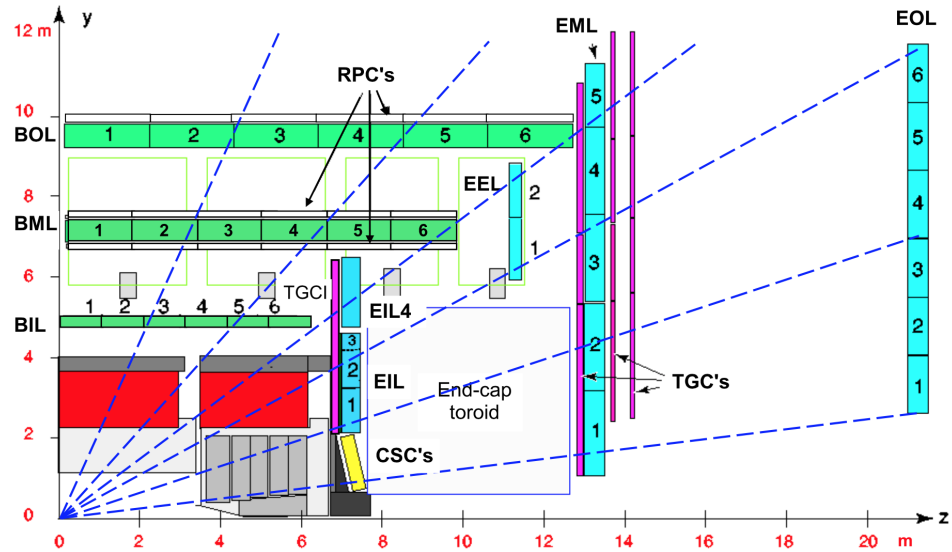


Figure 2.19: The cross section of the end-cap region for the muon spectrometer. Four layers of end-cap MDT are shown in blue colour. Three layers of barrel MDT are also shown in green colour [14].

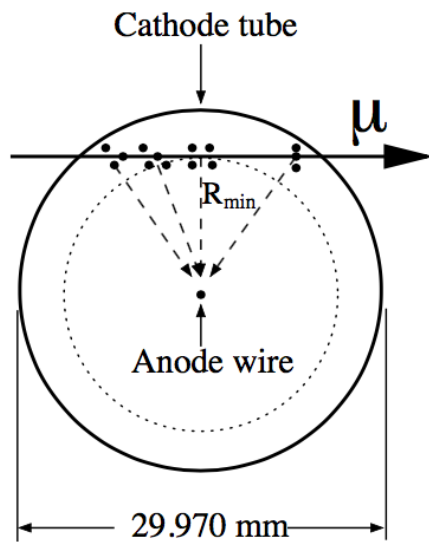


Figure 2.20: The cross-section of a MDT tube. When muons pass through the tube, free electrons are produced along the track, which drift to the anode wire [14].

Chapter 3

Dataset and event selection

3.1 Dataset

The dataset contains the data samples and Monte-Carlo(MC) simulated sample.

3.1.1 Data samples

We use 2015 and 2016 pp -collisions data samples, at $\sqrt{s} = 13$ TeV. Only events in good conditions are used, where LHC beams were stable and all ATLAS detectors were in good state. These good events are summarised in the Good Run Lists. The two Good Run Lists (GRL) in 2015 and 2016 data are shown in the section [A.1](#). The integrated luminosities in 2015 and 2106 are 3.21 fb^{-1} and 32.86 fb^{-1} respectively, with relative error 2.1%. The list of data samples used in this analysis is shown in the section [A.1](#).

3.1.2 MC samples

3.1.2.1 SM background

All MC samples are mc15c samples with offline release 20.7. All the background MC samples used in this analysis for each process are shown in the section [A.2](#) in appendix. The cross section, k-factor, generator efficiency and its equivalent integrated luminosity for each sample are listed.

t \bar{t} and single top The simulated events are generated by the POWHEG generator, and the CT10 PDF set is used. PYTHIA6 is also used for the parton shower model, with the PERUGIA 2012 tune. The mass of the top quark is assumed to be

172.5 GeV. The $t\bar{t}$ samples are normalized to the next-to-next-to-leading order of cross section, while the single top samples are normalized to the next-to-leading order of cross section.

W+jets and Z+jets The simulated events are generated by the SHERPA v2.2.1. The matrix elements are calculated at the next-to-leading order for up to two partons, and at the leading order for up to four partons, by using the COMIX and OPENLOOPS generators. The samples are normalized to the next-to-next-to-leading order QCD cross section.

Diboson The processes with four charged leptons ($\ell\ell\ell\ell$), three charged leptons and one neutrino ($\ell\ell\ell\nu$), and two charged leptons and two neutrinos ($\ell\ell\nu\nu$) are simulated by the SHERPA v2.2.1 generator. Diboson WW , WZ and ZZ processes with four or six electroweak vertices are also used.

Triboson The triboson processes WWW , WWZ , WZZ and ZZZ with up to six charged leptons are simulated by the SHERPA v2.2.1 generator.

ttV The processes ttW , ttZ , $ttWW$ and $ttWZ$ are simulated by MADGRAPH v2.2.2 at the leading-order, with PYTHIA 8.186 for the parton shower model.

Higgs The WH and ZH processes are generated by using PYTHIA 8 generator, and the A14 set of tuned parameters is used together with the NNPDF23LO PDF set. The ttH processes are generated by using MCATNLO generator, interfaced with HERWIGPP. The CT10 PDF tuning is used along with the CTEQ6L1-UE-EE-5 tuning of parton shower.

3.1.2.2 Signal

The signal MC samples simulate the signal process $\tilde{\chi}_1^\pm \tilde{\chi}_2^0 \rightarrow W(\ell\nu)h$. They are generated by the MADGRAPH v2.2.3, calculated at the leading-order matrix elements with up to two extra partons. The PYTHIA version 8.186 and the A14 tune are also used for the modelling of the SUSY decay chain, parton showering and hadronization. Parton distribution functions are provided by the NNPDF23LO PDF set. Table A.12 shows the list of signal samples used in this analysis, with

different hypothesized masses point ($m_{\tilde{\chi}_1^\pm, \tilde{\chi}_2^0}$, $m_{\tilde{\chi}_1^0}$). These signal samples are selected that at least 2 leptons with $p_T > 7$ GeV is required. The efficiencies due to this selection are applied and also shown in the table.

3.2 Pre-selection and event cleaning

The following pre-selections are applied to reject background events which do not come from the proton-proton collision and to ensure that the detector was working properly.

- **Good Run List** The events need to pass the good run list. (For data only)
- **LAr/Tile/SCT error** Events with data integrity errors in the SCT detector and the LAr and Tile calorimeter are removed. (For data only)
- **Primary Vertex** The events are required to have a primary vertex, which is defined as the one with the largest $\sum p_T^2$ of tracks, and has at least two tracks.
- **Cosmic Muon Veto** The events with cosmic muons need to be removed. The track of cosmic muon is identified by large impact parameters with respect to the primary vertex, where $|z_0^{PV}| > 1$ mm or $|d_0^{PV}| > 0.2$ mm.
- **Bad Muon Veto** The events with a bad muon that does not come from the proton-proton collision need to be removed. The bad muon is identified by a large relative error in the ratio of electric charge to momentum (q/p), with the condition that $\sigma(q/p)/|q/p| > 0.2$ [23].
- **Bad Jet Veto** The events with bad jets that do not come from the proton-proton collision need to be removed. A jet with $p_T < 20$ GeV or with the “BadLoose” quality [24] is identified as a bad jet.
- **Trigger Selection** The events are required to pass at least one trigger in the trigger list, described in section 3.3.
- **Exactly 2 baseline leptons** The events which have exactly 2 baseline leptons are selected. The definition of baseline electron and muon are described in section 3.4. “The two leptons” mentioned in the following chapters refer to these 2 baseline leptons. The two leptons are indexed in the descending

order by their p_T . The lepton with larger p_T is called the leading lepton (ℓ_1), and the lepton with smaller p_T is called the sub-leading lepton(ℓ_2).

3.3 Trigger strategy

The time-spacing between two adjacent bunches is 25 ns, and equivalently the frequency is 40 MHz. Because not all the collisions will be our interested events, and it is also infeasible to store all the events generated by the LHC to the permanent storage, the trigger strategy is used. The trigger system accepts and rejects the events immediately after the data is taken. The Level 1 trigger system filters the events from 40 MHz to 100 kHz. The High Level trigger (HLT) system uses the output from the Level 1 trigger system, and further filters the events from 100 kHz to 1 kHz.

In our analysis, the single lepton triggers and di-lepton triggers were used. Table 3.1 and 3.2 show the list of triggers used in this analysis. All triggers are high level trigger (HLT), with the name starting from HLT. The second label represents the p_T selection for the lepton. For example, e24 is the selection that the p_T of the electron is larger than 24 GeV. Other labels are described in appendix B [3,4].

	Single electron	Single muon
2015	HLT_e24_lhmedium_L1EM20VH HLT_e60_lhmedium HLT_e120_lhloose	HLT_mu20_iloose_L1MU15 HLT_mu40
2016	HLT_e26_lhtight_nod0_ivarloose HLT_e60_lhmedium_nod0 HLT_e140_lhloose_nod0	HLT_mu26_imedium HLT_mu50

Table 3.1: List of the single lepton triggers used in this analysis.

	Di-electron	Di-muon	Electron-muon
2015	HLT_2e12_lhloose_L12EM10VH	HLT_mu18_mu8noL1	HLT_e17_lhloose_mu14 HLT_e7_lhmedium_mu24
2016	HLT_2e17_lhvloose_nod0	HLT_mu22_mu8noL1	HLT_e17_lhloose_nod0_mu14 HLT_e7_lhmedium_nod0_mu24

Table 3.2: List of the di-lepton triggers used in this analysis.

3.4 Object definitions

3.4.1 Electrons

Electrons are reconstructed inside the region $|\eta^{\text{cluster}}| < 2.47$ [25]. The baseline electrons are identified by the `LooseAndBLayer` quality criterion and have $p_T > 10$ GeV. The signal electrons must be baseline electrons and satisfy additional criteria. At the signal level, the electron must satisfy the `Medium` quality criterion and has $p_T > 25$ GeV. The working point for the isolation cut is Fix (Tight) described in [25]. The requirement for the impact parameter is $|z_0 \cdot \sin(\theta)| < 0.5$ mm and $|d_0/\sigma(d_0)| < 5$. To reduce the charge flip background, the working point `Medium` at 97% efficiency is used. The selections for baseline and signal electrons are summarised in table 3.3.

3.4.2 Muons

Muons are reconstructed in $|\eta| < 2.4$ [23]. The baseline muons are identified by the `Medium` quality criterion and have $p_T > 10$ GeV. The signal muons must be baseline muons and satisfy additional criteria. The additional criteria are $p_T > 25$ GeV and isolation cut with the working point `GradientLoose` described in [23]. The requirement for the impact parameter is $|z_0 \cdot \sin(\theta)| < 0.5$ mm and $|d_0/\sigma(d_0)| < 3$. The selections for baseline and signal muons are summarised in table 3.3.

3.4.3 Jets

The baseline jets are reconstructed by the anti- k_t jet algorithm [26] with the distance parameter $D = 0.4$. Each baseline jet must have $p_T > 20$ GeV and $|\eta| < 2.8$. The signal jets are selected on top of the baseline jet, with additional

	Baseline Electron	Baseline Muon
Acceptance	$p_T > 10 \text{ GeV}$, $ \eta^{\text{cluster}} < 2.47$	$p_T > 10 \text{ GeV}$, $ \eta < 2.4$
Quality	LooseAndBLayerLLH	Medium
	Signal Electron	Signal Muon
Acceptance	$p_T > 25 \text{ GeV}$	$p_T > 25 \text{ GeV}$
Quality	MediumLLH	Medium
Isolation Cut	FixedCutTight	GradientLoose
Impact parameter	$ z_0 \cdot \sin(\theta) < 0.5 \text{ mm}$ $ d_0/\sigma(d_0) < 5$	$ z_0 \cdot \sin(\theta) < 0.5 \text{ mm}$ $ d_0/\sigma(d_0) < 3$
ChargeIDSelector	Medium at 97% efficiency	-

Table 3.3: Summary of the electron and muon selection criteria. The signal selection requirements are applied on top of the baseline criteria.

criteria. The signal jets need to further satisfy the Jet Vertex Tagger (JVT) cut [27] that $\text{JVT} > 0.59$ if the jets have $p_T < 60 \text{ GeV}$ and $|\eta| < 2.4$. The b-jets are signal jets with b-tag, by using the MV2c10 b-tagging algorithm with **FixedCut** working point which has b-jet efficiency 77% [28]. The selections of jets are summarised in table 3.4.

3.4.4 Missing transverse momentum

Based on the conservation of transverse momentum, the total transverse momentum of the missing particles, which were not detected by the detector, can be estimated by the total transverse momentum of particles which can be detected. The missing transverse momentum ($\mathbf{p}_T^{\text{miss}}$) is defined by the negative of the sum of transverse momentum of all electrons, muons, photons, jets and all other tracks associated with the primary vertex. The calibrated electrons, muons, photons and jet objects are used as the inputs. This missing transverse momentum can estimate the total transverse momentum of the missing neutrinos and hypothetical neutralinos. The Missing transverse energy (E_T^{miss}) is defined by the magnitude of the missing transverse momentum $\mathbf{p}_T^{\text{miss}}$.

Baseline Jet	
Collection	AntiKt4EMTopo
Acceptance	$p_T > 20 \text{ GeV}$, $ \eta < 2.8$
Signal Jet	
Acceptance	$p_T > 20 \text{ GeV}$, $ \eta < 2.8$
Jet vertex tagger	Medium working point $\text{JVT} > 0.59$ for $p_T < 60 \text{ GeV}$ and $ \eta < 2.4$
B-Jet	
Acceptance	$p_T > 20 \text{ GeV}$, $ \eta < 2.4$
b -tagging algorithm	MV2c10 algorithm
Working point	FixedCut with efficiency 77%

Table 3.4: Summary of the jet selection criteria.

3.4.5 Overlap removal

The overlap removal (OR) is performed with the baseline objects (electrons, muons and jets). The objects are removed in the following order.

1. If a jet is within $\Delta R = \sqrt{(\Delta\eta)^2 + (\Delta\phi)^2} = 0.2$ of an electron:
 - If the jet is not b -tagged, then the jet is removed. It mostly originates from the calorimeter energy deposits by the electron shower.
 - If the jet is b -tagged, then the electron is removed. It is more likely that it results from the semi-leptonic decays of b -quarks.
2. Electrons within $\Delta R = 0.4$ of a jet are removed, in order to suppress electrons from semi-leptonic decays of c - and b -hadrons.
3. Muons within $\Delta R = 0.4$ of a jet are removed, in order to suppress muons from semi-leptonic decays of c - and b -hadrons.
4. Any muons sharing the same inner-detector track with an electron are removed.
5. Any electrons sharing the same inner-detector track with the remaining muons are removed.

Chapter 4

Signal regions

A signal region (SR) is the region in which signals are rich and the background are small. It is designed to search for the new particles. In the analysis, two signal regions are defined, SRjet1 and SRjet23. Number of signal jets in SRjet1 is 1, while number of signal jets in SRjet23 is 2 or 3. The details of the definition of these two signal regions will be described in section 4.2.

4.1 Discriminant variables

The discriminant variables are designed to define the signal regions. The discriminant variables are used to distinguish the signal events from the background events, by applying a cut on the discriminant variable. The following are the discriminant variables used in this analysis.

- n_{jets} : Number of signal jets:
- $n_{b\text{-jets}}$: Number of b -jets.
- p_T^1 : Transverse momentum of the leading lepton.
- p_T^2 : Transverse momentum of the sub-leading lepton.
- $\Delta\eta_{ll}$: The difference in pseudorapidity between the two leptons.

$$\Delta\eta_{ll} = |\eta_1 - \eta_2| \quad (4.1)$$

- m_{ll} : The invariant mass of the two leptons (i.e. the invariant mass of the 4-momentum sum of the two leptons).

$$(m_{ll})^2 = (p_1 + p_2)^2 \quad (4.2)$$

- E_T^{miss} : The magnitude of the missing transverse momentum.

$$E_T^{\text{miss}} = |\mathbf{p}_T^{\text{miss}}| \quad (4.3)$$

- m_T : It is designed to reconstruct the transverse mass of the W-boson. It is calculated by using the transverse momentum of the leading lepton and the missing transverse momentum, defined by equation 4.4. By using the approximation $|\mathbf{p}_T^1| > 10 \text{ GeV} \gg m_1$ (0.511 MeV or 106 MeV) and hence $E_T^1 = \sqrt{(m_1)^2 + |\mathbf{p}_T^1|^2} \approx |\mathbf{p}_T^1|$, it can be approximated by $m_T = \sqrt{2p_T^1 E_T^{\text{miss}}(1 - \cos \Delta\phi)}$, where $\Delta\phi$ is the azimuthal angle between the leading lepton and the missing transverse momentum.

$$(m_T)^2 = (E_T^1 + E_T^{\text{miss}})^2 - |\mathbf{p}_T^1 + \mathbf{p}_T^{\text{miss}}|^2 \quad (4.4)$$

$$\approx (|\mathbf{p}_T^1| + |\mathbf{p}_T^{\text{miss}}|)^2 - |\mathbf{p}_T^1 + \mathbf{p}_T^{\text{miss}}|^2 \quad (4.5)$$

$$= (p_T^1 + p_T^{\text{miss}})^2 - (\mathbf{p}_T^1 + \mathbf{p}_T^{\text{miss}}) \cdot (\mathbf{p}_T^1 + \mathbf{p}_T^{\text{miss}}) \quad (4.6)$$

$$= (p_T^1)^2 + (p_T^{\text{miss}})^2 + 2p_T^1 p_T^{\text{miss}} - (p_T^1)^2 - (p_T^{\text{miss}})^2 - 2\mathbf{p}_T^1 \cdot \mathbf{p}_T^{\text{miss}} \quad (4.7)$$

$$= 2p_T^1 p_T^{\text{miss}} - 2\mathbf{p}_T^1 \cdot \mathbf{p}_T^{\text{miss}} \quad (4.8)$$

$$= 2p_T^1 p_T^{\text{miss}} - 2p_T^1 p_T^{\text{miss}} \cos \Delta\phi \quad (4.9)$$

$$= 2p_T^1 p_T^{\text{miss}}(1 - \cos \Delta\phi) \quad (4.10)$$

$$m_T = \sqrt{2p_T^1 E_T^{\text{miss}}(1 - \cos \Delta\phi)} \quad (4.11)$$

- m_{eff} : Effective mass is defined as the sum of the transverse momenta of the two leptons, signal jets and the missing transverse energy.

$$m_{\text{eff}} = p_T^1 + p_T^2 + E_T^{\text{miss}} + \sum_{\text{signal jets}} p_T \quad (4.12)$$

- m_{lj} or m_{ljj} : m_{lj} is for the case that $n_{\text{jets}} = 1$ (i.e. SRjet1), while m_{ljj} is for the case that $n_{\text{jets}} = 2$ or 3 (i.e. SRjet23). It attempts to reconstruct the mass of the Higgs boson. It is defined as the invariant mass of the leading jet (i.e. the jet with the highest p_T) in SRjet1 or the di-jet system (i.e. the sum of the two leading jets) in SRjet23, and the closest lepton to the jet system, where the measure of distance is $\Delta R = \sqrt{(\Delta\phi)^2 + (\Delta\eta)^2}$. The details of the definition are shown below.

The 4-momentum of the jet system is defined as

$$p_{\text{jet-system}} = \begin{cases} p_{\text{jet1}} & \text{for SRjet1} \\ p_{\text{jet1}} + p_{\text{jet2}} & \text{for SRjet23} \end{cases} \quad (4.13)$$

The 4-momentum of the closest lepton is defined as

$$p_{\text{closest-lepton}} = \begin{cases} p_{\text{lepton1}} & \text{if } \Delta R(p_{\text{lepton1}}, p_{\text{jet-system}}) \leq \Delta R(p_{\text{lepton2}}, p_{\text{jet-system}}) \\ p_{\text{lepton2}} & \text{if } \Delta R(p_{\text{lepton1}}, p_{\text{jet-system}}) > \Delta R(p_{\text{lepton2}}, p_{\text{jet-system}}) \end{cases} \quad (4.14)$$

m_{lj} or m_{ljj} is defined as the invariant mass of the 4-momentum sum of the closest lepton and the jet system.

$$(m_{lj(j)})^2 = (p_{\text{closest-lepton}} + p_{\text{jet-system}})^2 \quad (4.15)$$

- m_{T2} : The “stransverse mass” (m_{T2}) is designed to set a lower bound on the masses of the unseen pair of charginos $\tilde{\chi}_1^\pm$ and neutralinos $\tilde{\chi}_2^0$. One branch is charginos $\tilde{\chi}_1^\pm$ decay and another branch is neutralinos $\tilde{\chi}_2^0$ decay, as shown in figure 1.6. They are both assumed to decay into one lepton that can be detected, and into neutralinos $\tilde{\chi}_1^0$ and neutrino that cannot be detected. Therefore, the missing transverse momentum is expected. The calculation of m_{T2} uses the transverse momentum of the two leptons (i.e. \mathbf{p}_T^1 and \mathbf{p}_T^2) and the missing transverse momentum $\mathbf{p}_T^{\text{miss}}$. It is defined by finding the minimum value over all possible transverse vectors \mathbf{q}_T , which is the trial missing transverse momentum on one side [29].

$$m_{T2} = \min_{\mathbf{q}_T} \left[\max \left(m_T(\mathbf{p}_T^1, \mathbf{q}_T), m_T(\mathbf{p}_T^2, \mathbf{p}_T^{\text{miss}} - \mathbf{q}_T) \right) \right] \quad (4.16)$$

Similar to equation 4.11, the transverse mass of two transverse momenta $m_T(\mathbf{p}_T, \mathbf{q}_T)$ is defined as follows.

$$m_T(\mathbf{p}_T, \mathbf{q}_T) = \sqrt{2p_T q_T (1 - \cos \Delta\phi)} \quad (4.17)$$

where $\Delta\phi$ is the azimuthal angle between the two transverse momenta.

4.2 Signal region optimization

This section describes how the signal region definition is optimized. The goal of the optimization is to increase the sensitivity to signals. This study was done by using the MC samples. The signal significance Z for large N_s and N_b is defined by

$$Z = \frac{N_s}{\sqrt{N_b + N_s}} \quad (4.18)$$

It measures how well the signal region is defined. The signal region optimization is driven by increasing the signal significance Z . The signal significance can be interpreted as the variable $z = \frac{x-\mu}{\sigma}$ in the standard normal distribution. The corresponding p-value can be interpreted as the probability that the excess in the number of signal events from the background prediction is just due to the statistical fluctuation. By changing the cuts on different discriminant variables, the maximum signal significance can be obtained, and the corresponding optimal cuts are the definition of the signal region.

Equation 4.18 is only valid for large N_s and N_b . Because N_s and N_b are often small, another sophisticated formula for the signal significance is used. Also, the systematic error and statistical error of N_b need to be taken into account. A fixed systematic error 25% is assumed, and the total relative error σ_b is the sum of systematic and statistical error in quadrature.

$$\sigma_b = \sqrt{(25\%)^2 + \left(\frac{\Delta N_b}{N_b}\right)^2} \quad (4.19)$$

where ΔN_b is the statistical error of N_b . The signal significance is calculated by using the function `NumberCountingUtils::BinomialExpZ` provided in `RooStats`.

$$Z = \text{BinomialExpZ}(N_s, N_b, \sigma_b) \quad (4.20)$$

This method basically calculates the signal significance Z with the corresponding p-value and probability for the following case. A series of Bernoulli experiments is conducted with the number of trials $n = N_b + N_s + \frac{1}{\sigma_b^2}$ and the probability of success of each trial $p = 1/(1 + 1/(N_b\sigma_b^2))$ [30]. The corresponding p-value is the probability that the number of success is at least $N_b + N_s$. The signal significance Z calculated by the equation 4.20 is an approximated signal significance to our analysis. It is useful because it has the following properties.

- It is a continuous function. N_b and N_s can be non-integer. (cf. Poisson distribution)
- It is a smooth function. It is convenient for finding the maximum value.
- For large N_b and N_s , it reduces to equation 4.18.
- It is fast to compute.

By using the equation 4.20, an approximately optimal signal region can be found.

4.2.1 Pre-selections

Before the optimization, the following pre-selections are applied, on top of the selections in section 3.2.

- **Exactly 2 signal leptons** The events which have exactly 2 signal leptons are selected.
- **Same sign** The electric charges of the two leptons have the same sign.
- **B-jet veto** The number of b-jets is 0, to suppress the top background.
- **Number of jet** Two signal regions are defined according to the number of signal jets. One signal region has 1 signal jet, called “SRjet1”, and another has 2 or 3 signal jets, called “SRjet23”.

4.2.2 Samples

As mentioned above, MC samples are used for estimating the expected N_s and N_b in the process of optimization.

For the signal, the mass point $(m_{\tilde{\chi}_1^\pm, \tilde{\chi}_2^0}, m_{\tilde{\chi}_1^0}) = (225, 75)$ is used for SRjet1, while the mass point $(m_{\tilde{\chi}_1^\pm, \tilde{\chi}_2^0}, m_{\tilde{\chi}_1^0}) = (187.5, 37.5)$ is used for SRjet23.

For the background, MC samples are used for diboson (WZ, WW and ZZ), ttV and rare processes (triboson, multi-top and Higgs). Instead of using the corresponding MC samples, the fake lepton background is estimated by the matrix method as described in section 5.2, because the fake lepton background is the dominant background and the corresponding MC sample is not reliable. The charge flip background estimated in section 5.1 is also used. The distributions after the pre-selections in section 4.2.1, but before the optimization, are shown in figures 4.1 and 4.2.

4.2.3 Optimization

Some constraints are applied during the process of optimization, in order to have enough statistics to have reliable estimation of N_s and N_b .

- The yields (i.e. the sum of weighted events) for each process of background need to be positive, to have a reasonable and stable modelling of the background shape. Also, the HistFitter requires the background to have positive yields.

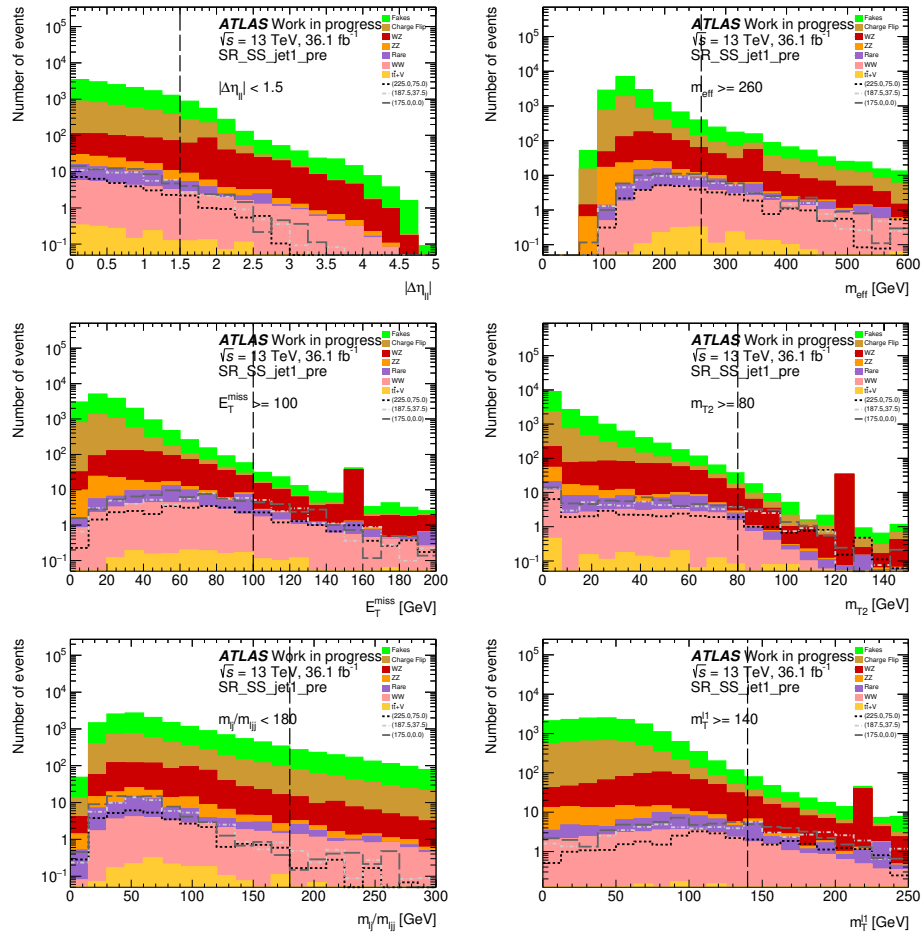


Figure 4.1: Distributions of the kinematic variables used for the optimization in SRjet1. The pre-selections have been applied.

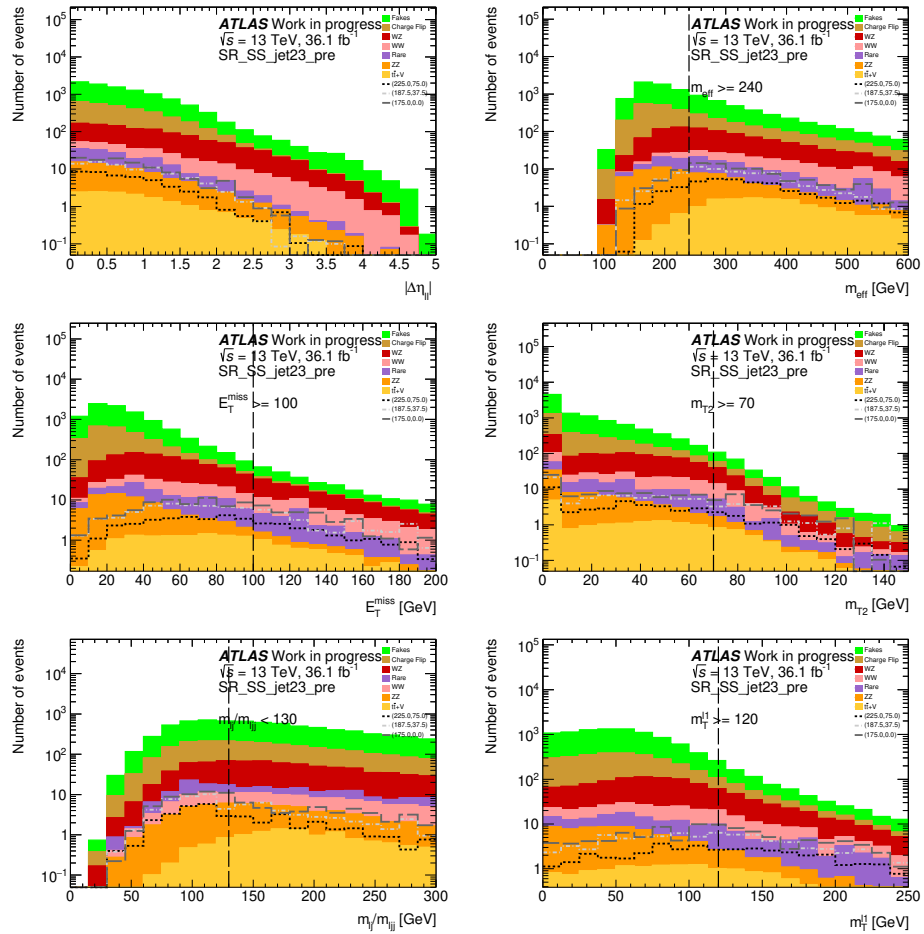


Figure 4.2: Distributions of the kinematic variables used for the optimization in SRjet23. The pre-selections have been applied.

- The diboson and ttV background have at least 10 unweighted events respectively, to have a reliable estimation for the main background processes from prompt leptons (i.e. not fake leptons).
- For E_T^{miss} , m_T , m_{eff} and m_{T2} , only lower cuts are applied.
- For $\Delta\eta_{ll}$ and $m_{lj(j)}$, only upper cuts are applied.

The list of variables used is shown in the table 4.1.

Variable	Optimization direction
$\Delta\eta_{ll}$	Cut value reduced
E_T^{miss}	Cut value increased
m_T	Cut value increased
m_{eff}	Cut value increased
$m_{lj(j)}$	Cut value reduced
m_{T2}	Cut value increased

Table 4.1: Kinematic variables used in the optimization.

4.2.4 Results of optimization

The final results for the definitions of the two signal regions are shown in table 4.2. The yields for different background and signal processes are shown in table 4.3 and 4.4. The N-1 plots for the discriminant variables are shown in figures 4.3 and 4.4. The N-1 plot means that all other SR selections are applied, except the selection for that variable.

Variable	SRjet1	SRjet23
$\Delta\eta_{ll}$	≤ 1.5	–
E_T^{miss}	$\geq 100 \text{ GeV}$	$\geq 100 \text{ GeV}$
m_T	$\geq 140 \text{ GeV}$	$\geq 120 \text{ GeV}$
m_{eff}	$\geq 260 \text{ GeV}$	$\geq 240 \text{ GeV}$
$m_{lj(j)}$	$< 180 \text{ GeV}$	$< 130 \text{ GeV}$
m_{T2}	$\geq 80 \text{ GeV}$	$\geq 70 \text{ GeV}$

Table 4.2: Final SR definitions

The expected combined signal significances for different mass points are shown in figure 4.5, where 25% systematic uncertainty is assumed. The combined signal

	Number of events	Significance
Fakes	3.295 ± 0.819 (24)	
WZ	2.176 ± 0.398 (257)	
Charge Flip	0.472 ± 0.053 (265)	
Rare	0.444 ± 0.111 (56)	
WW	0.166 ± 0.023 (67)	
$t\bar{t} + V$	0.125 ± 0.046 (36)	
ZZ	0.055 ± 0.028 (31)	
Total BG	6.733 ± 0.921 (736)	
(225.0,75.0)	3.33 ± 0.60 (60)	0.74
(187.5,37.5)	3.77 ± 0.95 (31)	0.86
(175.0,0.0)	4.29 ± 0.73 (36)	0.98

Table 4.3: The yields in SRjet1. The unweighed event are also shown in parentheses.

	Number of events	Significance
WZ	1.849 ± 0.273 (319)	
Fakes	1.765 ± 0.709 (20)	
Rare	0.731 ± 0.195 (48)	
WW	0.514 ± 0.037 (235)	
Charge Flip	0.267 ± 0.029 (274)	
$t\bar{t} + V$	0.142 ± 0.031 (67)	
ZZ	0.067 ± 0.025 (24)	
Total BG	5.335 ± 0.787 (987)	
(225.0,75.0)	2.35 ± 0.34 (58)	0.57
(187.5,37.5)	4.72 ± 0.74 (47)	1.26
(175.0,0.0)	8.60 ± 1.51 (58)	2.24

Table 4.4: The yields in SRjet23. The unweighed event are also shown in parentheses.

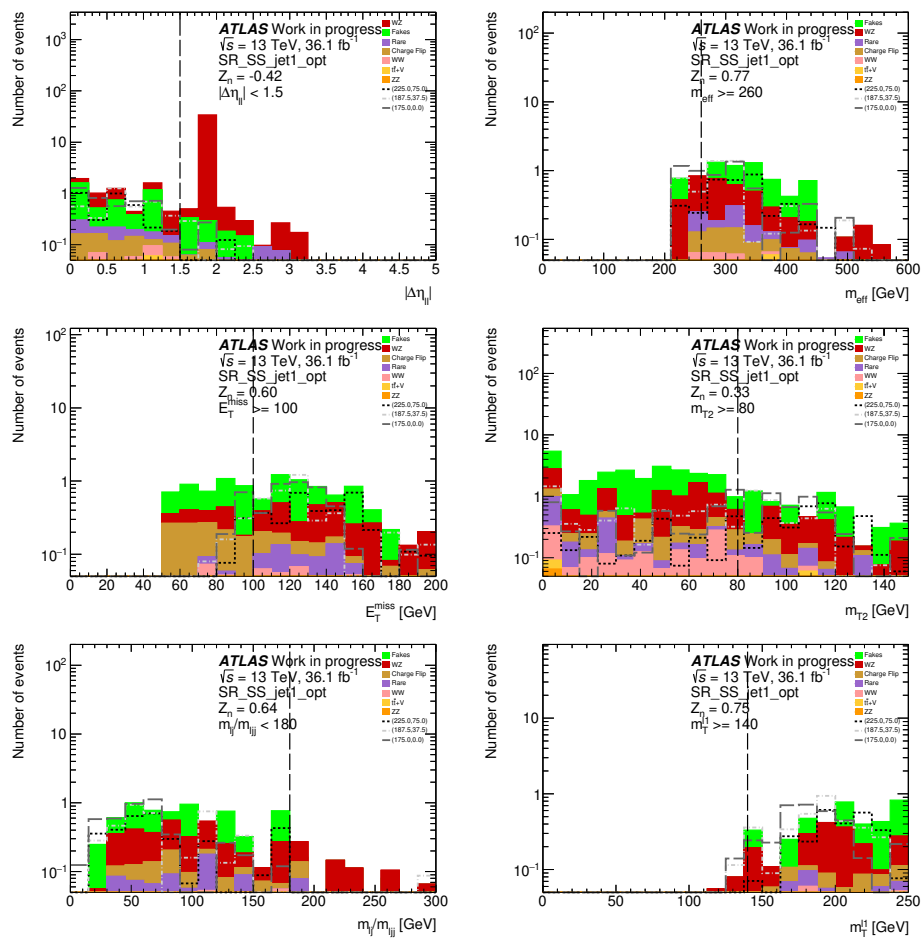


Figure 4.3: The N-1 plots for SRjet1.

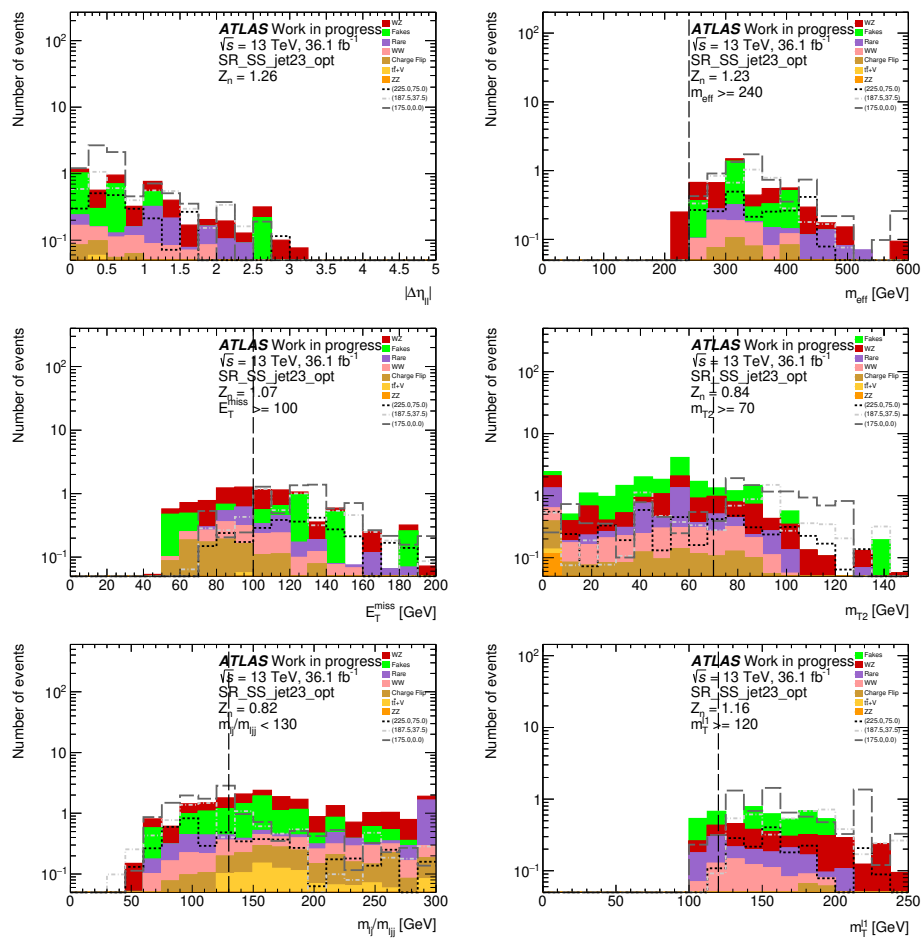


Figure 4.4: The N-1 plots for SRjet23.

significances are calculated by adding the signal significances of the two signal regions in quadrature. The figure shows considerable signal significances, in particular for the compressed region, where $m_{\tilde{\chi}_1^\pm, \tilde{\chi}_2^0} - m_{\tilde{\chi}_1^0}$ are close to the mass of Higgs boson (~ 125 GeV).

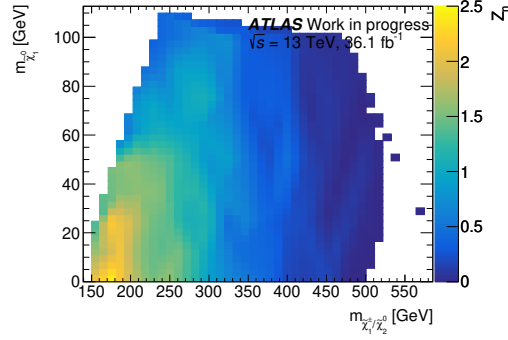


Figure 4.5: The expected combined signal significances for different mass points.

Chapter 5

Background estimation

The charge flip background and the fake lepton background are the two dominant backgrounds due to a mis-reconstruction of the final state leptons. This type of background will be estimated by using data-driven methods.

5.1 Charge flip background

5.1.1 Sources for charge flip background

The charge flip background is due to the misidentification of the sign of the charge of a lepton. The sign of the charge is determined by the direction of the curvature of the track. There are two main sources for the misidentification for the direction of the curvature.

The first source is described by figure 5.1. It is the case that the lepton interacts with the material of the detector and a photon is emitted by the process of bremsstrahlung. The emitted photon further produces a pair of electron and positron, namely the γ conversion. As shown in figure 5.1, if most of the energy is carried by the positron e^+ (the purple track), the direction of the curvature of the reconstructed track (the orange track) will be reversed. Thus, the charge of the lepton is flipped. Because the misidentification depends on the amount of the detector material, and hence depends on $|\eta|$ of the original track.

The second source is described by the figure 5.2. When the p_T of the lepton is very high, the track of the lepton will be almost a straight line. The curvature of the track will be close to zero, and the sign of the curvature will be difficult to be determined. As a result, the sign of the charge of the lepton is likely incorrectly

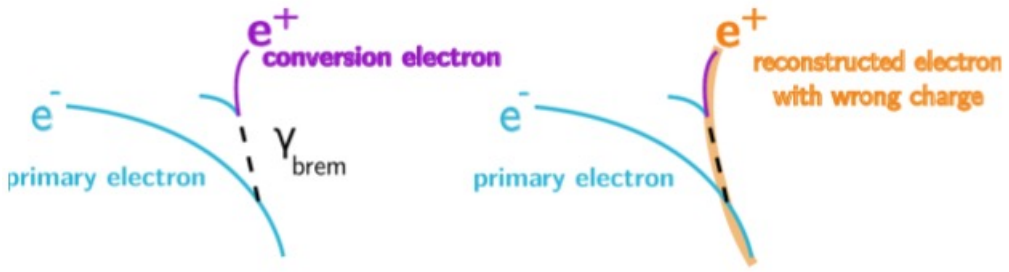


Figure 5.1: It shows how the track of the electron is incorrectly reconstructed (the orange track), due to the process of bremsstrahlung and γ conversion.

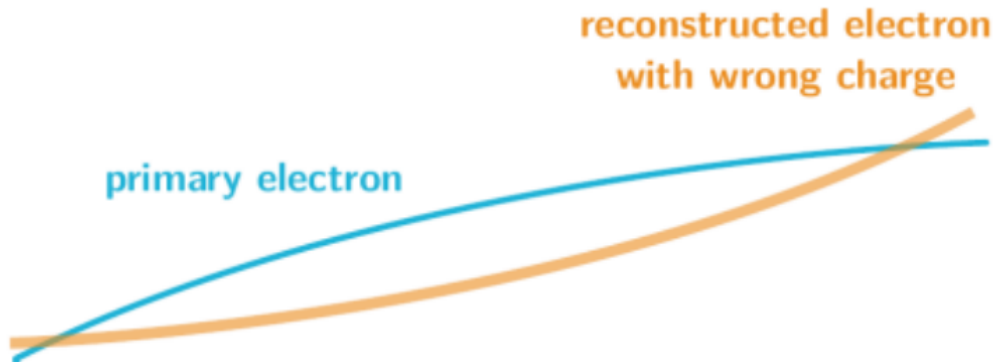


Figure 5.2: It shows how the track of the electron is incorrectly reconstructed (the orange track), due to very high p_T of the electron.

assigned. The chance to have this problem obviously depends on p_T of the lepton.

Compared to an electron, the charge of a reconstructed muon will be less often to be misidentified. Firstly, a muon is heavier than an electron. This will reduce the chance of the process of bremsstrahlung. Secondly, muons can reach to the muon spectrometer, which is the outer part of the detector, while electrons cannot. This means that the length of the track of a muon, which can be detected by the tracker, is longer than that of an electron. Hence, the reconstructed curvature of the track for muons can be more accurate, and it reduces the chance of the misidentification due to the high p_T . Because most of the charge flip background comes from electrons, we only estimate the charge flip background for electrons.

5.1.2 Likelihood method

The probability that the charge of an electron is flipped is denoted by the charge-flip rate ϵ_i , where the index i represents the dependency on the p_T and $|\eta|$ of the electron. The value of index i is found by splitting the variables p_T and $|\eta|$ into different 2-dimensional bins, and the binning for the p_T and $|\eta|$ is described by the table 5.1. The index i of ϵ_i is defined by the index of the bin.

Variable	Boundary of the bins
p_T (GeV)	25, 60, 90, 130, 150, 1000
$ \eta $	0, 0.50, 1.00, 1.37, 1.52, 1.80, 2.00, 2.47

Table 5.1: Binning in p_T and $|\eta|$ for the charge-flip rate ϵ_i .

Suppose that there are m_{OS}^{ij} opposite-sign events with the leading lepton in bin i and the sub-leading lepton in bin j before the reconstruction, and there are m_{SS}^{ij} same-sign events. After the reconstruction, there are M_{OS}^{ij} opposite-sign events and M_{SS}^{ij} same-sign events due to the charge-flipped leptons. The number of events after the reconstruction is given by

$$M_{OS}^{ij} = (1 - \epsilon_i)(1 - \epsilon_j)m_{OS}^{ij} + \epsilon_i(1 - \epsilon_j)m_{SS}^{ij} + (1 - \epsilon_i)\epsilon_j m_{SS}^{ij} + \epsilon_i\epsilon_j m_{OS}^{ij} \quad (5.1)$$

$$M_{SS}^{ij} = (1 - \epsilon_i)(1 - \epsilon_j)m_{SS}^{ij} + \epsilon_i(1 - \epsilon_j)m_{OS}^{ij} + (1 - \epsilon_i)\epsilon_j m_{OS}^{ij} + \epsilon_i\epsilon_j m_{SS}^{ij} \quad (5.2)$$

From equation 5.2, the number of reconstructed same-sign events due to the charge-flipped leptons, i.e. the charge flip BG , denoted by N_{SS}^{ij} , is

$$N_{SS}^{ij} = \epsilon_i(1 - \epsilon_j)m_{OS}^{ij} + (1 - \epsilon_i)\epsilon_j m_{OS}^{ij} + \epsilon_i\epsilon_j m_{SS}^{ij} \quad (5.3)$$

$$\approx \epsilon_i(1 - \epsilon_j)m_{OS}^{ij} + (1 - \epsilon_i)\epsilon_j m_{OS}^{ij} \quad (5.4)$$

The dominant charge flip BG comes from events with two opposite-sign electrons, with one of the charge is flipped. The contribution from the events with two charge-flipped electrons is negligible.

Figure 5.3 shows that the number of OS events is much larger than the number of SS events by almost 10^3 times, and hence m_{OS}^{ij} is much larger than m_{SS}^{ij} . Besides, it turns out that the measured charge-flip rate ϵ_i is about 10^{-3} , as shown

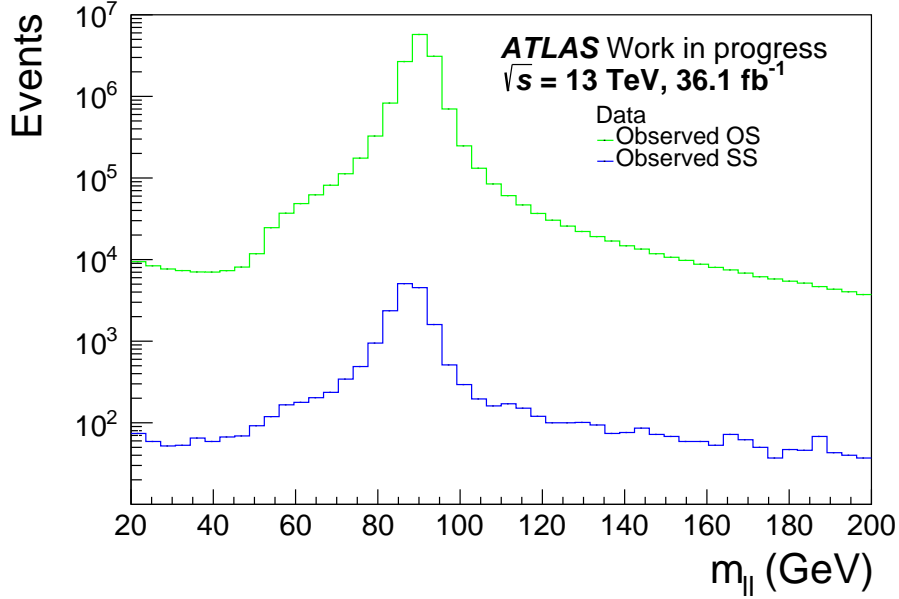


Figure 5.3: The comparison between the OS events and the SS events in data. The number of OS events is much larger than the number of SS events by almost 10^3 times.

in figure 5.8. Hence, m_{OS}^{ij} can be estimated by

$$M_{OS}^{ij} \approx (1 - \epsilon_i)(1 - \epsilon_j)m_{OS}^{ij} \quad (5.5)$$

$$m_{OS}^{ij} \approx \frac{M_{OS}^{ij}}{(1 - \epsilon_i)(1 - \epsilon_j)} \quad (5.6)$$

$$m_{OS}^{ij} \approx M_{OS}^{ij} \quad (5.7)$$

$$m_{OS}^{ij} \approx M_{OS}^{ij} + M_{SS}^{ij} \quad (5.8)$$

By substituting equation 5.8 into 5.4, the charge flip BG can be estimated by M_{OS}^{ij} , M_{SS}^{ij} and the charge-flip rate ϵ_i ,

$$N_{SS}^{ij} \approx \epsilon_i(1 - \epsilon_j)m_{OS}^{ij} + (1 - \epsilon_i)\epsilon_jm_{OS}^{ij} \quad (5.9)$$

$$= [\epsilon_i(1 - \epsilon_j) + (1 - \epsilon_i)\epsilon_j]m_{OS}^{ij} \quad (5.10)$$

$$\approx p_{ij}(M_{OS}^{ij} + M_{SS}^{ij}) \quad (5.11)$$

$$= p_{ij}N^{ij} \quad (5.12)$$

where p_{ij} and N^{ij} are

$$p_{ij} = \epsilon_i(1 - \epsilon_j) + (1 - \epsilon_i)\epsilon_j \quad (5.13)$$

$$N^{ij} = M_{OS}^{ij} + M_{SS}^{ij}$$

The probability density function of N_{SS}^{ij} , with the given values of N^{ij} and ϵ_i , can be described by the Poisson distribution with the mean value $\lambda = p_{ij}N^{ij}$.

$$P(N_{SS}^{ij}|N^{ij}, \epsilon_i, \epsilon_j) = \frac{\lambda^{N_{SS}^{ij}} e^{-\lambda}}{N_{SS}^{ij}!} \quad (5.14)$$

$$= \frac{(p_{ij}N^{ij})^{N_{SS}^{ij}} e^{-p_{ij}N^{ij}}}{N_{SS}^{ij}!} \quad (5.15)$$

In order to estimate the charge flip BG, we need to measure the charge-flip rate ϵ_i . The charge-flip rate is measured as a function of p_T and $|\eta|$ by using a likelihood method, based on the 2015 and 2016 data. A control region is used to select $Z \rightarrow ee$ processes, with Z mass window of $80 \text{ GeV} < m_{ll} < 100 \text{ GeV}$. Inside the control region, exactly 2 signal electrons are required. In this control region, the total number of events N^{ij} and the SS events N_{SS}^{ij} in each bin can be measured. By using the equation 5.15, the charge-flip rate ϵ_i can be measured by using the following likelihood method.

The likelihood function L is defined by

$$L(\epsilon_i, \epsilon_j | N^{ij}, N_{SS}^{ij}) = \prod_{ij} P(N_{SS}^{ij} | N^{ij}, \epsilon_i, \epsilon_j) \quad (5.16)$$

$$= \prod_{ij} \frac{(p_{ij}N^{ij})^{N_{SS}^{ij}} e^{-p_{ij}N^{ij}}}{N_{SS}^{ij}!} \quad (5.17)$$

Given the measured values of N^{ij} and N_{SS}^{ij} in each bin, the value of ϵ_i can be estimated by maximizing the likelihood function over all possible values of ϵ_i . By taking the negative logarithm, it is equivalent to minimize $-\ln L$.

$$-\ln L = -\ln \prod_{ij} \frac{(p_{ij}N^{ij})^{N_{SS}^{ij}} e^{-p_{ij}N^{ij}}}{N_{SS}^{ij}!} \quad (5.18)$$

$$= -\sum_{ij} \ln \frac{(p_{ij}N^{ij})^{N_{SS}^{ij}} e^{-p_{ij}N^{ij}}}{N_{SS}^{ij}!} \quad (5.19)$$

$$= -\sum_{ij} \left[N_{SS}^{ij} \ln(p_{ij}N^{ij}) - p_{ij}N^{ij} - \ln(N_{SS}^{ij}!) \right] \quad (5.20)$$

$$= -\sum_{ij} \left[N_{SS}^{ij} \ln(p_{ij}N^{ij}) - p_{ij}N^{ij} \right] + \text{constant} \quad (5.21)$$

$$= -\sum_{ij} \left[N_{SS}^{ij} \ln(N^{ij}[\epsilon_i(1-\epsilon_j) + (1-\epsilon_i)\epsilon_j]) - N^{ij}[\epsilon_i(1-\epsilon_j) + (1-\epsilon_i)\epsilon_j] \right] + \text{constant} \quad (5.22)$$

5.1.3 Background subtraction

By minimizing $-\ln L$ described in the previous section, the value of the charge-flip rate ϵ_i can be measured by using the data in the control region. In order to have accurate N^{ij} and N_{SS}^{ij} , the number of events should come from $Z \rightarrow ee$ processes, and other processes should be subtracted in data. The number of events from other processes can be estimated with the sideband method in the region: $60 \text{ GeV} < m_{ll} < 80 \text{ GeV}$ and $100 \text{ GeV} < m_{ll} < 120 \text{ GeV}$, by assuming a flat distribution. The corrected values of N^{ij} and N_{SS}^{ij} are given by

$$N_{80,100;\text{corrected}} = N_{80,100} - 20 \left(\frac{N_{60,80} + N_{80,100}}{20 + 20} \right) \quad (5.23)$$

In the sideband subtraction, the number of events in the sideband region should be normalized to the width of the central region. In general, given the number of events in the central region N_{central} , the left sideband region N_{left} and the right sideband region N_{right} , and their corresponding width w_{central} , w_{left} and w_{right} , the corrected values $N_{\text{central},\text{corrected}}$ are given by

$$N_{\text{central},\text{corrected}} = N_{\text{central}} - w_{\text{central}} \left(\frac{N_{\text{left}} + N_{\text{right}}}{w_{\text{left}} + w_{\text{right}}} \right) \quad (5.24)$$

5.1.4 Results without systematic uncertainty

Figure 5.4 shows the measured values of the charge-flip rate ϵ_i by using the data. The errors only include the uncertainties in the likelihood method due to the statistics, denoted by $\epsilon_{\text{lik,data}}$.

5.1.5 Systematic uncertainties due to background subtraction

The systematic uncertainties due to background subtraction is estimated by the variations of different central widths and sideband widths. The following are the nominal central region and sideband region, and their 4 variations.

The nominal background subtraction:

- Central region: 80 - 100 GeV; Sideband width: 20 GeV

The 4 variations for background subtraction:

- Central region: 80 - 100 GeV; Sideband width: 15 GeV
- Central region: 80 - 100 GeV; Sideband width: 25 GeV

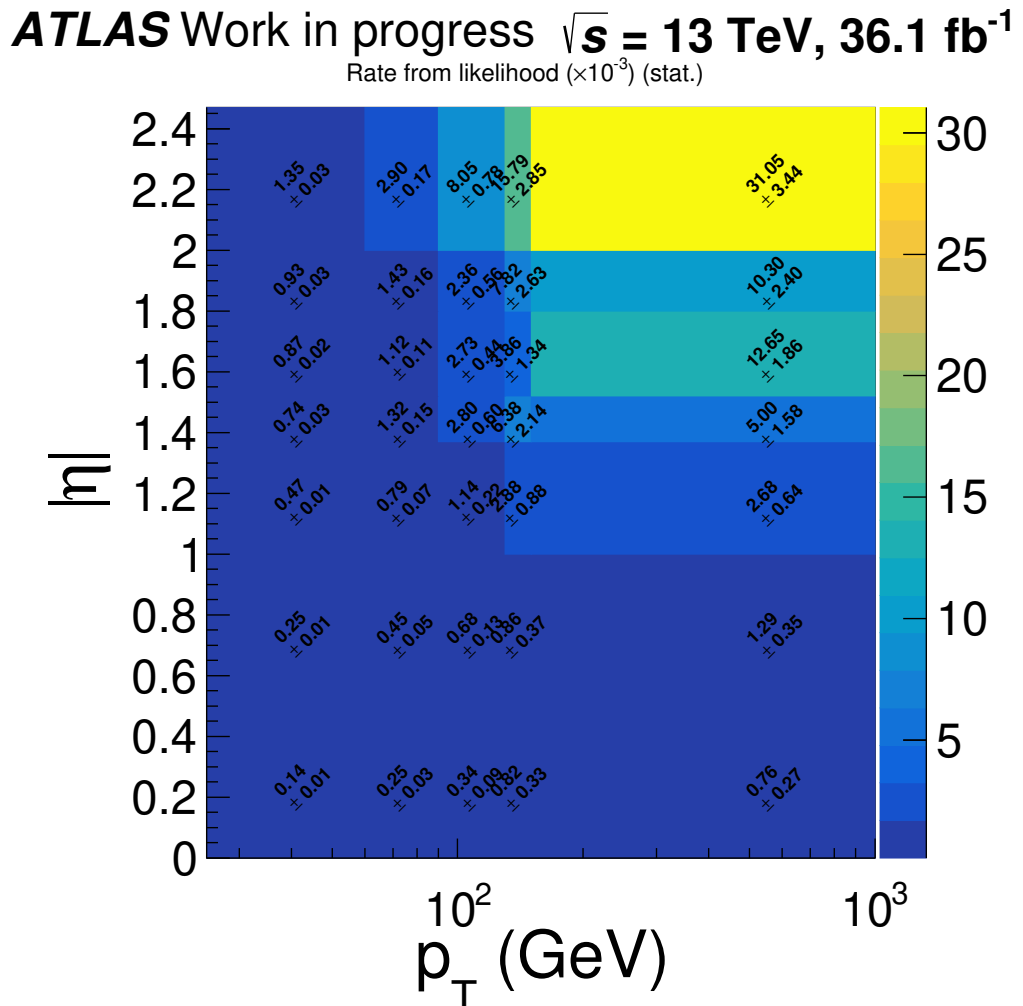


Figure 5.4: The measured values of the charge-flip rate ϵ_i in data. Only uncertainties due to the likelihood method are included.

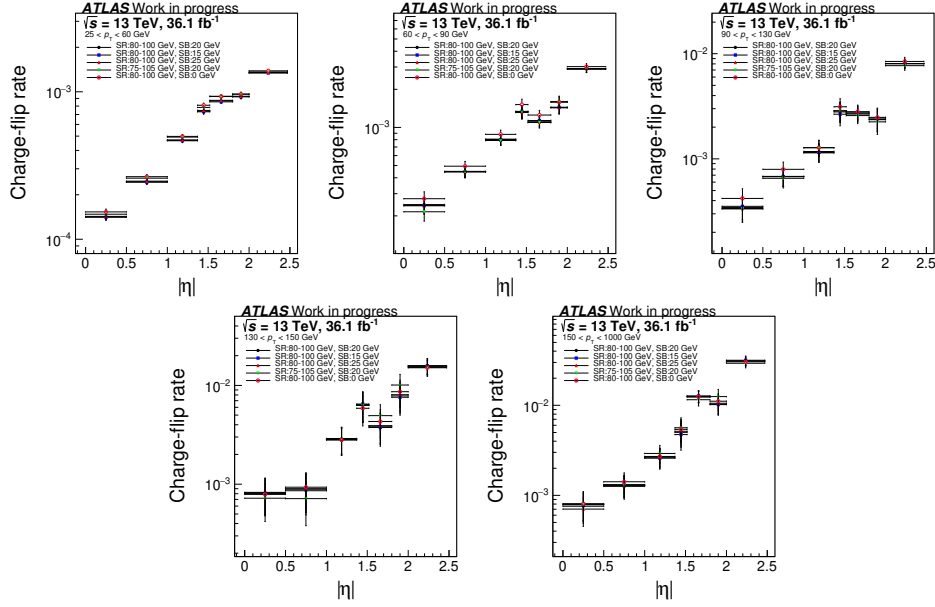


Figure 5.5: The systematic variations of the charge-flip rate ϵ_i in data, due to the background subtraction.

- Central region: 75 - 105 GeV; Sideband width: 20 GeV
- Central region: 80 - 100 GeV; no background subtraction

For each bin, the largest deviation from the nominal among these variations is the systematic uncertainty due to background subtraction.

$$\sigma_{\text{bgk}} = \max\{|\sigma_{\text{nominal}} - \sigma_{\text{variation}}|\} \quad (5.25)$$

Figure 5.5 shows the variations of the resulting charge flip rate, due to these 4 variations.

5.1.6 Systematic uncertainties due to likelihood method

The systematic uncertainties due to likelihood method are estimated by the difference between the likelihood method and the MC truth method. In the MC truth method, the charge-flip rate is estimated by using the truth information in the $Z \rightarrow ee$ MC sample inside the control region. The control region requires exactly 2 signal electrons. The following are the procedures to match the reconstructed electron to the original electron, in order to find out the original electric charge. In this procedure, some reconstructed electrons cannot be matched. Figure 5.6 shows how the original electron is found in the decay process described in figure 5.1.

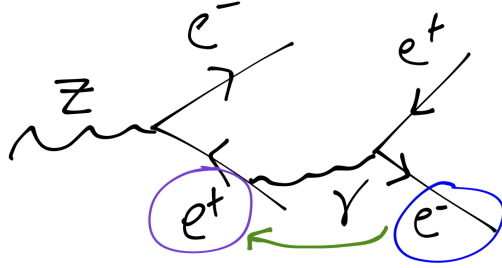


Figure 5.6: This diagram shows how the original electron is found through the decay chain.

1. The reconstructed electron will be matched to the truth particle with the smallest ΔR within the cone $\Delta R < 0.1$.
2. In the following cases, the reconstructed electron are thrown away.
 - (a) No any truth particles can be found inside the cone.
 - (b) The truth particle is not an electron.
 - (c) The origin of the truth electron is not a Z boson.
 - (d) The daughter particle of the Z boson is not an electron.
3. The charge of the daughter electron from the Z boson is the original charge of the reconstructed electron.

Only the events with two reconstructed electrons that are kept in the above procedure are considered. N_{total} is the total number of electrons in these events, and N_{flipped} is the number of electrons that the original charge and the reconstructed charge are different. By calculating the ratio in each bin, the charge flip rate can be estimated by using the MC truth information.

$$\epsilon_{\text{MC truth}} = \frac{N_{\text{flipped}}}{N_{\text{total}}} \quad (5.26)$$

The systematic uncertainties due to likelihood method σ_{truth} is then given by for MC,

$$\sigma_{\text{truth,MC}} = |\epsilon_{\text{lik,MC}} - \epsilon_{\text{MC truth}}| \quad (5.27)$$

for data,

$$\sigma_{\text{truth,data}} = \epsilon_{\text{lik,data}} \times \frac{\sigma_{\text{truth,MC}}}{\epsilon_{\text{lik,MC}}} \quad (5.28)$$

Figure 5.7 shows the comparison of the resulting charge flip rate, between the likelihood method and the MC truth method.

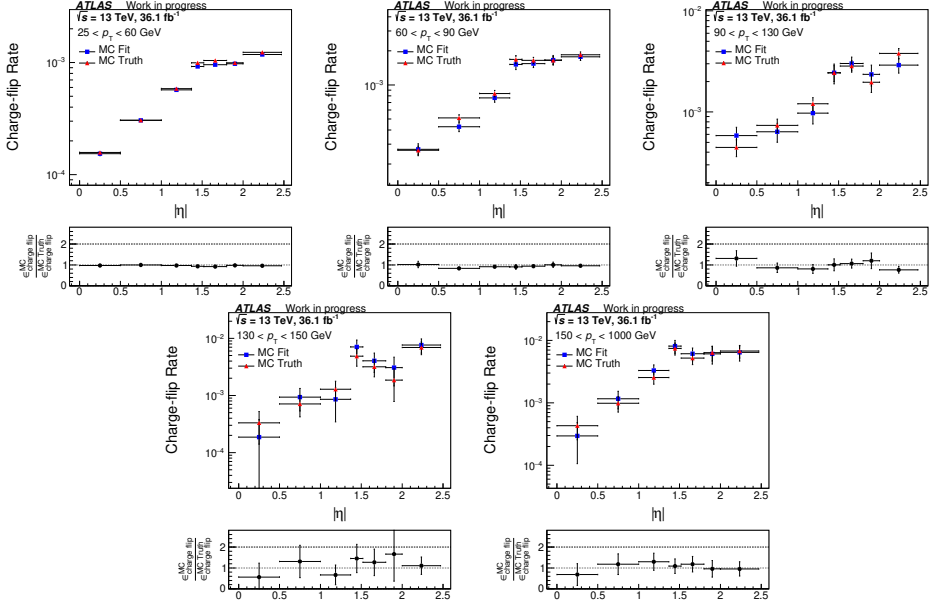


Figure 5.7: The comparisons between the likelihood method and the MC truth method. The systematic uncertainties due to likelihood method can be estimated.

5.1.7 Results with total uncertainties

The total systematic uncertainties is a quadratic sum of systematic uncertainties due to the background subtraction and the likelihood method, described in section 5.1.5 and 5.1.6 respectively.

$$\sigma_{\text{sys}} = \sqrt{\sigma_{\text{bgk}}^2 + \sigma_{\text{truth}}^2} \quad (5.29)$$

The total uncertainties is the quadratic sum of the total systematic uncertainties and the statistical uncertainties in the likelihood method.

$$\sigma_{\text{tot}} = \sqrt{\sigma_{\text{sys}}^2 + \sigma_{\text{lik}}^2} \quad (5.30)$$

Figure 5.8 shows the measured values of the charge-flip rate ϵ_i by using the data, with total uncertainties described in equation 5.30.

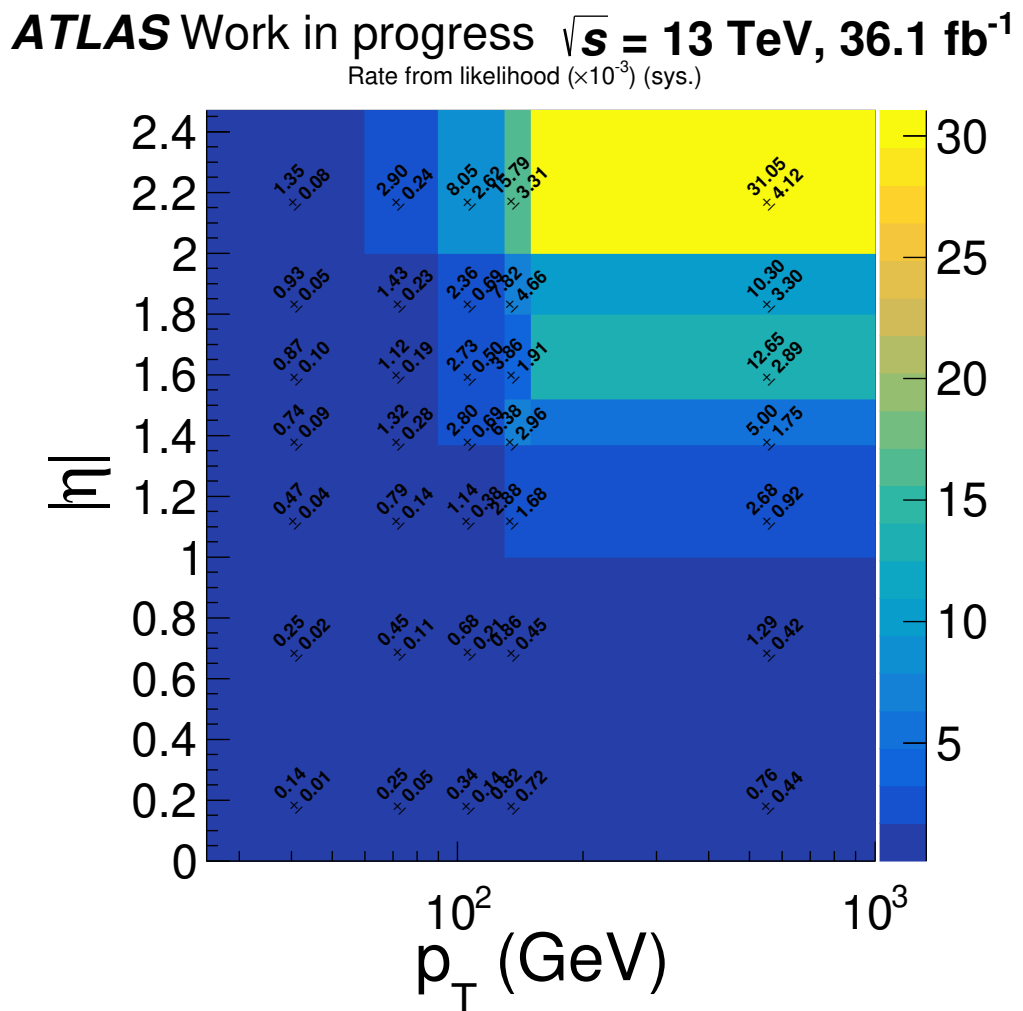


Figure 5.8: The measured values of the charge-flip rate ϵ_i in data, with total uncertainties.

5.1.8 MC validation

The charge flip rate can be validated by using the $Z \rightarrow ee$ MC samples. By using the equation 5.6 and 5.10, N_{SS}^{ij} can be approximated by

$$N_{SS}^{ij} = [\epsilon_i(1 - \epsilon_j) + (1 - \epsilon_i)\epsilon_j]m_{OS}^{ij} \quad (5.31)$$

$$\approx [\epsilon_i(1 - \epsilon_j) + (1 - \epsilon_i)\epsilon_j] \frac{M_{OS}^{ij}}{(1 - \epsilon_i)(1 - \epsilon_j)} \quad (5.32)$$

$$= \frac{\epsilon_i(1 - \epsilon_j) + (1 - \epsilon_i)\epsilon_j}{(1 - \epsilon_i)(1 - \epsilon_j)} M_{OS}^{ij} \quad (5.33)$$

In the equation 5.2, m_{SS}^{ij} is zero for the $Z \rightarrow ee$ MC samples, therefore we have

$$M_{SS}^{ij} = \epsilon_i(1 - \epsilon_j)m_{OS}^{ij} + (1 - \epsilon_i)\epsilon_j m_{OS}^{ij} \quad (5.34)$$

$$= N_{SS}^{ij} \quad (5.35)$$

Hence, it is expected that

$$M_{SS}^{ij} \approx \frac{\epsilon_i(1 - \epsilon_j) + (1 - \epsilon_i)\epsilon_j}{(1 - \epsilon_i)(1 - \epsilon_j)} M_{OS}^{ij} \quad (5.36)$$

By weighting the OS events in MC with the weight,

$$\text{weight} = \frac{\epsilon_i(1 - \epsilon_j) + (1 - \epsilon_i)\epsilon_j}{(1 - \epsilon_i)(1 - \epsilon_j)} \quad (5.37)$$

the weighted OS events and the SS events will be close to each other. This can be used to validate the charge flip rate. Figure 5.9 shows the comparisons between the weighted OS events and the SS events in various distributions, where all event weights are applied except the charge flip scale factor. The weighted OS events and the SS events agree within the uncertainties.

5.2 Fake lepton background

5.2.1 Sources for fake lepton background

The fake lepton background is ascribed to the case that other particles like meson, hadron and photon are misidentified as leptons. Three types of fake lepton background are described as follows.

- Heavy-flavor fakes:

- It comes from semi-leptonic decays of heavy-quark (b or c) hadrons in jets

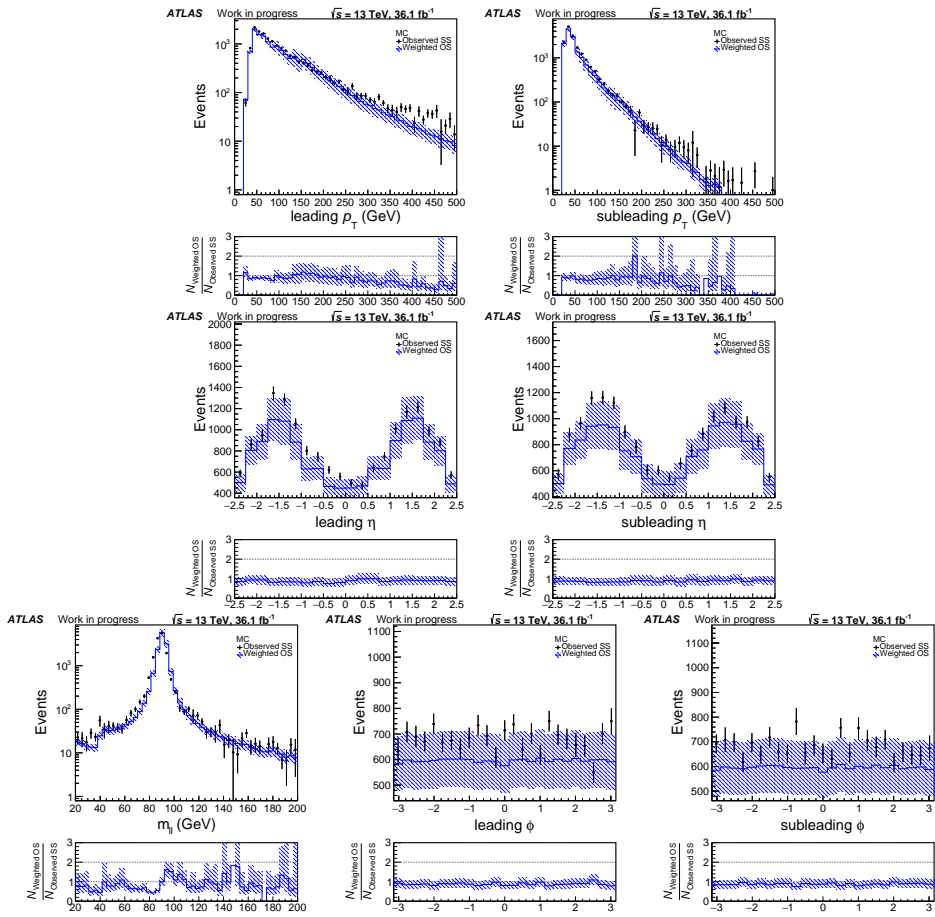


Figure 5.9: The comparisons between the weighted OS events and the SS events.

- Light-flavor fakes:
 - It comes from semi-leptonic decays of light-quark hadrons in jets
 - or comes from mis-reconstructions of jets from light-quark hadrons
- photon conversion:
 - It comes from the pair production from a photon

These leptons do not often pass the lepton identification cuts and have large impact parameters.

5.2.2 Matrix method

The fake lepton background is estimated with the matrix method. The input of this method is the real and fake efficiencies of electron and muon, in different bins of p_T and $|\eta|$, which are measured in the sections 5.2.3 and 5.2.4. This method will estimate the amount of fake lepton background, by counting the number of loose and tight leptons in data. The tight leptons in our analysis are the signal leptons, and the loose leptons are baseline leptons but not signal leptons.

The probability that a real electron (or muon) passes the signal selection (i.e. tight lepton) is denoted by the real efficiency ϵ . The probability that a real electron (or muon) does not pass the signal selection (i.e. loose lepton) is denoted by $\bar{\epsilon} = 1 - \epsilon$. Similarly, the probability that a fake electron (or muon) passes the signal selection (i.e. tight lepton) is denoted by the fake efficiency f . The probability that a fake electron (or muon) does not pass the signal selection (i.e. loose lepton) is denoted by $\bar{f} = 1 - f$. Although there are no subscripts and superscripts for the efficiencies e and f , these efficiencies are different for different flavours of the leptons (electron or muon), and depend on p_T and $|\eta|$.

For simplicity, we first consider the case with only one lepton. We will then generalize to the case with two leptons. By the definition of the efficiencies, the relation between the number of real/fake leptons and the number of tight/loose leptons is given by the following matrix.

$$\begin{pmatrix} N_T \\ N_L \end{pmatrix} = \begin{pmatrix} \epsilon & f \\ \bar{\epsilon} & \bar{f} \end{pmatrix} \begin{pmatrix} N_R \\ N_F \end{pmatrix} \quad (5.38)$$

Because the number of tight/loose leptons can be counted in data, $\begin{pmatrix} N_T \\ N_L \end{pmatrix}$

is known. By inverting the matrix, the original number of fake leptons can be calculated.

$$\begin{pmatrix} 0 \\ N_F \end{pmatrix} = \begin{pmatrix} 0 & 0 \\ 0 & 1 \end{pmatrix} \begin{pmatrix} N_R \\ N_F \end{pmatrix} \\ = \begin{pmatrix} 0 & 0 \\ 0 & 1 \end{pmatrix} \begin{pmatrix} \epsilon & f \\ \bar{\epsilon} & \bar{f} \end{pmatrix}^{-1} \begin{pmatrix} N_T \\ N_L \end{pmatrix} \quad (5.39)$$

The fake lepton background, which is the number of tight lepton due to the fake lepton, N'_T , can then be found, by re-apply the matrix in equation 5.38.

$$\begin{pmatrix} N'_T \\ N'_L \end{pmatrix} = \begin{pmatrix} \epsilon & f \\ \bar{\epsilon} & \bar{f} \end{pmatrix} \begin{pmatrix} 0 \\ N_F \end{pmatrix} \\ = \begin{pmatrix} \epsilon & f \\ \bar{\epsilon} & \bar{f} \end{pmatrix} \begin{pmatrix} 0 & 0 \\ 0 & 1 \end{pmatrix} \begin{pmatrix} \epsilon & f \\ \bar{\epsilon} & \bar{f} \end{pmatrix}^{-1} \begin{pmatrix} N_T \\ N_L \end{pmatrix} \\ N'_T = \begin{pmatrix} \epsilon & f \end{pmatrix} \begin{pmatrix} 0 & 0 \\ 0 & 1 \end{pmatrix} \begin{pmatrix} \epsilon & f \\ \bar{\epsilon} & \bar{f} \end{pmatrix}^{-1} \begin{pmatrix} N_T \\ N_L \end{pmatrix} \quad (5.40)$$

To generalize to the case with two leptons, equation 5.38 becomes

$$\begin{pmatrix} N_{TT} \\ N_{TL} \\ N_{LT} \\ N_{LL} \end{pmatrix} = \begin{pmatrix} \epsilon_1\epsilon_2 & \epsilon_1f_2 & f_1\epsilon_2 & f_1f_2 \\ \epsilon_1\bar{\epsilon}_2 & \epsilon_1\bar{f}_2 & f_1\bar{\epsilon}_2 & f_1\bar{f}_2 \\ \bar{\epsilon}_1\epsilon_2 & \bar{\epsilon}_1f_2 & \bar{f}_1\epsilon_2 & \bar{f}_1f_2 \\ \bar{\epsilon}_1\bar{\epsilon}_2 & \bar{\epsilon}_1\bar{f}_2 & \bar{f}_1\bar{\epsilon}_2 & \bar{f}_1\bar{f}_2 \end{pmatrix} \begin{pmatrix} N_{RR} \\ N_{RF} \\ N_{FR} \\ N_{FF} \end{pmatrix} \quad (5.41)$$

where the subscripts 1 and 2 of the efficiencies denote the leading lepton and sub-leading lepton respectively. The two letters in the subscript of N describe the types of the leading and sub-leading lepton respectively. N_{RF} , N_{FR} , N_{FF} can be found by inverting the matrix.

$$\begin{pmatrix} 0 \\ N_{RF} \\ N_{FR} \\ N_{FF} \end{pmatrix} = \begin{pmatrix} 0 & 0 & 0 & 0 \\ 0 & 1 & 0 & 0 \\ 0 & 0 & 1 & 0 \\ 0 & 0 & 0 & 1 \end{pmatrix} \begin{pmatrix} N_{RR} \\ N_{RF} \\ N_{FR} \\ N_{FF} \end{pmatrix} \\ = \begin{pmatrix} 0 & 0 & 0 & 0 \\ 0 & 1 & 0 & 0 \\ 0 & 0 & 1 & 0 \\ 0 & 0 & 0 & 1 \end{pmatrix} \begin{pmatrix} \epsilon_1\epsilon_2 & \epsilon_1f_2 & f_1\epsilon_2 & f_1f_2 \\ \epsilon_1\bar{\epsilon}_2 & \epsilon_1\bar{f}_2 & f_1\bar{\epsilon}_2 & f_1\bar{f}_2 \\ \bar{\epsilon}_1\epsilon_2 & \bar{\epsilon}_1f_2 & \bar{f}_1\epsilon_2 & \bar{f}_1f_2 \\ \bar{\epsilon}_1\bar{\epsilon}_2 & \bar{\epsilon}_1\bar{f}_2 & \bar{f}_1\bar{\epsilon}_2 & \bar{f}_1\bar{f}_2 \end{pmatrix}^{-1} \begin{pmatrix} N_{TT} \\ N_{TL} \\ N_{LT} \\ N_{LL} \end{pmatrix} \quad (5.42)$$

The fake lepton background, which is the number of tight-tight lepton due to the fake lepton, N'_{TT} , can then be found.

$$\begin{aligned}
\begin{pmatrix} N'_{TT} \\ N'_{TL} \\ N'_{LT} \\ N'_{LL} \end{pmatrix} &= \begin{pmatrix} \epsilon_1\epsilon_2 & \epsilon_1f_2 & f_1\epsilon_2 & f_1f_2 \\ \epsilon_1\bar{\epsilon}_2 & \epsilon_1\bar{f}_2 & f_1\bar{\epsilon}_2 & f_1\bar{f}_2 \\ \bar{\epsilon}_1\epsilon_2 & \bar{\epsilon}_1f_2 & \bar{f}_1\epsilon_2 & \bar{f}_1f_2 \\ \bar{\epsilon}_1\bar{\epsilon}_2 & \bar{\epsilon}_1\bar{f}_2 & \bar{f}_1\bar{\epsilon}_2 & \bar{f}_1\bar{f}_2 \end{pmatrix} \begin{pmatrix} 0 \\ N_{RF} \\ N_{FR} \\ N_{FF} \end{pmatrix} \\
&= \begin{pmatrix} \epsilon_1\epsilon_2 & \epsilon_1f_2 & f_1\epsilon_2 & f_1f_2 \\ \epsilon_1\bar{\epsilon}_2 & \epsilon_1\bar{f}_2 & f_1\bar{\epsilon}_2 & f_1\bar{f}_2 \\ \bar{\epsilon}_1\epsilon_2 & \bar{\epsilon}_1f_2 & \bar{f}_1\epsilon_2 & \bar{f}_1f_2 \\ \bar{\epsilon}_1\bar{\epsilon}_2 & \bar{\epsilon}_1\bar{f}_2 & \bar{f}_1\bar{\epsilon}_2 & \bar{f}_1\bar{f}_2 \end{pmatrix} \begin{pmatrix} 0 & 0 & 0 & 0 \\ 0 & 1 & 0 & 0 \\ 0 & 0 & 1 & 0 \\ 0 & 0 & 0 & 1 \end{pmatrix} \begin{pmatrix} \epsilon_1\epsilon_2 & \epsilon_1f_2 & f_1\epsilon_2 & f_1f_2 \\ \epsilon_1\bar{\epsilon}_2 & \epsilon_1\bar{f}_2 & f_1\bar{\epsilon}_2 & f_1\bar{f}_2 \\ \bar{\epsilon}_1\epsilon_2 & \bar{\epsilon}_1f_2 & \bar{f}_1\epsilon_2 & \bar{f}_1f_2 \\ \bar{\epsilon}_1\bar{\epsilon}_2 & \bar{\epsilon}_1\bar{f}_2 & \bar{f}_1\bar{\epsilon}_2 & \bar{f}_1\bar{f}_2 \end{pmatrix}^{-1} \begin{pmatrix} N_{TT} \\ N_{TL} \\ N_{LT} \\ N_{LL} \end{pmatrix} \\
N'_{TT} &= \left(\begin{array}{cccc} \epsilon_1\epsilon_2 & \epsilon_1f_2 & f_1\epsilon_2 & f_1f_2 \end{array} \right) \begin{pmatrix} 0 & 0 & 0 & 0 \\ 0 & 1 & 0 & 0 \\ 0 & 0 & 1 & 0 \\ 0 & 0 & 0 & 1 \end{pmatrix} \begin{pmatrix} \epsilon_1\epsilon_2 & \epsilon_1f_2 & f_1\epsilon_2 & f_1f_2 \\ \epsilon_1\bar{\epsilon}_2 & \epsilon_1\bar{f}_2 & f_1\bar{\epsilon}_2 & f_1\bar{f}_2 \\ \bar{\epsilon}_1\epsilon_2 & \bar{\epsilon}_1f_2 & \bar{f}_1\epsilon_2 & \bar{f}_1f_2 \\ \bar{\epsilon}_1\bar{\epsilon}_2 & \bar{\epsilon}_1\bar{f}_2 & \bar{f}_1\bar{\epsilon}_2 & \bar{f}_1\bar{f}_2 \end{pmatrix}^{-1} \begin{pmatrix} N_{TT} \\ N_{TL} \\ N_{LT} \\ N_{LL} \end{pmatrix} \tag{5.43}
\end{aligned}$$

Equation 5.43 can be applied to any combination of the flavours, p_T and $|\eta|$ of the leading and sub-leading lepton. In principle, the total amount of fake lepton background should be the summation of all combinations of the flavours, p_T and $|\eta|$. For a particular combination, the counting result of the tight/loose leptons in

data $\begin{pmatrix} N_{TT} \\ N_{TL} \\ N_{LT} \\ N_{LL} \end{pmatrix}$ can be split into “one”, which is the contribution by one event:

$$\begin{pmatrix} N_{TT} \\ N_{TL} \\ N_{LT} \\ N_{LL} \end{pmatrix} = \sum_{i=1}^{N_{TT}} \begin{pmatrix} 1 \\ 0 \\ 0 \\ 0 \end{pmatrix} + \sum_{i=1}^{N_{TL}} \begin{pmatrix} 0 \\ 1 \\ 0 \\ 0 \end{pmatrix} + \sum_{i=1}^{N_{LT}} \begin{pmatrix} 0 \\ 0 \\ 1 \\ 0 \end{pmatrix} + \sum_{i=1}^{N_{LL}} \begin{pmatrix} 0 \\ 0 \\ 0 \\ 1 \end{pmatrix} \tag{5.44}$$

Because equation 5.43 is a linear function, we can first calculate the small contribution of N'_{TT} from one event, and assign this value as a weight to the event. This weight is called the fake weight of the event. The total fake lepton background is then the sum of the fake weight of all events in data. For example, if a pair of two leptons is a tight-tight pair, the fake weight of this event is N'_{TT} in the following

equation.

$$N'_{TT} = \begin{pmatrix} \epsilon_1\epsilon_2 & \epsilon_1f_2 & f_1\epsilon_2 & f_1f_2 \end{pmatrix} \begin{pmatrix} 0 & 0 & 0 & 0 \\ 0 & 1 & 0 & 0 \\ 0 & 0 & 1 & 0 \\ 0 & 0 & 0 & 1 \end{pmatrix} \begin{pmatrix} \epsilon_1\epsilon_2 & \epsilon_1f_2 & f_1\epsilon_2 & f_1f_2 \\ \epsilon_1\bar{\epsilon}_2 & \epsilon_1\bar{f}_2 & f_1\bar{\epsilon}_2 & f_1\bar{f}_2 \\ \bar{\epsilon}_1\epsilon_2 & \bar{\epsilon}_1f_2 & \bar{f}_1\epsilon_2 & \bar{f}_1f_2 \\ \bar{\epsilon}_1\bar{\epsilon}_2 & \bar{\epsilon}_1\bar{f}_2 & \bar{f}_1\bar{\epsilon}_2 & \bar{f}_1\bar{f}_2 \end{pmatrix}^{-1} \begin{pmatrix} 1 \\ 0 \\ 0 \\ 0 \end{pmatrix} \quad (5.45)$$

where the flavours, p_T and $|\eta|$ of the efficiencies are simply the flavours, p_T and $|\eta|$ of the leading and sub-leading lepton in this event.

By inverting the matrix, equation 5.43 can be simplified. First, we define a variable d .

$$d = (\epsilon_1 - f_1)(\epsilon_2 - f_2) \quad (5.46)$$

The inverse of the matrix is given by

$$\begin{pmatrix} \epsilon_1\epsilon_2 & \epsilon_1f_2 & f_1\epsilon_2 & f_1f_2 \\ \epsilon_1\bar{\epsilon}_2 & \epsilon_1\bar{f}_2 & f_1\bar{\epsilon}_2 & f_1\bar{f}_2 \\ \bar{\epsilon}_1\epsilon_2 & \bar{\epsilon}_1f_2 & \bar{f}_1\epsilon_2 & \bar{f}_1f_2 \\ \bar{\epsilon}_1\bar{\epsilon}_2 & \bar{\epsilon}_1\bar{f}_2 & \bar{f}_1\bar{\epsilon}_2 & \bar{f}_1\bar{f}_2 \end{pmatrix}^{-1} = \frac{1}{d} \begin{pmatrix} \bar{f}_1\bar{f}_2 & -\bar{f}_1f_2 & -f_1\bar{f}_2 & f_1f_2 \\ -\bar{f}_1\bar{\epsilon}_2 & \bar{f}_1\epsilon_2 & f_1\bar{\epsilon}_2 & -f_1\epsilon_2 \\ -\bar{\epsilon}_1\bar{f}_2 & \bar{\epsilon}_1f_2 & \epsilon_1\bar{f}_2 & -\epsilon_1f_2 \\ \bar{\epsilon}_1\bar{\epsilon}_2 & -\bar{\epsilon}_1\epsilon_2 & -\epsilon_1\bar{\epsilon}_2 & \epsilon_1\epsilon_2 \end{pmatrix} \quad (5.47)$$

Equation 5.43 becomes

$$N'_{TT} = \begin{pmatrix} \epsilon_1\epsilon_2 & \epsilon_1f_2 & f_1\epsilon_2 & f_1f_2 \end{pmatrix} \begin{pmatrix} 0 & 0 & 0 & 0 \\ 0 & 1 & 0 & 0 \\ 0 & 0 & 1 & 0 \\ 0 & 0 & 0 & 1 \end{pmatrix} \frac{1}{d} \begin{pmatrix} \bar{f}_1\bar{f}_2 & -\bar{f}_1f_2 & -f_1\bar{f}_2 & f_1f_2 \\ -\bar{f}_1\bar{\epsilon}_2 & \bar{f}_1\epsilon_2 & f_1\bar{\epsilon}_2 & -f_1\epsilon_2 \\ -\bar{\epsilon}_1\bar{f}_2 & \bar{\epsilon}_1f_2 & \epsilon_1\bar{f}_2 & -\epsilon_1f_2 \\ \bar{\epsilon}_1\bar{\epsilon}_2 & -\bar{\epsilon}_1\epsilon_2 & -\epsilon_1\bar{\epsilon}_2 & \epsilon_1\epsilon_2 \end{pmatrix} \begin{pmatrix} N_{TT} \\ N_{TL} \\ N_{LT} \\ N_{LL} \end{pmatrix}$$

$$= \frac{1}{d} \begin{pmatrix} \epsilon_1\epsilon_2 & \epsilon_1f_2 & f_1\epsilon_2 & f_1f_2 \end{pmatrix} \begin{pmatrix} 0 & 0 & 0 & 0 \\ -\bar{f}_1\bar{\epsilon}_2 & \bar{f}_1\epsilon_2 & f_1\bar{\epsilon}_2 & -f_1\epsilon_2 \\ -\bar{\epsilon}_1\bar{f}_2 & \bar{\epsilon}_1f_2 & \epsilon_1\bar{f}_2 & -\epsilon_1f_2 \\ \bar{\epsilon}_1\bar{\epsilon}_2 & -\bar{\epsilon}_1\epsilon_2 & -\epsilon_1\bar{\epsilon}_2 & \epsilon_1\epsilon_2 \end{pmatrix} \begin{pmatrix} N_{TT} \\ N_{TL} \\ N_{LT} \\ N_{LL} \end{pmatrix} \quad (5.48)$$

For a tight-tight pair,

$$\text{fake weight} = \frac{1}{d}(-\epsilon_1\bar{f}_1\bar{\epsilon}_2f_2 - \bar{\epsilon}_1f_1\epsilon_2\bar{f}_2 + \bar{\epsilon}_1f_1\bar{\epsilon}_2f_2) \quad (5.49)$$

For a tight-loose pair,

$$\begin{aligned} \text{fake weight} &= \frac{1}{d}(\epsilon_1\bar{f}_1\epsilon_2f_2 + \bar{\epsilon}_1f_1\epsilon_2f_2 - \bar{\epsilon}_1f_1\epsilon_2f_2) \\ &= \frac{\epsilon_1\bar{f}_1\epsilon_2f_2}{d} \end{aligned} \quad (5.50)$$

For a loose-tight pair,

$$\begin{aligned}\text{fake weight} &= \frac{1}{d}(\epsilon_1 f_1 \bar{\epsilon}_2 f_2 + \epsilon_1 f_1 \epsilon_2 \bar{f}_2 - \epsilon_1 f_1 \bar{\epsilon}_2 f_2) \\ &= \frac{\epsilon_1 f_1 \epsilon_2 \bar{f}_2}{d}\end{aligned}\tag{5.51}$$

For a loose-loose pair,

$$\begin{aligned}\text{fake weight} &= \frac{1}{d}(-\epsilon_1 f_1 \epsilon_2 f_2 - \epsilon_1 f_1 \epsilon_2 f_2 + \epsilon_1 f_1 \epsilon_2 f_2) \\ &= -\frac{\epsilon_1 f_1 \epsilon_2 f_2}{d}\end{aligned}\tag{5.52}$$

5.2.3 Measurement of real efficiencies

The real efficiencies ϵ_i are measured by the Z boson tag-and-probe method. This method is based on the fact that the Z bosons decay into two opposite-sign electrons or two muons and the invariant mass of the two leptons is the mass of the Z boson (close to 91 GeV). By selecting two opposite-sign same-flavour leptons with the invariant mass $80 \text{ GeV} < m_{ll} < 100 \text{ GeV}$, these two leptons are likely to be real leptons from a Z boson decay. If one of the leptons is a signal lepton, called the tag lepton, another lepton called the probe lepton is very likely to be a real lepton. By counting the total number of baseline leptons and signal leptons for the probe lepton, the real efficiencies ϵ can be measured. The counting is done in the data sample, and hence this is a data-driven method.

$$\epsilon = \frac{N_{\text{signal}}^{\text{data}}}{N_{\text{baseline}}^{\text{data}}}\tag{5.53}$$

The selections for the control region used in the measurement of real efficiencies is, on top of the selections in section 3.2, as follows:

- The two leptons are two electrons or two muons.
- The electric charges of the two leptons are opposite sign.
- $80 \text{ GeV} < m_{ll} < 100 \text{ GeV}$

If the two leptons are both signal leptons, both leptons can be tag leptons to increase the statistics.

The binning for p_T and $|\eta|$ is shown in table 5.2.

The results for the real efficiencies are shown in figure 5.10.

Variable	Boundary of the bins
p_T (GeV)	25, 35, 45, 55, 65, 75, 85, 95
$ \eta $ (For electrons)	0, 0.8, 1.37, 1.52, 2.47
$ \eta $ (For muons)	0, 0.6, 1.2, 1.8, 2.4

Table 5.2: Binning in p_T and $|\eta|$ for real efficiencies.

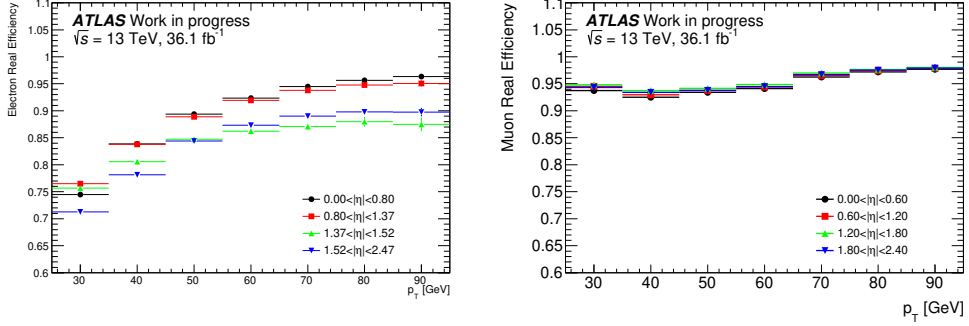


Figure 5.10: The real efficiencies for electrons (left) and muons (right). Only statistical uncertainties are considered.

5.2.4 Measurement of fake efficiencies

The fake efficiencies are measured by the tag-and-probe method, similar to the real efficiencies. On top of the selections in section 3.2, two different control regions are defined for electron and muon respectively. The control regions contain rich heavy-flavor fakes by requiring at least one b-jet. The selections for the control regions are summarized as follows:

- For electron fake efficiencies, one lepton is a muon and another is an electron.
For muons fake efficiencies, the two leptons are both muons.
- The electric charges of the two leptons are same sign.
- There is at least 1 b-jet.

In both control regions, the tag leptons must be a signal muon with $p_T > 40$ GeV. The probe lepton is very likely to a fake lepton from heavy-flavor jets, because the two leptons are same-sign and the tag lepton is very likely to be a real lepton. By counting the number of the baseline and signal probe leptons, the fake efficiencies can be estimated. This counting is done in the data samples. In order to ensure that the probe leptons are not coming from real leptons, the

number of real leptons estimated by the MC sample is subtracted. These MC samples include WZ, WW, ZZ, VVV, higgs, multi-top and ttV.

$$f = \frac{N_{\text{signal}}}{N_{\text{baseline}}} \quad (5.44)$$

$$= \frac{N_{\text{signal}}^{\text{data}} - N_{\text{signal}}^{\text{MC, real}}}{N_{\text{baseline}}^{\text{data}} - N_{\text{baseline}}^{\text{MC, real}}} \quad (5.45)$$

The identification of the real leptons in the MC samples is using the truth information. It classifies the reconstructed lepton into different types of truth particle. The origin of the reconstructed lepton are known.

The binning for p_T and $|\eta|$ is shown in table 5.3.

Variable	Boundary of the bins
Electrons	
p_T (GeV)	25, 35, 45, 120, 200
$ \eta $	0, 1.37, 1.52, 2.47
Muons	
p_T (GeV)	25, 30, 45, 120, 200
$ \eta $	0, 1.37, 1.52, 2.4

Table 5.3: Binning in p_T and $|\eta|$ for fake efficiencies.

The results for the fake efficiencies are shown in figure 5.11.

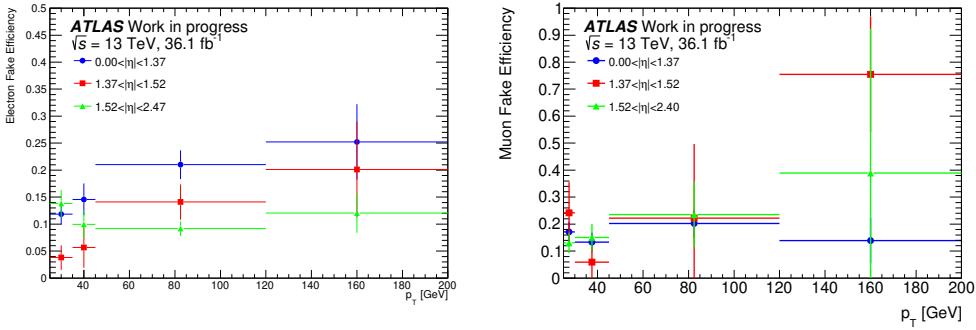


Figure 5.11: The fake efficiencies for electrons (left) and muons (right). Only statistical uncertainties are considered.

5.2.5 Validation for the fake lepton background

In order to validate the fake lepton background, we compare data with all background predictions including the fake lepton background in validation regions.

The validation region is expected to have small contribution from signal. It is defined as follows on top of the selections in section 3.2.

- The two leptons are signal leptons.
- The two leptons are same-sign.
- b-jets veto: $n_{\text{b-jets}} = 0$, to suppress top background.
- At least one signal jet: $n_{\text{jets}} \geq 1$
- Z veto: $|m_{ll} - m_Z| > 10 \text{ GeV}$, to suppress Z+jets background.
- $E_T^{\text{miss}} > 30 \text{ GeV}$
- $m_{\text{eff}} > 200 \text{ GeV}$

To ensure that the contribution from signal is small, the fractions of the signal contribution are checked in figure 5.12, and they are below 7%. In addition, in order to make sure that there is a substantial contribution from fake lepton background, the background compositions are checked in table 5.4. The validation region is split into 3 channels: electron-electron, muon-muon and electron-muon channel. Their fake contributions are 65%, 24% and 48% respectively.

The backgrounds and the data are compared in several variable distributions in the 3 channels, shown in figures 5.13, 5.14 and 5.15 respectively. There are good agreements between the backgrounds and the data within the uncertainties.

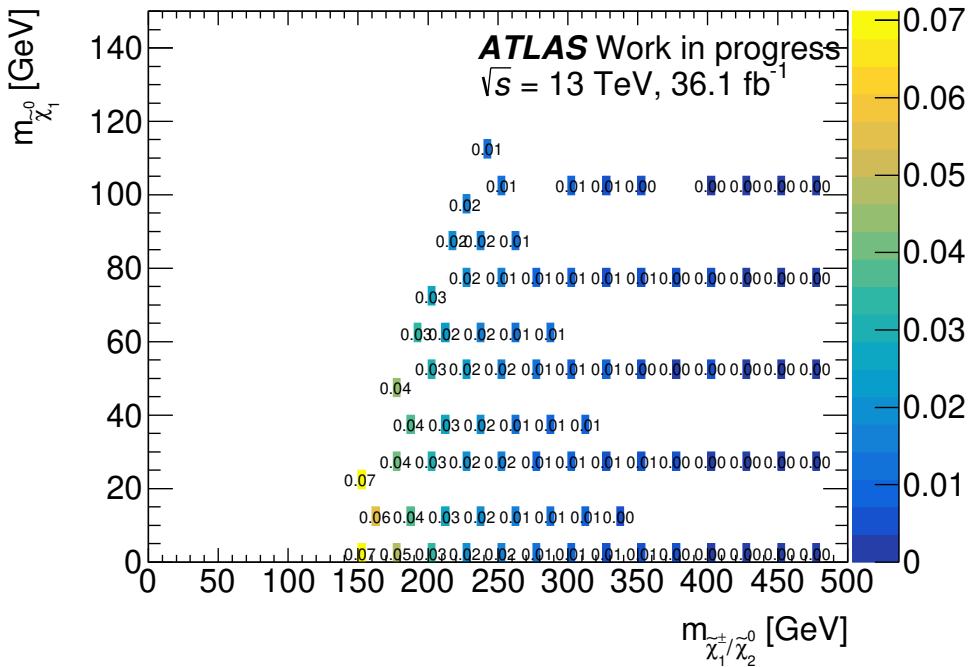


Figure 5.12: Signal contributions in the validation region are shown for different mass points.

	ee channel	$\mu\mu$ channel	e μ channel
Fakes	65.1% (860.7)	23.6% (96.2)	47.8% (614.7)
Charge Flip	12.7% (168.0)	0.0% (0.0)	2.6% (34.0)
WZ	15.2% (201.1)	51.2% (209.2)	35.0% (450.7)
ZZ	0.6% (8.4)	2.3% (9.5)	1.6% (20.4)
WW	3.4% (45.2)	13.1% (53.7)	7.6% (98.3)
Rare	2.3% (30.8)	7.5% (30.5)	3.9% (50.0)
ttV	0.6% (8.3)	2.3% (9.4)	1.4% (18.1)
Total BG	1322	408.4	1286
Data	1201	454	1410

Table 5.4: The background compositions in the validation region. The numbers in brackets are the event yields.

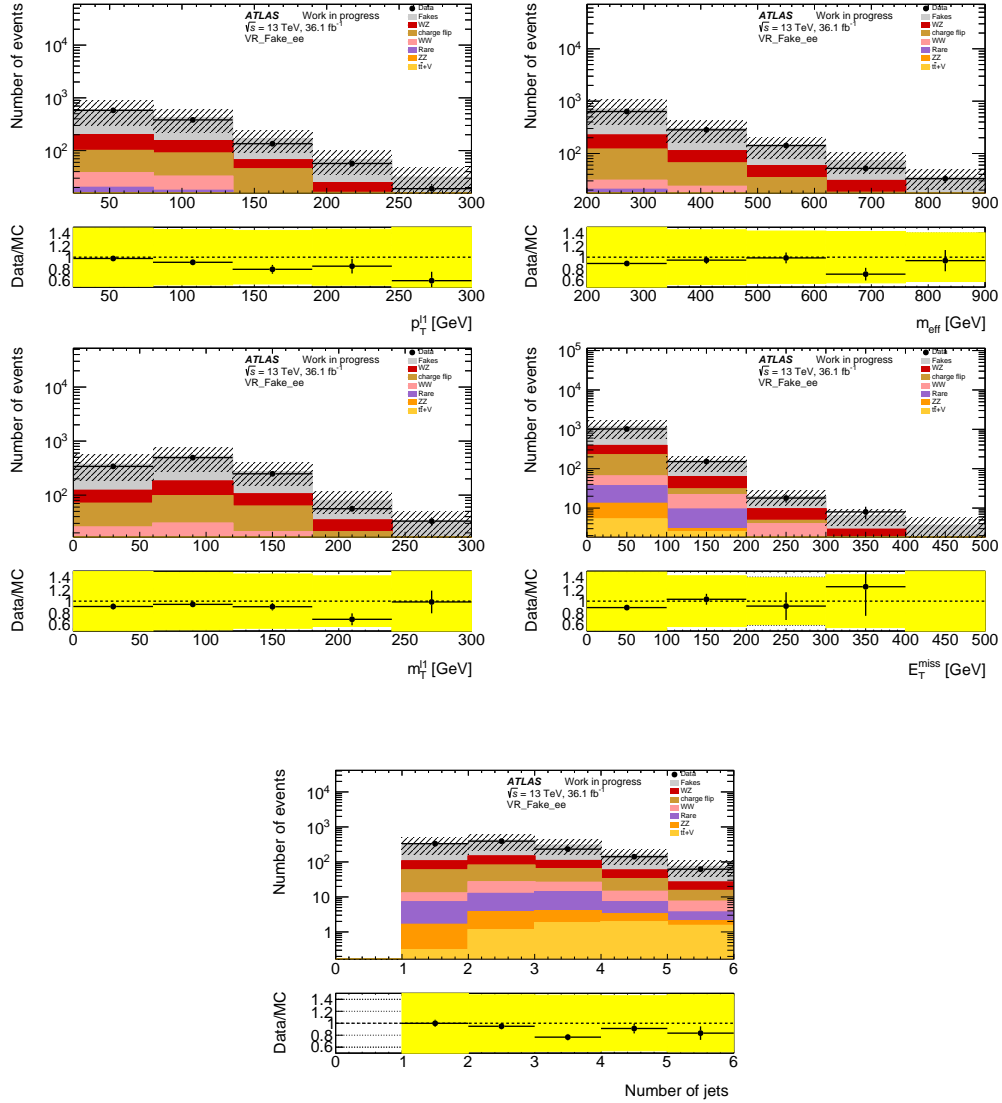


Figure 5.13: Distribution of the leading lepton p_T , m_{eff} , m_T , E_T^{miss} and n_{jets} in the electron-electron channel. The ratio of data to background yields is shown in the lower plot. The error bar includes all the systematic uncertainties except for the theoretical uncertainties.

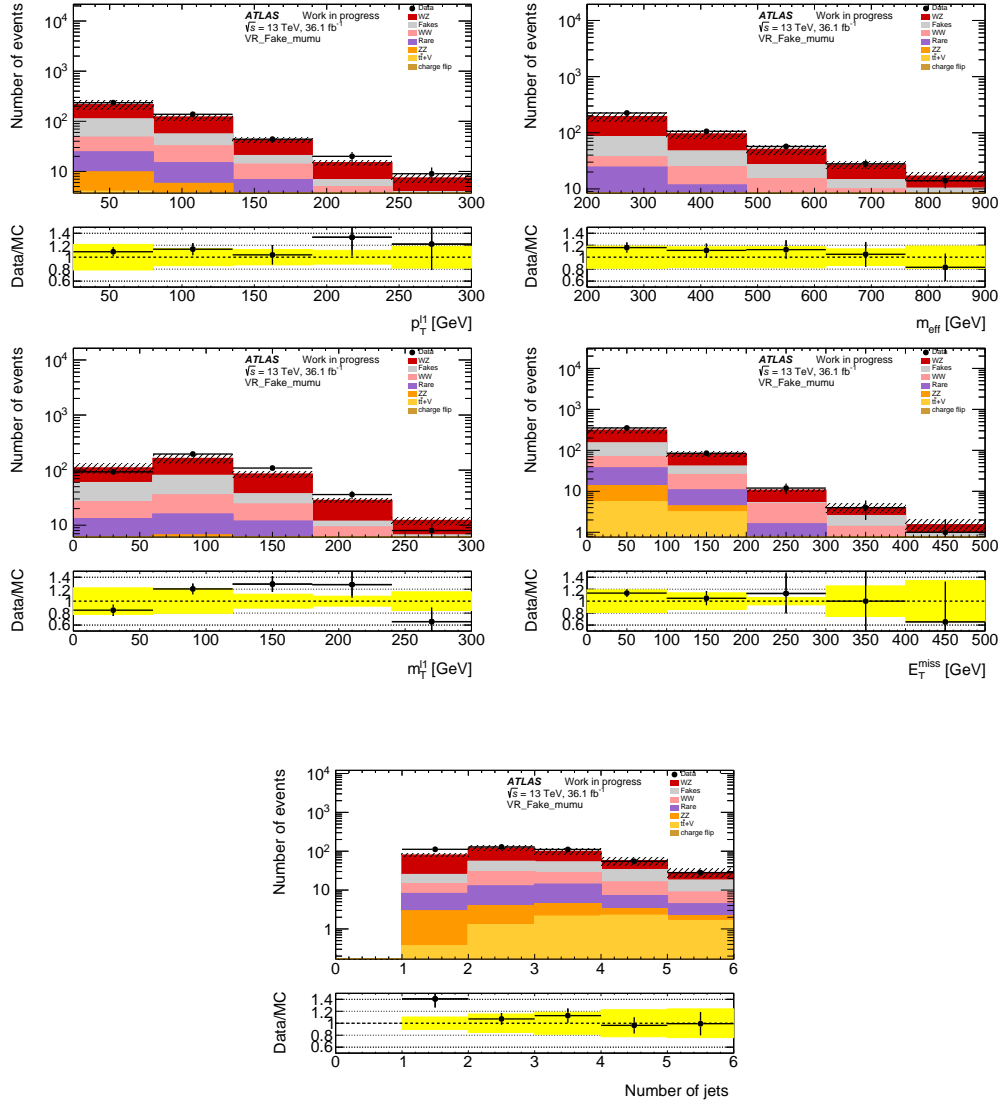


Figure 5.14: Distribution of the leading lepton p_T , m_{eff} , m_T , E_T^{miss} and n_{jets} in the muon-muon channel. The ratio of data to background yields is shown in the lower plot. The error bar includes all the systematic uncertainties except for the theoretical uncertainties.

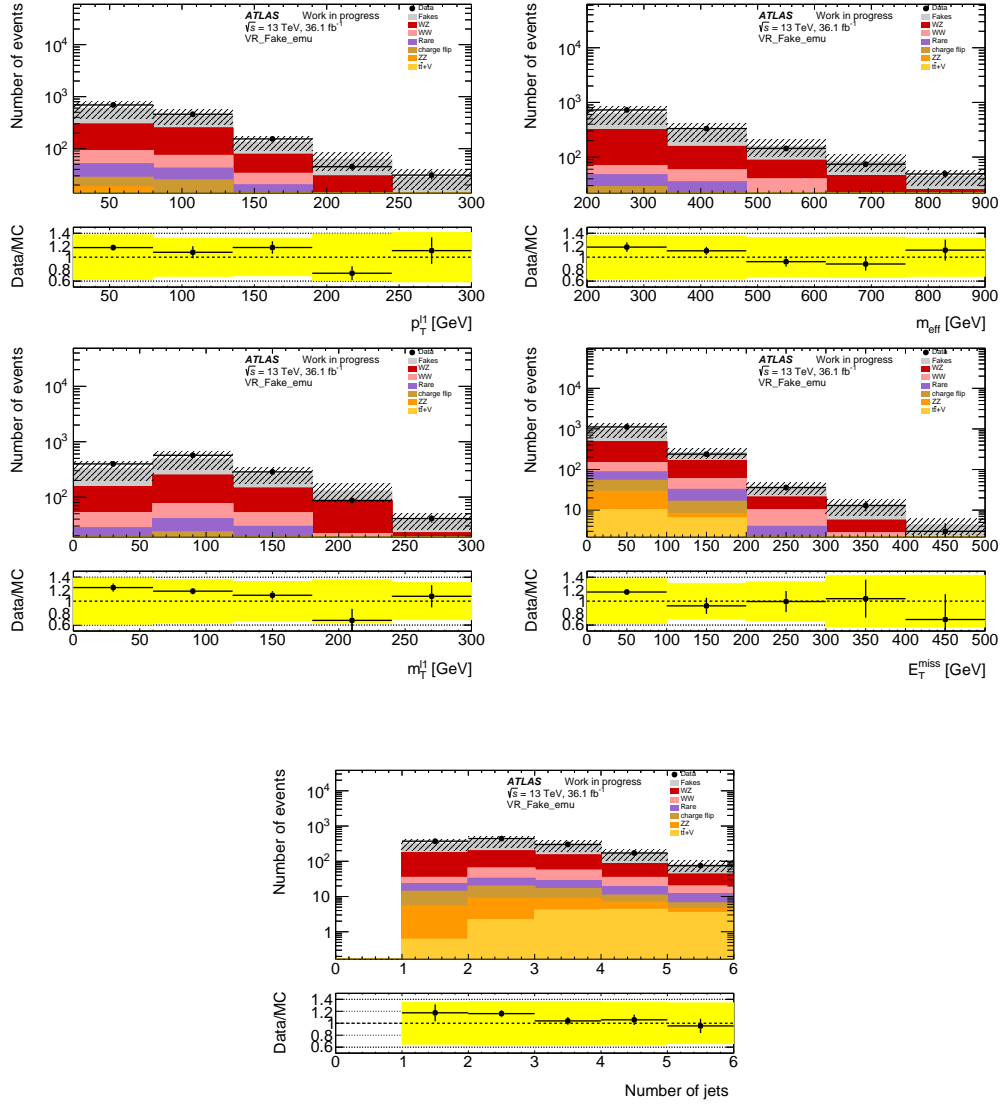


Figure 5.15: Distribution of the leading lepton p_T , m_{eff} , m_T , E_T^{miss} and n_{jets} in the electron-muon channel. The ratio of data to background yields is shown in the lower plot. The error bar includes all the systematic uncertainties except for the theoretical uncertainties.

Chapter 6

Validation regions

In order to ensure the estimations of the backgrounds are robust, two validation regions (VRjet1 and VRjet23) are defined for the corresponding two signal regions (SRjet1 and SRjet23), to compare the backgrounds and the data. There are three requirements for the validation regions:

- The signal contribution is small.
- The validation region is orthogonal to the corresponding signal region.
- The background composition is similar to the corresponding signal region.

The definitions of the two validation regions are summarized in table 6.1.

Cut	VRjet1	VRjet23
n_{jets}	1	[2, 3]
$\Delta\eta_{ll}$	< 1.5	—
E_T^{miss} [GeV]	[70, 100]	> 100
m_T [GeV]	> 140	[65, 120]
m_{eff} [GeV]	—	> 240
$m_{l(j)}$ [GeV]	> 130	> 130
m_{T2} [GeV]	—	—

Table 6.1: The definition of the two validation regions on top of the pre-selections in section 4.2.1. The values in red colour represent different cuts compared to the signal regions.

For the VRjet1, the validation region is obtained by reversing the E_T^{miss} cut compared to the signal region. This can ensure that the validation region is

orthogonal to the SRjet1. The lower cut of E_T^{miss} is optimized to 70 GeV. Such a similar background composition is obtained compared with the SRjet1. The cut on m_{lj} is reversed and relaxed, in order to reduce the signal contribution and increase the statistics. The cuts of m_{eff} and m_{T2} are also removed to increase the statistics.

For the VRjet23, the validation region is obtained by reversing the m_T cut. This can ensure that the validation region is orthogonal to the SRjet23. The cut is optimized to 65 GeV to have a similar background composition. The cut on m_{ljj} is reversed to reduce the signal contribution. To increase the statistics, the m_{T2} cut is removed.

The fractions of signal contribution at different mass points are shown in figure 6.1. The signal contributions are below 12% and 10% for VRjet1 and VRjet23 respectively. Figures 6.2 and 6.3 show the background composition in the validation regions and in the corresponding signal regions. The background compositions of the validation regions are similar compared with their corresponding signal regions. Table 6.2 shows the expected number of events in each background and the observed number of events in data. The comparisons of some variable distributions between the background and the data are also shown in figures 6.4 and 6.5 for VRjet1 and VRjet23 respectively. The estimated background and the data agree with each other within the uncertainties.

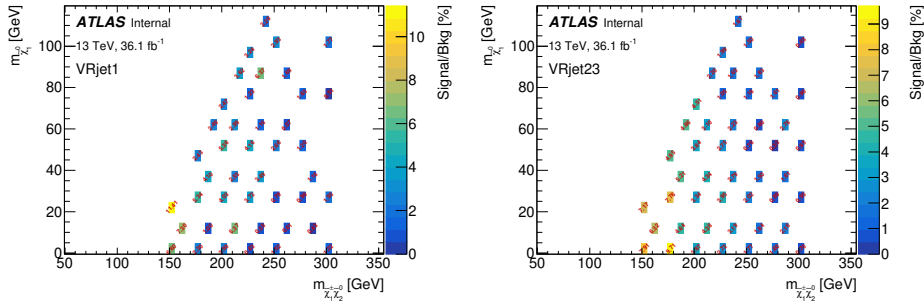


Figure 6.1: Fractions of signal contribution are shown for the VRjet1 (left) and VRjet23 (right).

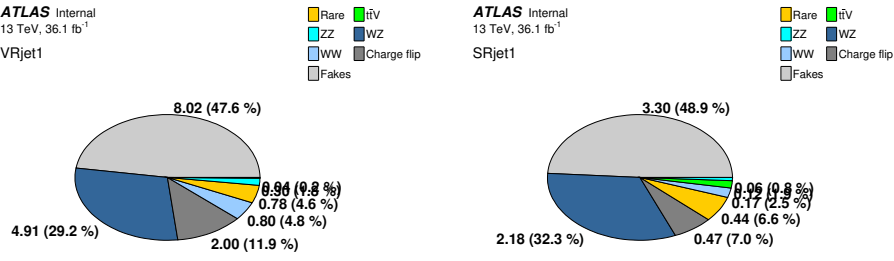


Figure 6.2: Background composition in the VRjet1 (left) and SRjet1 (right).

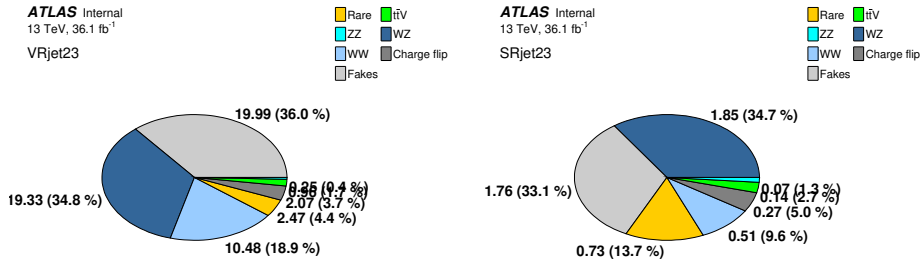


Figure 6.3: Background composition in the VRjet23 (left) and SRjet23 (right).

Process	VRjet1	VRjet23
Rare	$0.775 \pm 0.389^{+0.661}_{-0.362}$	$2.469 \pm 0.674^{+0.998}_{-0.899}$
$t\bar{t}V$	$0.039 \pm 0.013^{+0.018}_{-0.012}$	$0.959 \pm 0.082^{+0.152}_{-0.146}$
ZZ	$0.298 \pm 0.060^{+0.089}_{-0.063}$	$0.247 \pm 0.045^{+0.113}_{-0.047}$
WZ	$4.909 \pm 0.530^{+0.960}_{-0.899}$	$19.325 \pm 0.643^{+4.393}_{-4.346}$
WW	$0.801 \pm 0.051^{+0.123}_{-0.060}$	$10.477 \pm 0.176^{+0.796}_{-0.726}$
Charge flip	$1.997 \pm 0.128^{+0.260}_{-0.260}$	$2.065 \pm 0.085^{+0.166}_{-0.166}$
Fakes	$8.021 \pm 1.390^{+5.806}_{-5.806}$	$19.990 \pm 2.013^{+13.461}_{-13.461}$
Total BG	$16.839 \pm 1.545^{+5.915}_{-5.912}$	$55.534 \pm 2.228^{+14.396}_{-14.332}$
Data	17	54

Table 6.2: The expected number of background events and the observed number of data events in the VRjet1 (the second column) and VRjet23 (the third column). The uncertainties include the statistical and systematic uncertainties.

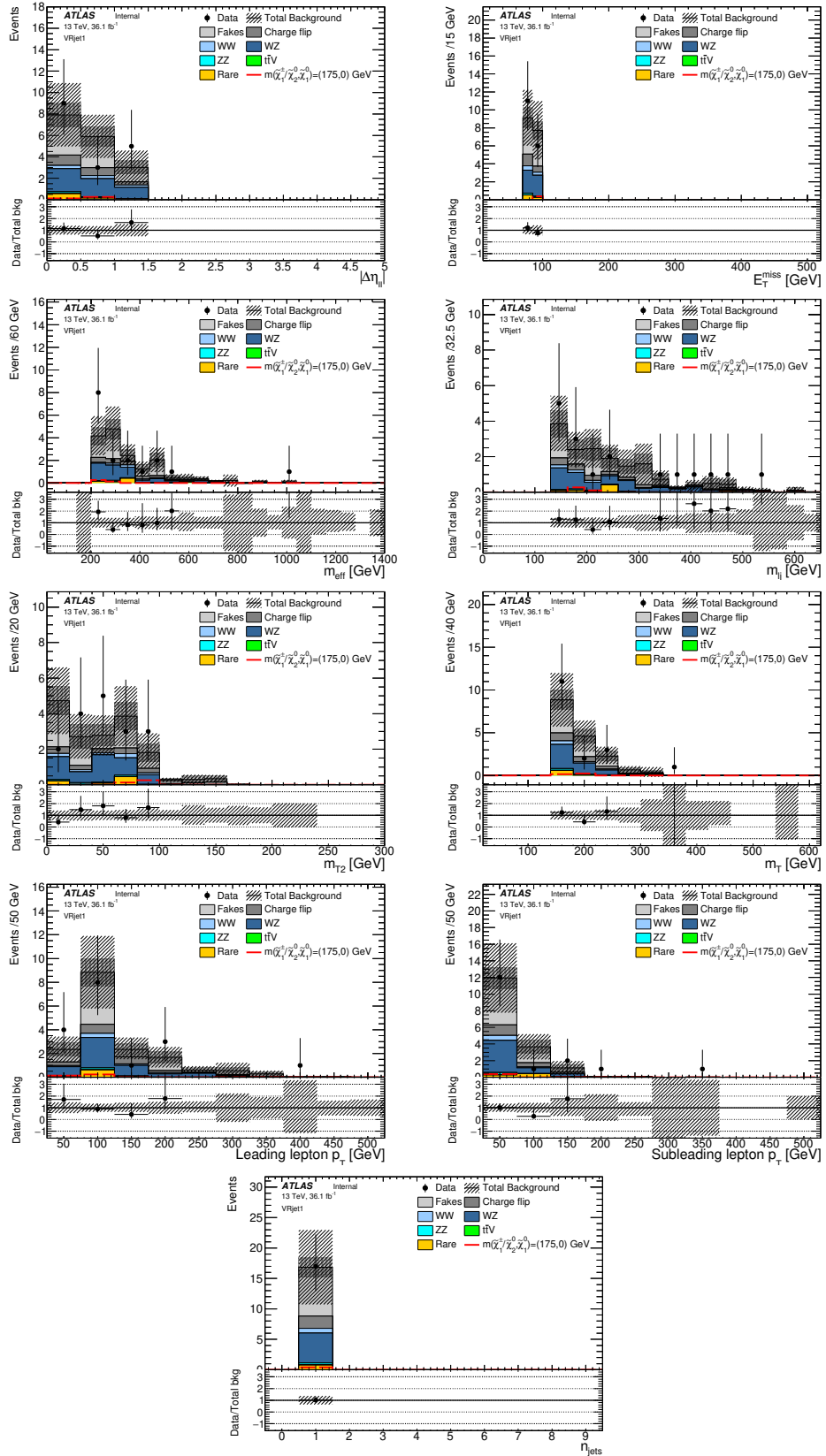


Figure 6.4: Distributions of the variables in the VRjet1 for the background estimation and the data are shown. A signal at a mass point $(m_{\tilde{\chi}_1^\pm, \tilde{\chi}_2^0} = (175, 0))$ is also shown. The internal shaded area refers to the statistical uncertainties, while the external shaded area refers to the total uncertainty.

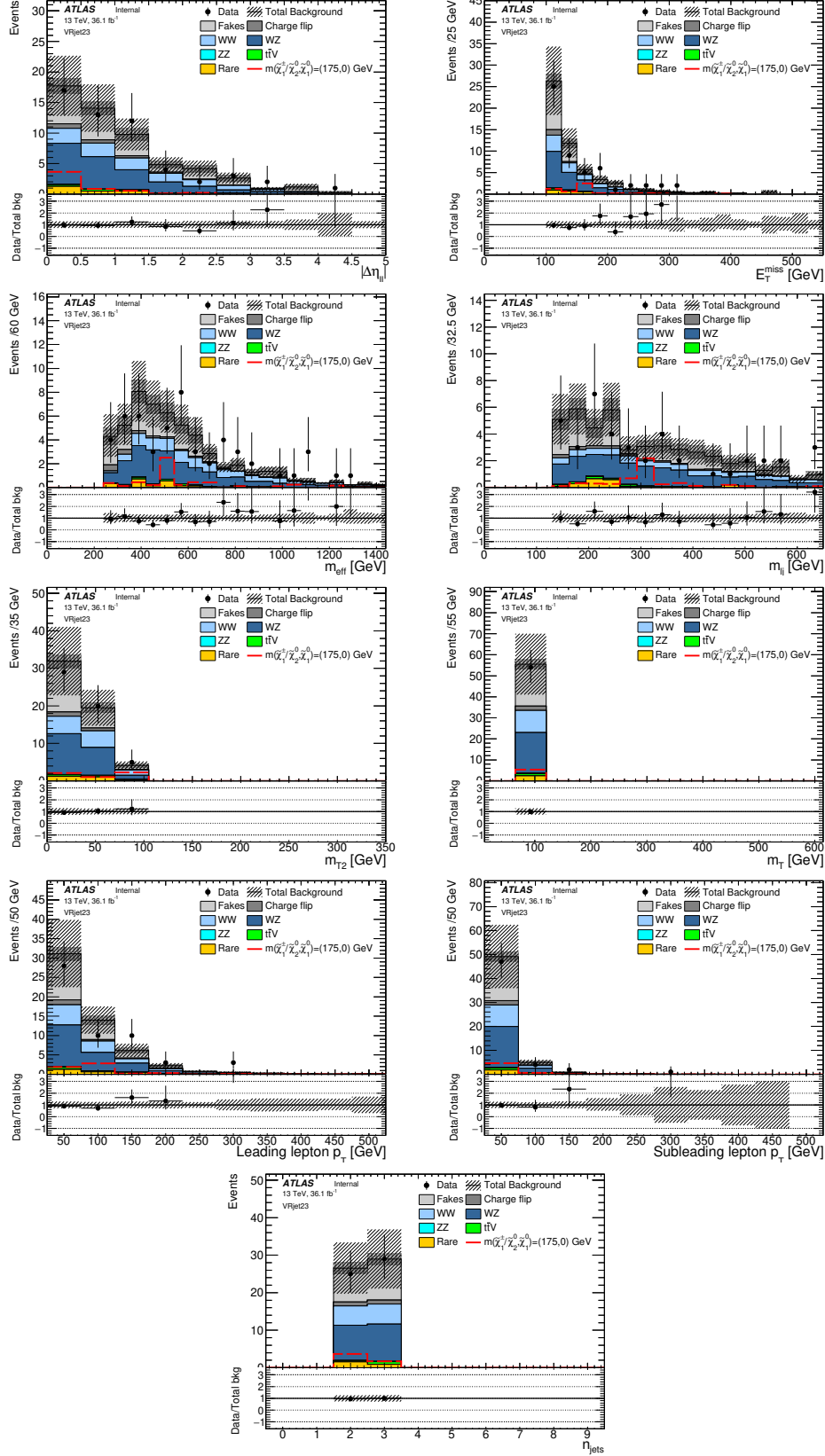


Figure 6.5: Distributions of the variables in the VRjet23 for the background estimation and the data are shown. A signal at a mass point $(m_{\tilde{\chi}_1^\pm}, m_{\tilde{\chi}_2^0}, m_{\tilde{\chi}_1^0}) = (175, 0)$ GeV is also shown. The internal shaded area refers to the statistical uncertainties, while the external shaded area refers to the total uncertainty.

Chapter 7

Results

No significant excess in signal is observed in the signal regions. Hence, the upper limits of the SUSY cross sections as a function of the masses of $m_{\tilde{\chi}_1^\pm, \tilde{\chi}_2^0}$ and $m_{\tilde{\chi}_1^0}$ are set at the 95% confidence level, in the simplified supersymmetric model.

The observed events in data and the estimated background yields in the two signal regions are shown in table 7.1. The N-1 plots (i.e. all SR selections, but the variable on the x-axis, are applied) for the two signal regions are shown in figures 7.1 and 7.2. The observed data and the Standard Model expectations agree with each other in all distributions within the uncertainties.

	SRjet1	SRjet23
Observed events	2	8
Total background	6.74 ± 2.18	5.33 ± 1.61
Fakes events	3.30 ± 2.10	1.76 ± 1.47
MC exp. WZ events	2.18 ± 0.46	1.85 ± 0.57
MC exp. Rare events	0.44 ± 0.13	0.73 ± 0.17
MC exp. ttV events	0.12 ± 0.05	0.14 ± 0.05
MC exp. WW events	0.17 ± 0.03	0.51 ± 0.07
MC exp. ZZ events	0.06 ± 0.03	0.07 ± 0.04
Charge-flip events	0.47 ± 0.07	0.27 ± 0.03

Table 7.1: The observed events and the background yields in the signal regions are shown. The uncertainties include the statistical and systematic uncertainties.

Table 7.2 shows the results of the model-independent fit. The numbers in the first column are the upper limits on the observed visible cross-section σ_{vis}

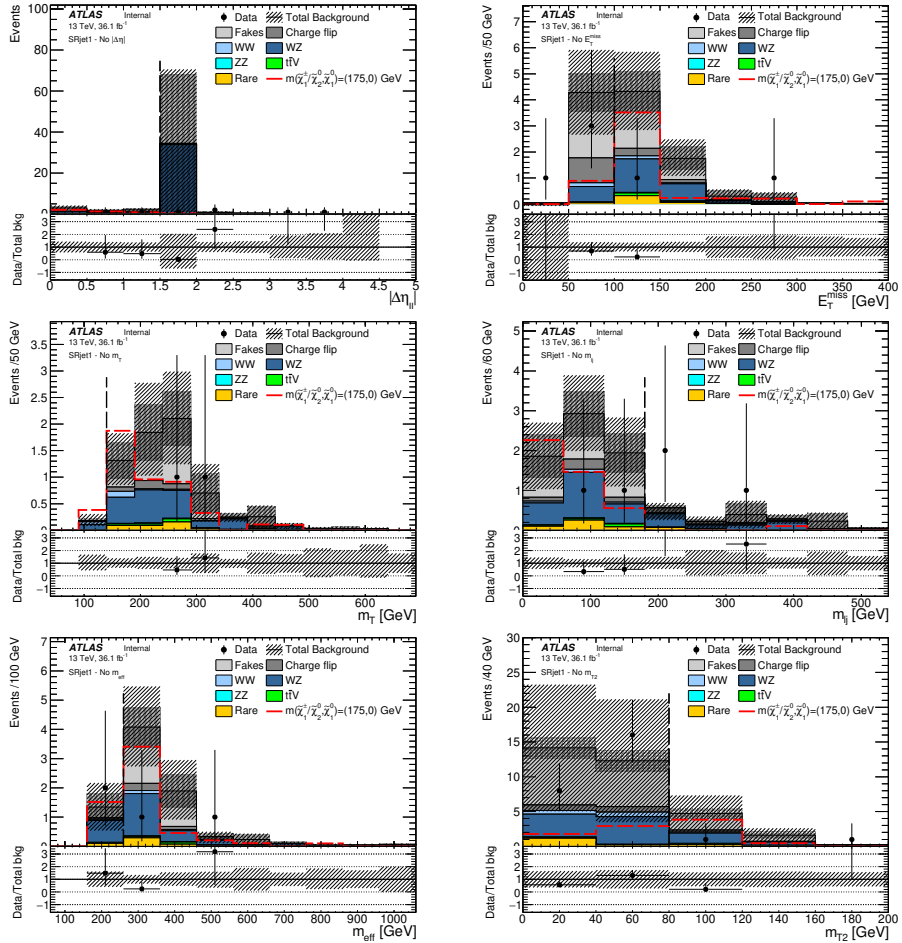


Figure 7.1: N-1 plots for different variable distributions in the SRjet1 for the background estimation and the data. The signal of the mass point with the highest significance ($m_{\tilde{\chi}_1^\pm, \tilde{\chi}_2^0} = (175, 0)$ GeV) is shown by the red dashed line. The internal shaded area refers to the statistical uncertainties, while the external shaded area refers to the total uncertainty. The vertical dashed line shows the SR cut of that variable. The lower plot shows the ratio of data yields with respect to the total background predictions. The plots are made by Dr. Daniela Paredes [1].

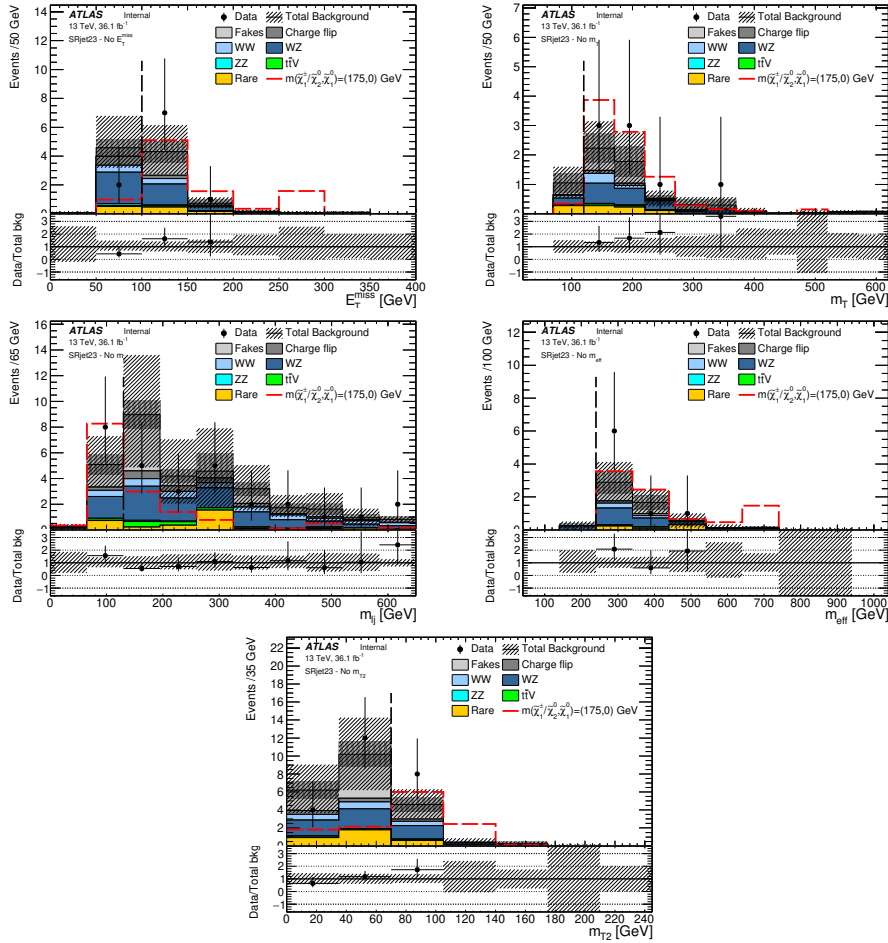


Figure 7.2: N-1 plots for different variable distributions in the SRjet23 for the background estimation and the data. The signal of the mass point with the highest significance ($m_{\tilde{\chi}_1^\pm, \tilde{\chi}_2^0, \tilde{\chi}_1^0} = (175, 0)$ GeV) is shown by the red dashed line. The internal shaded area refers to the statistical uncertainties, while the external shaded area refers to the total uncertainty. The vertical dashed line shows the SR cut of that variable. The lower plot shows the ratio of data yields with respect to the total background predictions. The plots are made by Dr. Daniela Paredes [1].

at 95% confidence level. The second and third column show the upper limits on the observed (S_{obs}^{95}) and expected (S_{exp}^{95}) signal events respectively, at 95% confidence level. The fluctuations of the upper limits of S_{exp}^{95} are also shown, with $\pm 1\sigma$ excursions on the expectation of the background events. The definition of the observed visible cross-section $\langle \sigma_{\text{vis}} \rangle$ is the product of a BSM cross-section, the acceptance and the selection efficiency of a BSM signal. The last column shows the discovery p -value (p_0). It is the probability that the Standard Model background fluctuate to the observed number of events or higher.

	$\langle \sigma_{\text{vis}} \rangle_{\text{obs}}^{95} [\text{fb}]$	S_{obs}^{95}	S_{exp}^{95}	p_0
SRjet1	0.12	4.2	$6.1^{+2.7}_{-1.5}$	0.50
SRjet23	0.27	9.9	$6.6^{+3.4}_{-1.1}$	0.17

Table 7.2: From left to right: 95% confidence level upper limits on the visible cross section ($\langle \sigma_{\text{vis}} \rangle_{\text{obs}}^{95}$) and on the observed number of signal events (S_{obs}^{95}). The third column (S_{exp}^{95}) shows the 95% confidence level upper limit on the expected number of signal events, with $\pm 1\sigma$ excursions on the expectation of the background events. The last column shows the discovery p -value (p_0).

Figure 7.3 shows the expected and observed exclusion limits on the masses of $m_{\tilde{\chi}_1^\pm, \tilde{\chi}_2^0}$ and $m_{\tilde{\chi}_1^0}$ at the 95% confidence level. The mass points inside the curve are excluded. The exclusion limits are calculated by combining the two signal regions. Compared with other channels in Wh search [1], our same-sign channel is sensitive in the low $m_{\tilde{\chi}_1^\pm, \tilde{\chi}_2^0}$ region and the compressed region described in section 1.5. The exclusion limits for the masses $m_{\tilde{\chi}_1^\pm, \tilde{\chi}_2^0}$ and $m_{\tilde{\chi}_1^0}$ supersede the run 1 results [7].

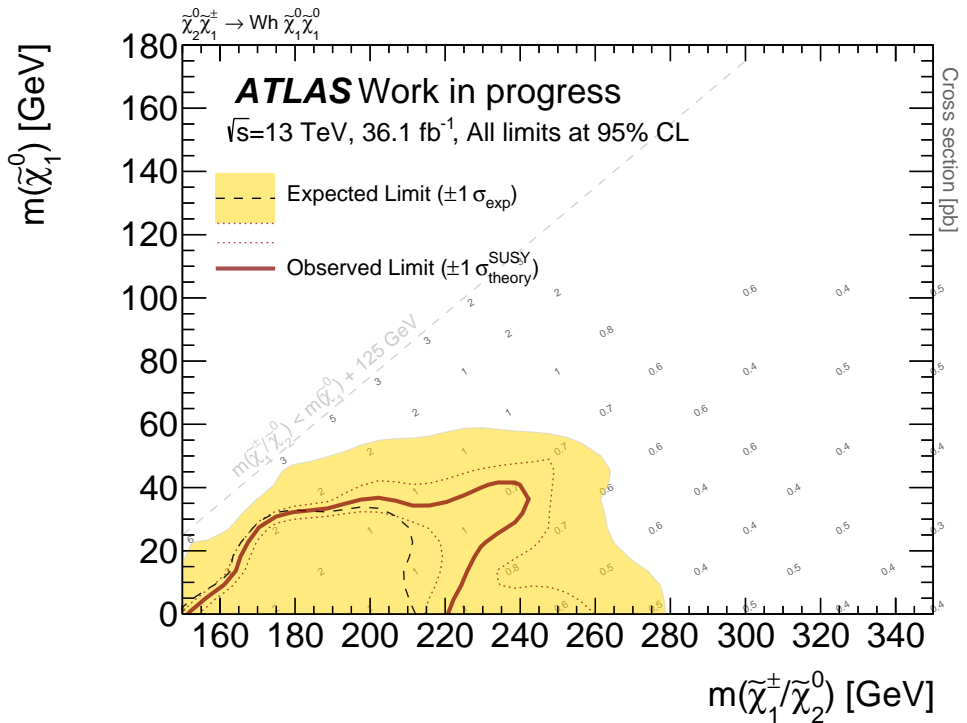


Figure 7.3: The expected and observed exclusion limits for the combined SRjet1 and SRjet23 are shown. Experimental and theoretical systematic uncertainties are applied to background and signal samples and illustrated by the yellow band and the red dotted contour lines respectively. The red dotted lines indicate the $\pm 1\sigma$ variation on the observed exclusion limit due to theoretical uncertainties on the signal cross-section. The upper limits for signal cross section at different mass points are also shown in grey numbers.

Chapter 8

Conclusion

Results of a search for the electroweak pair production of chargino and neutralino ($p + p \rightarrow \tilde{\chi}_1^\pm + \tilde{\chi}_2^0$) are presented in the Wh channel $\tilde{\chi}_1^\pm \rightarrow \tilde{\chi}_1^0 + W$ and $\tilde{\chi}_2^0 \rightarrow \tilde{\chi}_1^0 + h$ with same-sign leptons in the final states. The dominant background is the fake lepton background, and the dominant irreducible background is the diboson processes, especially the WZ processes. Two signal regions are defined and optimized for the compressed region where the mass difference between $\tilde{\chi}_1^\pm/\tilde{\chi}_2^0$ and $\tilde{\chi}_1^0$ is close to the Higgs mass 125 GeV. No significant deviations from the SM predictions are observed, therefore new exclusion limits for the masses $m_{\tilde{\chi}_1^\pm, \tilde{\chi}_2^0}$ and $m_{\tilde{\chi}_1^0}$ are set, which supersedes the run 1 results [7].

Appendix A

List of MC samples

A.1 List of data samples

The following Good Run Lists (GRL) are used.

- `data15_13TeV.periodAllYear_DetStatus-v79-repro20-02_DQDefects-00-02-02_PHYS_StandardGRL--All_Good_25ns.xml` for 2015 data.
- `data16_13TeV.periodAllYear_DetStatus-v89-pro21-01_DQDefects-00-02-04_PHYS_StandardGRL--All_Good_25ns.xml` for 2016 data.

The following is the list of data samples used.

```
data15_13TeV.periodD.physics_Main.PhysCont.DAOD_SUSY2.grp15_v02_p2950
data15_13TeV.periodE.physics_Main.PhysCont.DAOD_SUSY2.grp15_v02_p2950
data15_13TeV.periodF.physics_Main.PhysCont.DAOD_SUSY2.grp15_v02_p2950
data15_13TeV.periodG.physics_Main.PhysCont.DAOD_SUSY2.grp15_v02_p2950
data15_13TeV.periodH.physics_Main.PhysCont.DAOD_SUSY2.grp15_v02_p2950
data15_13TeV.periodJ.physics_Main.PhysCont.DAOD_SUSY2.grp15_v02_p2950
data16_13TeV.periodA.physics_Main.PhysCont.DAOD_SUSY2.grp16_v02_p2950
data16_13TeV.periodB.physics_Main.PhysCont.DAOD_SUSY2.grp16_v02_p2950
data16_13TeV.periodC.physics_Main.PhysCont.DAOD_SUSY2.grp16_v02_p2950
data16_13TeV.periodD.physics_Main.PhysCont.DAOD_SUSY2.grp16_v02_p2950
data16_13TeV.periodE.physics_Main.PhysCont.DAOD_SUSY2.grp16_v02_p2950
data16_13TeV.periodF.physics_Main.PhysCont.DAOD_SUSY2.grp16_v02_p2950
data16_13TeV.periodG.physics_Main.PhysCont.DAOD_SUSY2.grp16_v02_p2950
data16_13TeV.periodI.physics_Main.PhysCont.DAOD_SUSY2.grp16_v02_p2950
data16_13TeV.periodK.physics_Main.PhysCont.DAOD_SUSY2.grp16_v02_p2950
data16_13TeV.periodL.physics_Main.PhysCont.DAOD_SUSY2.grp16_v02_p2950
```

A.2 List of background MC samples

Dataset ID	Process	Tags	Cross section [pb]	k-factor	Generator efficiency	$\mathcal{L}_{\text{int}} [\text{fb}^{-1}]$
364156	Sherpa_221_NNPDF30NNLO_Wmmu_MAXHTPTV0_70_CVetoBVeto	e5340_s2726_r7772_r7676_p2949	19143.0000	0.97	0.824	1.616
364157	Sherpa_221_NNPDF30NNLO_Wmmu_MAXHTPTV0_70_CFilterBVeto	e5340_s2726_r7772_r7676_p2949	19121.0000	0.97	0.130	4.071
364158	Sherpa_221_NNPDF30NNLO_Wmmu_MAXHTPTV0_70_BFilter	e5340_s2726_r7772_r7676_p2949	19135.0000	0.97	0.044	21.032
364159	Sherpa_221_NNPDF30NNLO_Wmmu_MAXHTPTV0_70_CVetoBVeto	e5340_s2726_r7772_r7676_p2949	944.8500	0.97	0.675	23.912
364160	Sherpa_221_NNPDF30NNLO_Wmmu_MAXHTPTV70_140_CFilterBVeto	e5340_s2726_r7772_r7676_p2949	937.7800	0.97	0.235	46.173
364161	Sherpa_221_NNPDF30NNLO_Wmmu_MAXHTPTV70_140_BFilter	e5340_s2726_r7772_r7676_p2949	944.6300	0.97	0.076	283.269
364162	Sherpa_221_NNPDF30NNLO_Wmmu_MAXHTPTV140_280_CVetoBVeto	e5340_s2726_r7772_r7676_p2949	339.5400	0.97	0.626	47.919
364163	Sherpa_221_NNPDF30NNLO_Wmmu_MAXHTPTV140_280_CFilterBVeto	e5340_s2726_r7772_r7676_p2949	340.0600	0.97	0.289	77.568
364164	Sherpa_221_NNPDF30NNLO_Wmmu_MAXHTPTV140_280_BFilter	e5340_s2726_r7772_r7676_p2949	339.5400	0.97	0.109	686.449
364165	Sherpa_221_NNPDF30NNLO_Wmmu_MAXHTPTV280_500_CVetoBVeto	e5340_s2726_r7772_r7676_p2949	72.0670	0.97	0.546	129.289
364166	Sherpa_221_NNPDF30NNLO_Wmmu_MAXHTPTV280_500_CFilterBVeto	e5340_s2726_r7772_r7676_p2949	72.1980	0.97	0.317	133.034
364167	Sherpa_221_NNPDF30NNLO_Wmmu_MAXHTPTV280_500_BFilter	e5340_s2726_r7772_r7676_p2949	72.0450	0.97	0.133	317.464
364168	Sherpa_221_NNPDF30NNLO_Wmmu_MAXHTPTV500_1000	e5340_s2726_r7772_r7676_p2949	15.0100	0.97	1.000	405.866
364169	Sherpa_221_NNPDF30NNLO_Wmmu_MAXHTPTV1000_E_CMS	e5340_s2726_r7772_r7676_p2949	1.2344	0.97	1.000	3305.737
364170	Sherpa_221_NNPDF30NNLO_Wenu_MAXHTPTV0_70_CVetoBVeto	e5340_s2726_r7772_r7676_p2949	19127.0000	0.97	0.824	1.617
364171	Sherpa_221_NNPDF30NNLO_Wenu_MAXHTPTV0_70_CFilterBVeto	e5340_s2726_r7772_r7676_p2949	19130.0000	0.97	0.130	4.074
364172	Sherpa_221_NNPDF30NNLO_Wenu_MAXHTPTV0_70_BFilter	e5340_s2726_r7772_r7676_p2949	19135.0000	0.97	0.044	20.272
364173	Sherpa_221_NNPDF30NNLO_Wenu_MAXHTPTV70_140_CVetoBVeto	e5340_s2726_r7772_r7676_p2949	942.5800	0.97	0.669	23.973
364174	Sherpa_221_NNPDF30NNLO_Wenu_MAXHTPTV70_140_CFilterBVeto	e5340_s2726_r7772_r7676_p2949	945.6700	0.97	0.228	46.963
364175	Sherpa_221_NNPDF30NNLO_Wenu_MAXHTPTV70_140_BFilter	e5340_s2726_r7772_r7676_p2949	945.1500	0.97	0.103	103.368
364176	Sherpa_221_NNPDF30NNLO_Wenu_MAXHTPTV140_280_CVetoBVeto	e5340_s2726_r7772_r7676_p2949	339.8100	0.97	0.597	50.200
364177	Sherpa_221_NNPDF30NNLO_Wenu_MAXHTPTV140_280_CFilterBVeto	e5340_s2726_r7772_r7676_p2949	339.8700	0.97	0.290	77.584
364178	Sherpa_221_NNPDF30NNLO_Wenu_MAXHTPTV140_280_BFilter	e5340_s2726_r7772_r7676_p2949	339.4800	0.97	0.109	687.518
364179	Sherpa_221_NNPDF30NNLO_Wemu_MAXHTPTV280_500_CVetoBVeto	e5340_s2726_r7772_r7676_p2949	72.0840	0.97	0.544	129.323
364180	Sherpa_221_NNPDF30NNLO_Wemu_MAXHTPTV280_500_CFilterBVeto	e5340_s2726_r7772_r7676_p2949	72.1280	0.97	0.317	133.693
364181	Sherpa_221_NNPDF30NNLO_Wemu_MAXHTPTV280_500_BFilter	e5340_s2726_r7772_r7676_p2949	72.1130	0.97	0.134	315.726
364182	Sherpa_221_NNPDF30NNLO_Wemu_MAXHTPTV500_1000	e5340_s2726_r7772_r7676_p2949	15.2240	0.97	1.000	400.587
364183	Sherpa_221_NNPDF30NNLO_Wemu_MAXHTPTV1000_E_CMS	e5340_s2726_r7772_r7676_p2949	1.2334	0.97	1.000	3298.389
364184	Sherpa_221_NNPDF30NNLO_Wtaunu_MAXHTPTV0_70_CVetoBVeto	e5340_s2726_r7772_r7676_p2949	19152.0000	0.97	0.825	1.617
364185	Sherpa_221_NNPDF30NNLO_Wtaunu_MAXHTPTV70_140_CFilterBVeto	e5340_s2726_r7772_r7676_p2949	19153.0000	0.97	0.129	4.105
364186	Sherpa_221_NNPDF30NNLO_Wtaunu_MAXHTPTV0_70_BFilter	e5340_s2726_r7772_r7676_p2949	19163.0000	0.97	0.045	20.834
364187	Sherpa_221_NNPDF30NNLO_Wtaunu_MAXHTPTV70_140_CVetoBVeto	e5340_s2726_r7772_r7676_p2949	947.6500	0.97	0.674	23.903
364188	Sherpa_221_NNPDF30NNLO_Wtaunu_MAXHTPTV70_140_CFilterBVeto	e5340_s2726_r7772_r7676_p2949	946.7300	0.97	0.222	48.307
364189	Sherpa_221_NNPDF30NNLO_Wtaunu_MAXHTPTV70_140_BFilter	e5340_s2726_r7772_r7676_p2949	943.3000	0.97	0.104	103.602
364190	Sherpa_221_NNPDF30NNLO_Wtaunu_MAXHTPTV140_280_CVetoBVeto	e5340_s2726_r7772_r7676_p2949	339.3600	0.97	0.596	50.427
364191	Sherpa_221_NNPDF30NNLO_Wtaunu_MAXHTPTV140_280_CFilterBVeto	e5340_s2726_r7772_r7676_p2949	339.6300	0.97	0.290	76.903
364192	Sherpa_221_NNPDF30NNLO_Wtaunu_MAXHTPTV140_280_BFilter	e5340_s2726_r7772_r7676_p2949	339.5400	0.97	0.118	632.798
364193	Sherpa_221_NNPDF30NNLO_Wtaunu_MAXHTPTV280_500_CVetoBVeto	e5340_s2726_r7772_r7676_p2949	72.0650	0.92	0.546	136.270
364194	Sherpa_221_NNPDF30NNLO_Wtaunu_MAXHTPTV280_500_CFilterBVeto	e5340_s2726_r7772_r7676_p2949	71.9760	0.97	0.316	133.773
364195	Sherpa_221_NNPDF30NNLO_Wtaunu_MAXHTPTV280_500_BFilter	e5340_s2726_r7772_r7676_p2949	72.0260	0.97	0.134	314.868
364196	Sherpa_221_NNPDF30NNLO_Wtaunu_MAXHTPTV500_1000	e5340_s2726_r7772_r7676_p2949	15.0460	0.97	1.000	407.258
364197	Sherpa_221_NNPDF30NNLO_Wtaunu_MAXHTPTV1000_E_CMS	e5340_s2726_r7772_r7676_p2949	1.2339	0.97	1.000	3296.218

Table A.1: List of simulated W+jets processes

Dataset ID	Process	Tags	Cross section [pb]	k-factor	Generator efficiency	$\mathcal{L}_{int}[\text{fb}^{-1}]$
301535	Sherpa_CTI0_eegammaPt10_35	e3952_s2608_s2183_r7725_r7676_p2949	52.7060	1.00	1.000	94.596
301536	Sherpa_CTI0_mumugammaPt10_35	e3952_s2608_s2183_r7773_r7676_p2949	52.7080	1.00	1.000	94.509
301890	Sherpa_CTI0_enugammaPt35_70	e3952_s2608_s2183_r7725_r7676_p2949	15.3480	1.00	1.000	32.525
301891	Sherpa_CTI0_enugammaPt70_140	e3952_s2608_s2183_r7725_r7676_p2949	1.5282	1.00	1.000	163.591
301892	Sherpa_CTI0_enugammaPt140	e3952_s2608_s2183_r7725_r7676_p2949	0.2415	1.00	1.000	1034.154
301893	Sherpa_CTI0_munugammaPt35_70	e3952_s2608_s2183_r7725_r7676_p2949	15.2720	1.00	1.000	32.674
301894	Sherpa_CTI0_munugammaPt70_140	e3952_s2608_s2183_r7725_r7676_p2949	1.5235	1.00	1.000	163.702
301895	Sherpa_CTI0_munugammaPt140	e3952_s2608_s2183_r7725_r7676_p2949	0.2418	1.00	1.000	1031.303
301896	Sherpa_CTI0_tauaugammaPt35_70	e3952_s2608_s2183_r7725_r7676_p2949	15.2970	1.00	1.000	32.568
301897	Sherpa_CTI0_tauaugammaPt70_140	e3952_s2608_s2183_r7725_r7676_p2949	1.5290	1.00	1.000	163.244
301898	Sherpa_CTI0_tauaugammaPt140	e3952_s2608_s2183_r7725_r7676_p2949	0.2426	1.00	1.000	1028.854
301899	Sherpa_CTI0_eegammaPt35_70	e3952_s2608_s2183_r7725_r7676_p2949	5.2420	1.00	1.000	95.383
301900	Sherpa_CTI0_eegammaPt70_140	e3952_s2608_s2183_r7725_r7676_p2949	0.3846	1.00	1.000	640.749
301901	Sherpa_CTI0_eegammaPt140	e3952_s2608_s2183_r7725_r7676_p2949	0.0472	1.00	1.000	5295.601
301902	Sherpa_CTI0_mumugammaPt35_70	e3952_s2608_s2183_r7725_r7676_p2949	5.2455	1.00	1.000	95.053
301903	Sherpa_CTI0_mumugammaPt70_140	e3952_s2608_s2183_r7725_r7676_p2949	0.3855	1.00	1.000	648.023
301904	Sherpa_CTI0_mumugammaPt140	e3952_s2608_s2183_r7725_r7676_p2949	0.0472	1.00	1.000	5275.190
301905	Sherpa_CTI0_tautaugammaPt35_70	e3952_s2608_s2183_r7725_r7676_p2949	5.2490	1.00	1.000	95.066
301906	Sherpa_CTI0_tautaugammaPt70_140	e3952_s2608_s2183_r7725_r7676_p2949	0.3848	1.00	1.000	649.135
301907	Sherpa_CTI0_tautaugammaPt140	e3952_s2608_s2183_r7725_r7676_p2949	0.0470	1.00	1.000	5295.056

Table A.11: List of simulated $V+\gamma$ processes

A.3 List of signal MC samples

Appendix B

Label for trigger [3,4]

B.1 Electron trigger

Label name	Description
lhvloose	Identification quality is likelihood very loose
lhloose	Identification quality is likelihood loose
lhmedium	Identification quality is likelihood medium
lhtight	Identification quality is likelihood tight
ivarloose	Isolation requirement: $\text{ptvarcone20}/E_T < 0.1$
nod0	Alignment-robust likelihood tune with no d0 information used
L1EM20VH	Level 1 trigger input: $p_T > 20 \text{ GeV}$
L12EM10VH	Level 1 trigger input: $p_T > 10 \text{ GeV}$

Table B.1: Label for electron trigger.

B.2 Muon trigger

Label name	Description
iloose	Isolation requirement: $\text{ptcone20}/p_T < 0.12$
imedium	Isolation requirement: $\text{ptcone30}/p_T < 0.06$
L1MU15	Level 1 trigger input: $p_T > 15 \text{ GeV}$
noL1	Level 1 trigger input: none

Table B.2: Label for muon trigger.

References

- [1] ATLAS Collaboration Collaboration, M. Aaboud et al., *Search for chargino and neutralino production in final states with a Higgs boson and missing transverse momentum at $\sqrt{s} = 13$ TeV with the ATLAS detector*, Tech. Rep. arXiv:1812.09432, CERN, Geneva, Dec, 2018.
<http://cds.cern.ch/record/2652633>.
- [2] A. Cervelli, G. Gallardo, J. Lorenz, D. M. Koeck, D. Paredes Hernandez, P. Tornambe, M. Javurkova, Y. Tu, D. Zhang, and C. Y. Lo, *Search for chargino and neutralino production in final states with two same-sign leptons, jets and missing transverse momentum at $\sqrt{s} = 13$ TeV with the ATLAS detector*, Tech. Rep. ATL-COM-PHYS-2017-1808, CERN, Geneva, Dec, 2017. <https://cds.cern.ch/record/2298595>.
- [3] ATLAS Collaboration Collaboration, M. Aaboud et al., *Performance of the ATLAS Trigger System in 2015. Performance of the ATLAS Trigger System in 2015*, Tech. Rep. CERN-EP-2016-241. 5, Nov, 2016.
<https://cds.cern.ch/record/2235584>. 77 pages in total, author list starting page 61, 50 figures, 1 table. Published in Eur. Phys. J. C. All figures including auxiliary figures are available at <http://atlas.web.cern.ch/Atlas/GROUPS/PHYSICS/PAPERS/TRIG-2016-01/>.
- [4] *Trigger naming Run 2*, 2019.
<https://twiki.cern.ch/twiki/bin/view/Atlas/TriggerNamingRun2>.
- [5] *Standard Model of Elementary Particles*, 2018.
https://en.wikipedia.org/wiki/File:Standard_Model_of_Elementary_Particles.svg.

- [6] *Standard Model Feynman Diagram Vertices*, 2018.
https://en.wikipedia.org/wiki/File:Standard_Model_Feynman_Diagram_Vertices.png.
- [7] ATLAS Collaboration Collaboration, G. Aad et al., *Search for direct pair production of a chargino and a neutralino decaying to the 125 GeV Higgs boson in $\sqrt{s} = 8$ TeV pp collisions with the ATLAS detector. Search for direct pair production of a chargino and a neutralino decaying to the 125 GeV Higgs boson in $\sqrt{s} = 8$ TeV pp collisions with the ATLAS detector*, Eur. Phys. J. C **C75** (2015) 208. 34 p,
<http://cds.cern.ch/record/1983600>, Comments: 19 pages plus cover page plus author list (34 pages total), 8 figures, 10 tables, submitted to EPJC, All figures including auxiliary figures are available at <http://atlas.web.cern.ch/Atlas/GROUPS/PHYSICS/PAPERS/SUSY-2013-23/>.
- [8] E. Mobs, *The CERN accelerator complex. Complexe des accélérateurs du CERN*, <https://cds.cern.ch/record/2197559>, General Photo.
- [9] J. Pequenao, *Computer generated image of the whole ATLAS detector*, <https://cds.cern.ch/record/1095924>.
- [10] J. Pequenao and P. Schaffner, *How ATLAS detects particles: diagram of particle paths in the detector*, <https://cds.cern.ch/record/1505342>.
- [11] *Different values of pseudorapidity shown against a polar grid*, 2018. https://commons.wikimedia.org/wiki/File:Pseudorapidity_plot.svg.
- [12] ATLAS Collaboration Collaboration,, *ATLAS magnet system: Technical Design Report*, 1. Technical Design Report ATLAS. CERN, Geneva, 1997.
<http://cds.cern.ch/record/338080>.
- [13] J. Pequenao, *Computer generated image of the ATLAS inner detector*, <https://cds.cern.ch/record/1095926>.
- [14] ATLAS Collaboration Collaboration, G. Aad et al., *The ATLAS Experiment at the CERN Large Hadron Collider*, JINST **3** (2008) S08003. 437 p, <http://cds.cern.ch/record/1129811>, Also published by CERN Geneva in 2010.

- [15] J. Pequenao, *Computer Generated image of the ATLAS calorimeter*,
<https://cds.cern.ch/record/1095927>.
- [16] ATLAS Collaboration Collaboration,, *ATLAS liquid-argon calorimeter: Technical Design Report*. Technical Design Report ATLAS. CERN, Geneva, 1996. <https://cds.cern.ch/record/331061>.
- [17] J. Pequenao, *Computer generated image of the ATLAS Muons subsystem*,
<https://cds.cern.ch/record/1095929>.
- [18] S. P. Martin, *A Supersymmetry primer*, arXiv:hep-ph/9709356 [hep-ph], [Adv. Ser. Direct. High Energy Phys.18,1(1998)].
- [19] ATLAS Collaboration Collaboration,, *Search for squarks and gluinos in final states with jets and missing transverse momentum using 36 fb^{-1} of $\sqrt{s} = 13 \text{ TeV}$ pp collision data with the ATLAS detector*, Tech. Rep. ATLAS-CONF-2017-022, CERN, Geneva, Apr, 2017.
<https://cds.cern.ch/record/2258145>.
- [20] *The accelerator complex*, 2018. <https://home.cern/about/accelerators>.
- [21] *Pulling together: Superconducting electromagnets*, 2018.
<https://home.cern/about/engineering/pulling-together-superconducting-electromagnets>.
- [22] *Cryogenics: Low temperatures, high performance*, 2018.
<https://home.cern/about/engineering/cryogenics-low-temperatures-high-performance>.
- [23] ATLAS Collaboration Collaboration, G. Aad et al., *Muon reconstruction performance of the ATLAS detector in proton-proton collision data at $\sqrt{s}=13 \text{ TeV}$. Muon reconstruction performance of the ATLAS detector in proton-proton collision data at $\sqrt{s}=13 \text{ TeV}$* , Eur. Phys. J. C **76** (2016) 292. 45 p, <http://cds.cern.ch/record/2139897>, Comments: 27 pages
 including cover page plus author list (45 pages total), 12 figures, 3 tables, submitted to Eur. Phys. J. C. All figures including auxiliary figures are available at
<https://atlas.web.cern.ch/Atlas/GROUPS/PHYSICS/PAPERS/PERF-2015-10/>.

- [24] *Selection of jets produced in 13TeV proton-proton collisions with the ATLAS detector*, Tech. Rep. ATLAS-CONF-2015-029, CERN, Geneva, Jul, 2015. <https://cds.cern.ch/record/2037702>.
- [25] ATLAS Collaboration Collaboration, M. Aaboud et al., *Electron reconstruction and identification in the ATLAS experiment using the 2015 and 2016 LHC proton-proton collision data at $\sqrt{s} = 13$ TeV*, Tech. Rep. arXiv:1902.04655, CERN, Geneva, Feb, 2019. <https://cds.cern.ch/record/2657964>.
- [26] M. Cacciari, G. P. Salam, and G. Soyez, *The anti- k_t jet clustering algorithm*, JHEP **04** (2008) 063, [arXiv:0802.1189 \[hep-ph\]](https://arxiv.org/abs/0802.1189).
- [27] ATLAS Collaboration Collaboration, G. Aad et al., *Performance of pile-up mitigation techniques for jets in pp collisions at $\sqrt{s} = 8$ TeV using the ATLAS detector. Performance of pile-up mitigation techniques for jets in pp collisions at $\sqrt{s} = 8$ TeV using the ATLAS detector*, Eur. Phys. J. C **76** (2015) 581. 54 p, <https://cds.cern.ch/record/2058295>, 38 pages, plus author list - 54 pages (total), 19 figures. Published in EPJC. All figures including auxiliary figures are available at <http://atlas.web.cern.ch/Atlas/GROUPS/PHYSICS/PAPERS/PERF-2014-03/>.
- [28] ATLAS Collaboration Collaboration,, *Optimisation of the ATLAS b-tagging performance for the 2016 LHC Run*, Tech. Rep. ATL-PHYS-PUB-2016-012, CERN, Geneva, Jun, 2016. <https://cds.cern.ch/record/2160731>.
- [29] A. J. Barr, C. Lester, and P. Stephens, *A variable for measuring masses at hadron colliders when missing energy is expected; m_{T2} : the truth behind the glamour*, J. Phys. G **29** (2003) 2343–63, <https://cds.cern.ch/record/725984>.
- [30] C. Clement, G. Conti, J. Dietrich, A. Floderus, S. Fratina, S. French, B. Gjelsten, E. Hines, B. Jackson, P. Klimek, T. Kono, F. Legger, C. Lester, M. Morii, M. Medinnis, A. S. Mete, A. Petridis, P. Pralavorio, M. Relich, T. Serre, A. Taffard, E. Thomson, B. Togerson, M. Tylmad, R. Ueno, S. Williams, J. Wittkowski, and M. Vincter, *Searching for direct gaugino production and direct slepton production with two leptons and missing*

transverse momentum at $\sqrt{s} = 8$ TeV, Tech. Rep.

ATL-COM-PHYS-2013-911, CERN, Geneva, Jul, 2013.

<https://cds.cern.ch/record/1560083>.